F_{420} COFACTOR DEPENDENT ENZYMES: KINETIC, MECHANISTIC AND STRUCTURAL CHARACTERIZATION OF F_{420}-DEPENDENT GLUCOSE-6-PHOSPHATE DEHYDROGENASE (FGD) FROM *MYCOBACTERIUM TUBERCULOSIS*

by

MERCY A. OYUGI

Presented to the Faculty of the Graduate School of

The University of Texas at Arlington in Partial Fulfillment

of the Requirements

for the Degree of

DOCTOR OF PHILOSOPHY

THE UNIVERSITY OF TEXAS AT ARLINGTON

August 2017

Acknowledgements

My sincerest gratitude to my research advisor, Dr. Kayunta Johnson-Winters. You have supported and guided me through every step of my graduate career and I have truly learnt a lot from you, not just academically, but also about life in general. You will always be a role model for me to look up to and I thank you for everything.

Special thanks to my dissertation committee members, Dr. Subhrangsu Mandal, Dr. Jongyun Heo and Dr. Frank Foss for their helpful and invaluable advice. I would also like to acknowledge our collaborators at the University of Auckland (Dr. Edward Baker and Dr. Ghader Bashiri) and at the University of Texas at Austin (Dr. Jessie Zhang and Joshua Mayfield) for their constant assistance and productive discussions.

Thank you to past and present members of Dr. Johnson-Winters' research group- Dr. Ebenezer Joseph, Dr. Cuong Le, Tijani Osumah, Toan Nguyen, Hasmat Ullah, Siqi Du, Lindsay Davis and Denzel Pugh. I appreciate your friendship and useful input towards my research. Thank you to everyone at the UTA Department of Chemistry and Biochemistry who has assisted me in one way or another.

To my beloved family, my parents (Maurice and Martha Oyugi) and my siblings Emily, Lynnette and Erick, I will forever be grateful for your enduring love, prayers and support, without which I would not have come this far. My heartfelt appreciation for my fiancé, Dennis Otieno, whose unconditional love, encouragement and faith in what I can achieve, has seen me through the ups and downs of graduate school and life in general.

Finally, I give thanks to God for how far He has brought me and for the unmerited love and favor He has shown me throughout my life. Through God, I can do all things and it's only by His strength that I have been able to achieve this great milestone of completing my doctorate studies. To God be the glory.

June 30, 2017

Abstract

F_{420} COFACTOR DEPENDENT ENZYMES: KINETIC, MECHANISTIC AND STRUCTURAL CHARACTERIZATION OF F_{420}-DEPENDENT GLUCOSE-6-PHOSPHATE DEHYDROGENASE (FGD) FROM *MYCOBACTERIUM TUBERCULOSIS*

Mercy A. Oyugi, PhD

The University of Texas at Arlington, 2017

Supervising Professor: Kayunta Johnson-Winters

F_{420}-dependent glucose-6-phosphate dehydrogenase (FGD) from *Mycobacterium tuberculosis* (*Mtb*) is one of a few enzymes that utilize the unique F_{420} cofactor for catalysis. FGD catalyzes the first committed step of the pentose-phosphate pathway, where it uses the oxidized F_{420} cofactor to convert glucose-6-phosphate (G6P) to 6-phosphogluconolactone. *Mtb* is the bacteria that causes Tuberculosis (TB), which is currently the world's deadliest bacterial disease. The pentose-phosphate pathway is important for survival of *Mtb*, since it provides precursors for nucleic acid synthesis and yields reducing equivalents that are essential for other metabolic pathways. The fact that FGD catalyzes the committed step of the pentose-phosphate pathway makes it a promising target for therapeutic purposes against TB. Chapter 1 gives detailed background on the F_{420} cofactor, FGD, and the direct link to TB disease.

The focus of the work presented here is to investigate FGD using a variety of protein characterization methods so as to deduce structural and mechanistic information about the enzyme. Chapter 2 discusses the mechanistic investigation of the FGD reaction using site-directed mutagenesis of essential active site residues. Five FGD variants (H40A,

E109Q, W44A, W44F, and W44Y) along with the wild-type FGD were analyzed using fluorescence binding assays, steady state and pre-steady state kinetic methods. All five variants were found to be less catalytically active than the wild-type FGD, with the FGD H40A variant being the least active with ~1000 fold decrease in activity. The pH profile of the wild-type FGD, FGD H40A and FGD E109Q confirmed that Glu109 is the active site acid for the FGD reaction, while His40 was proven to not be the active site base as was previously proposed. The multiple turnover pre-steady state kinetics exponential decay curves were biphasic, suggesting that hydride transfer is not rate-limiting.

Chapter 3 presents further investigation of the wild-type FGD mechanism using substrate inhibition experiments along with solvent and substrate deuterium isotope effects studies. The substrate inhibition studies revealed an ordered substrate addition mechanism in which FGD must first bind F_{420} before binding the G6P substrate. The deuterium isotope effects results yielded normal SKIE on the k_{cat} and k_{cat}/K_m, and this effect is likely a contribution of the Glu109 hydrogen that protonates the F_{420} at position N1.

In Chapter 4, the catalytically inactive FGD H40A variant was successfully co-crystallized with both F_{420} and G6P in an attempt at providing novel insights into the interactions within the FGD active site. The crystal structure of this variant was solved at 2.9 Å resolution, revealing a vast network of interactions between the phosphate moiety and C1-C4 hydroxyl groups of G6P with some FGD active site residues.

Table of Contents

List of Illustrations

List of Tables

List of Abbreviations

βME	2-mercaptoethanol
Ddn	Deazaflavin-dependent nitroreductase
F_{420} cofactor	7,8-didemethyl-8-hydroxy-5-deazariboflavin-5'-phosphoryllactyl(glutamyl)$_n$
FAD	Flavin adenine dinucleotide
Fe^{2+}	Ferrous ion
FGD	F_{420}-dependent glucose-6-phosphate dehydrogenase
FMN	Flavin mononucleotide
G6P	Glucose-6-phosphate
G6P-d_1	Deuterated glucose-6-phosphate (at H of C1)
G6PD	Glucose-6-phosphate dehydrogenase
HBL	Hydrogen bond length
k_{cat}	Turnover number
k_{cat}/K_m	Catalytic efficiency
K_d	Dissociation constant
K_m	Michaelis-Menten constant
k_{obs}	Observed rate constant
LC-MS-IT-TOF	Liquid chromatography-mass spectrometry-ion trap-time of flight
M. smegmatis	*Mycobacterium smegmatis*
M. tuberculosis	*Mycobacterium tuberculosis*
Mn^{2+}	Manganese ion
NAD^+	Nicotinamide adenine dinucleotide
$NADP^+$	Nicotinamide adenine dinucleotide phosphate

PA-824	Pretomanid
PEG	Polyethylene glycol
p*K*	Ionization constant
SDS-PAGE	Sodium dodecyl sulfate-polyacrylamide gel electrophoresis
SEC	Size exclusion chromatography
SKIE	Solvent kinetic isotope effect
SSHB	Short strong hydrogen bond
TB	Tuberculosis
Zn^{2+}	Zinc ion

Chapter 1

F_{420} COFACTOR, F_{420} DEPENDENT ENZYMES AND TUBERCULOSIS DISEASE

1.1 Introduction

Enzymes are biological catalysts that speed up the rates of chemical reactions. Most enzymes are protein in nature and their substrate specificity allows them to catalyze only specific reactions. In order to function, most enzymes require cofactors which help in mediating the reactions catalyzed by the enzymes. Cofactors can be either inorganic or organic. Inorganic cofactors are usually metal ions such as Zn^{2+}, Mn^{2+} or Fe^{2+}. Organic cofactors are called coenzymes, examples of which include $NADP^+$, F_{420}, FAD, FMN and NAD^+. This chapter discusses the F_{420} cofactor in detail, presenting its chemical and physical properties, biological significance, biosynthetic pathway and phylogenetic distribution. This chapter also introduces the *M. tuberculosis* enzyme F_{420}-dependent glucose-6-phosphate dehydrogenase (FGD), discussing its catalyzed reaction, crystal structure, and proposed mechanism. Finally, this chapter addresses the implications of both the F_{420} cofactor and FGD on Tuberculosis disease (TB).

1.2 F_{420} cofactor

1.2.1 Structure of the F_{420} cofactor

The chemical name of the F_{420} cofactor is 7,8-didemethyl-8-hydroxy-5-deazariboflavin-5'-phosphoryllactyl(glutamyl)$_n$, which is descriptive of the various moieties that make up the F_{420} cofactor (Figure 1.1).[1] The primary component of the F_{420} cofactor is the 5-deazaisoalloxazine fused-ring system, which contains the sites of chemistry at positions N1 and C5. The side chain of the F_{420} cofactor contains four different structures and is linked at position N10 of the 5'-deazaisoalloxazine moiety. The first side chain component linked directly at the N10 position is a ribitol group, which together with the 5-deazaisoalloxazine moiety, forms the FO fragment of the F_{420} cofactor. This FO fragment

is known to be catalytically active with several F_{420}-dependent enzymes.[1-4] The next component of the side chain is a phosphate group, which forms the F^+ fragment together with the FO. The third structure in the side chain is a lactyl group and this together with the F^+ forms the F_{420}-0 fragment. At the end of the side chain is a γ-linked polyglutamate tail whose length varies from 1-9 depending on the species from which the cofactor is found (F_{420}-1 to F_{420}-9).

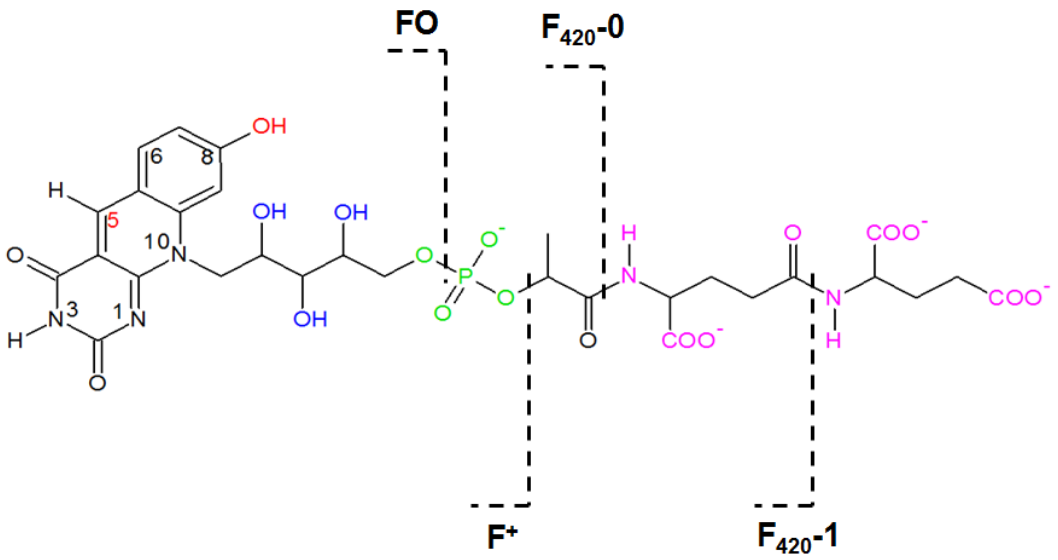

Figure 1.1 Structure of the F_{420} cofactor showing the 5'-deazaisoalloxazine chromophore, with a side chain at N10 consisting of a ribitol (blue), phosphate (green), lactate (black), and a polyglutamate tail (purple). The fragments of the F_{420} cofactor are also shown in dashed lines.[5]

The F_{420} cofactor is a flavin analogue with notable structural differences compared to other known flavin cofactors. These structural differences contribute immensely to the chemistry of the F_{420} cofactor, which is discussed in Section 1.2.2. One significant structural difference is that the F_{420} cofactor contains a carbon at position 5, whereas the other flavins possess a nitrogen atom at position 5. Another difference is that flavins contain methyl groups at positions C7 and C8, while the F_{420} cofactor is demethylated at position C7 and

the methyl group has been replaced with a hydroxyl group at position C8. Finally, the F_{420} cofactor has a polyglutamate tail at the end of its side chain, which is a feature that other flavins do not possess.

1.2.2 Spectral properties and chemistry of the F_{420} cofactor

The F_{420} cofactor derives its name from its unique spectral properties. When the F_{420} cofactor is oxidized, it has a strong absorbance peak at 420 nm (Figure 1.2). Upon reduction, the F_{420} cofactor loses the peak at 420 nm and instead gains a shoulder at 325 nm (Figure 1.2).[6,7] The reduced $F_{420}H_2$ has less conjugated bonds compared to the oxidized F_{420}, and this in turn results in the observed spectral changes between the two redox states of the cofactor (Figure 1.2). This unique absorbance profile of the F_{420} cofactor provides the capability of conducting kinetic experiments of F_{420}-dependent enzymes by monitoring the reactions at 420 nm. The molar extinction coefficients (ε) for the oxidized F_{420} and reduced $F_{420}H_2$ are also significantly different, with $\varepsilon_{oxidized,420}$ being 45.5 $mM^{-1}cm^{-1}$ and $\varepsilon_{reduced,325}$ being lower at 10.8 $mM^{-1}cm^{-1}$.[1]

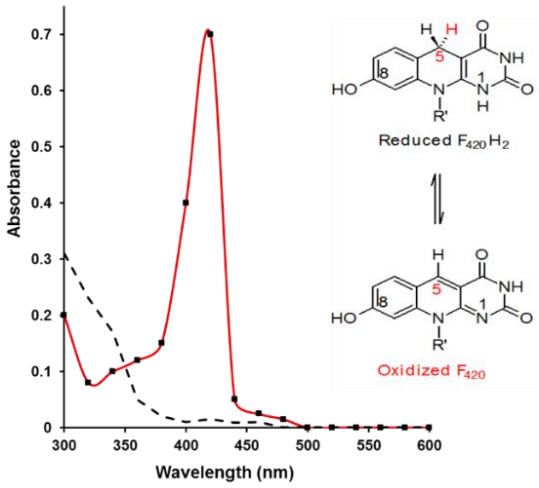

Figure 1.2 Absorbance spectra of the oxidized F_{420} (red solid line) and reduced $F_{420}H_2$ (black dashed line).[6]

The F_{420} cofactor is chemically equivalent to NAD^+ and $NADP^+$ in its redox chemistry, in that it is strictly a two-electron acceptor. Because it lacks a nitrogen atom at position 5, the F_{420} cofactor does not display the semiquinone form common to other flavins, and can therefore only facilitate hydride transfer reactions. The sites of the redox chemistry are at the C5 and N1 positions of the 5-deazaisoalloxazine chromophore (Figure 1.2).

In 1984, the redox potential of the F_{420} cofactor was investigated by the Jacobson group and found to be approximately −350 mV.[8] This redox potential is more negative than that of flavins and thus gives the F_{420} cofactor the unique ability to facilitate the reduction of NAD^+ with electrons from hydrogen or formate oxidation (Figure 1.3).[9]

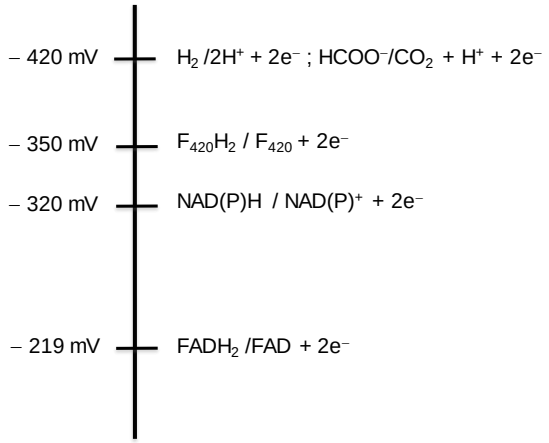

Figure 1.3 Redox potential ladder of the F_{420} cofactor and other physiological electron transfer mediators.[10]

The absorbance spectra of the F_{420} cofactor is also pH-dependent (Figure 1.4).[1,5,8] The maximum absorbance wavelength (λ_{max}) of the F_{420} cofactor is 420 nm when in solutions with pH values greater than 6. However, at pH values lower than 6, the λ_{max} of the F_{420} cofactor shifts from 420 nm to lower wavelengths with an isosbestic point of 401

nm. (Figure 1.4). The observed shift in λ_{max} can be attributed to the pH-dependent ionization events that occur at the C8-OH and N3-H positions of the 5'-deazaisoalloxazine chromophore (Figure 1.5A). The C8-OH group has a pK_a value of 6.3,[1] and at higher pH, the hydroxyl proton is abstracted, resulting in a negatively charged 5'-deazaisoalloxazine chromophore. The negatively charged chromophore has two resonance structures (Figure 1.5B and C) which then contribute to the observed shift in λ_{max}.[8] At increasingly basic pH, the N3-H proton is also removed and the resulting structure (Figure 1.5D) further contributes to the shift in λ_{max} to longer wavelengths.[1,5,8]

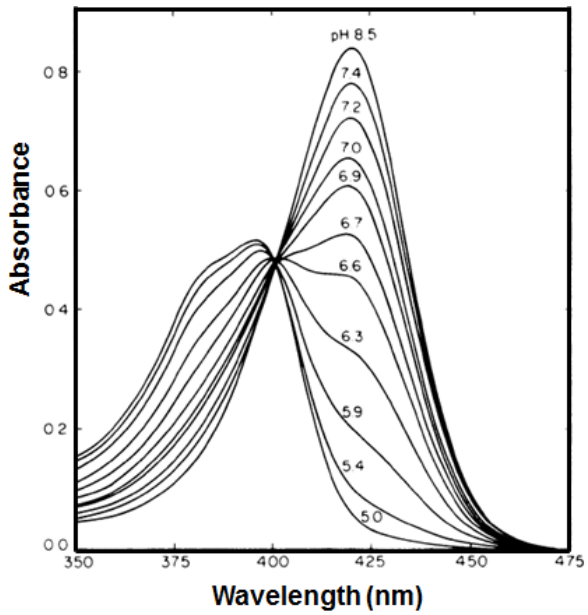

Figure 1.4 UV-Vis absorbance spectra showing the effect of pH on the absorbance properties of the oxidized F_{420} cofactor.[5] A shift in the λ_{max} from 420 nm to lower wavelengths is observed at pH lower than 6.

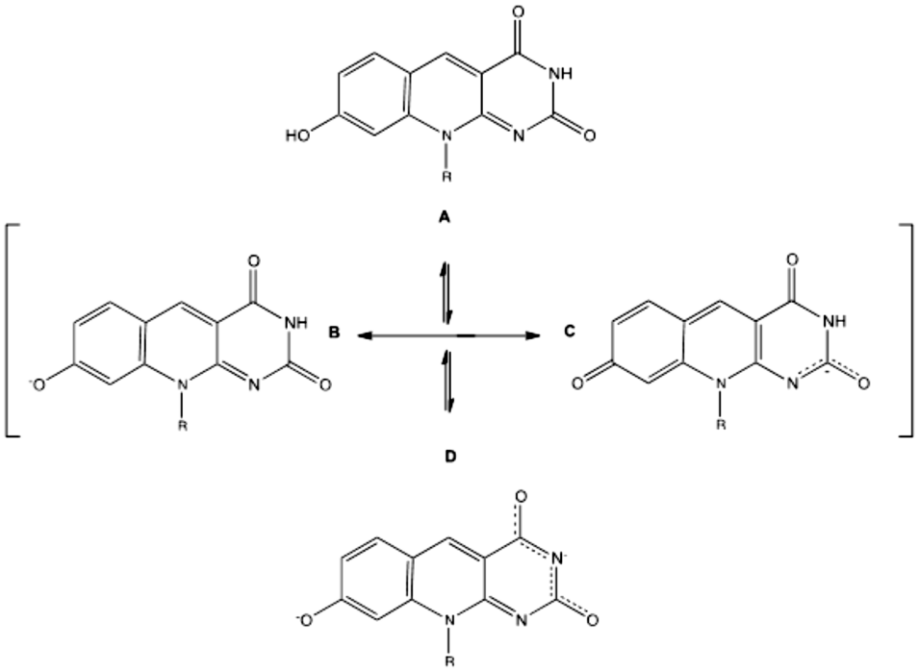

Figure 1.5 Ionization events that occur at the 5'-deazaisoalloxazine chromophore of the F_{420} cofactor (**A**). The deprotonation at the C8-OH results in a negatively charged structure with two possible resonance forms (**B** and **C**), while further deprotonation at the N3-H increases the negative charge on the structure (**D**), resulting in further shifts in λ_{max} to longer wavelengths.[8,11]

1.2.3 Biosynthetic pathway of the F_{420} cofactor

The early steps in the synthesis of F_{420} and other riboflavins lead to the formation of 5-amino-6-ribitylamino-2,4(1H,3H)-pyrimidinedione (ARP).[12] ARP is synthesized in 5 enzymatic steps (Figure 1.6). The first step is catalyzed by guanosine triphosphate (GTP) cyclohydrolase III (ArfA), which converts GTP to 2-amino-5-formylamino-6-ribosylamino-4(3H)-pyrimidinone 5' monophosphate (FAPy) (Figure 1.6, Structure II).[12] The second step is catalyzed by a formamide hydrolase (ArfB) which converts FAPy to 2,5-diamino-6-ribosylamino-4(3H)-pyrimidinone 5'-phosphate (APy) (Figure 1.6, Structure III).[12] The next

step involves the reduction of the APy to 2,5-diamino-6- ribitylamino-4(3H)-pyrimidinone 5-phosphate (Figure 1.6, Structure IV) by the enzyme APy reductase (ArfC).[12,13] The next reaction is catalyzed by an unknown enzyme and involves the deamination of the pyrimidine at C2 to form 2-amino-5-formylamino-6-ribosylamino-4(3H) pyrimidinone 5'-monophosphate (ARP-P) (Figure 1.6, Structure V). Finally, the dephosphorylation of ARP-P by an enzyme that is also unknown yields ARP (Figure 1.6, Structure VI).[12] The enzyme FO synthase (CofGH) then catalyzes the condensation of ARP and 4-hydroxyphenylpyruvate to form the F_{420} precursor 7,8-didemethyl-8-hydroxy-5-deazariboflavin (FO) (Figure 1.6, Structure VII).[14,15]

The next integral process in the synthesis of F_{420} involves the assembly of the side chain. The fusion of 2-phospho-L-lactate with GTP yields lactyl-2-diphospho-5'-guanosine (LPPG), and the reaction is catalyzed by phospho-L-lactate guanylyltransferase (CofC). The enzyme 2-phospho-L-Lactate transferase (CofD) then facilitates the transfer of 2-phospho-L-lactate from LPPG to FO, forming the core F_{420}-0 structure (Figure 1.6, Structure IX).[12,16] Finally, a polyglutamate tail is added to the F_{420}-0 structure, and the number of glutamates varies from 1-9 depending on the organism. The first two glutamates are added to F_{420}-0 by the GTP-dependent enzyme F_{420}-0:L-glutamate ligase (CofE), in two sequential reactions that yield F_{420}-1 then F_{420}-2 (Figure 1.6, Structures X and XI).[17,18]

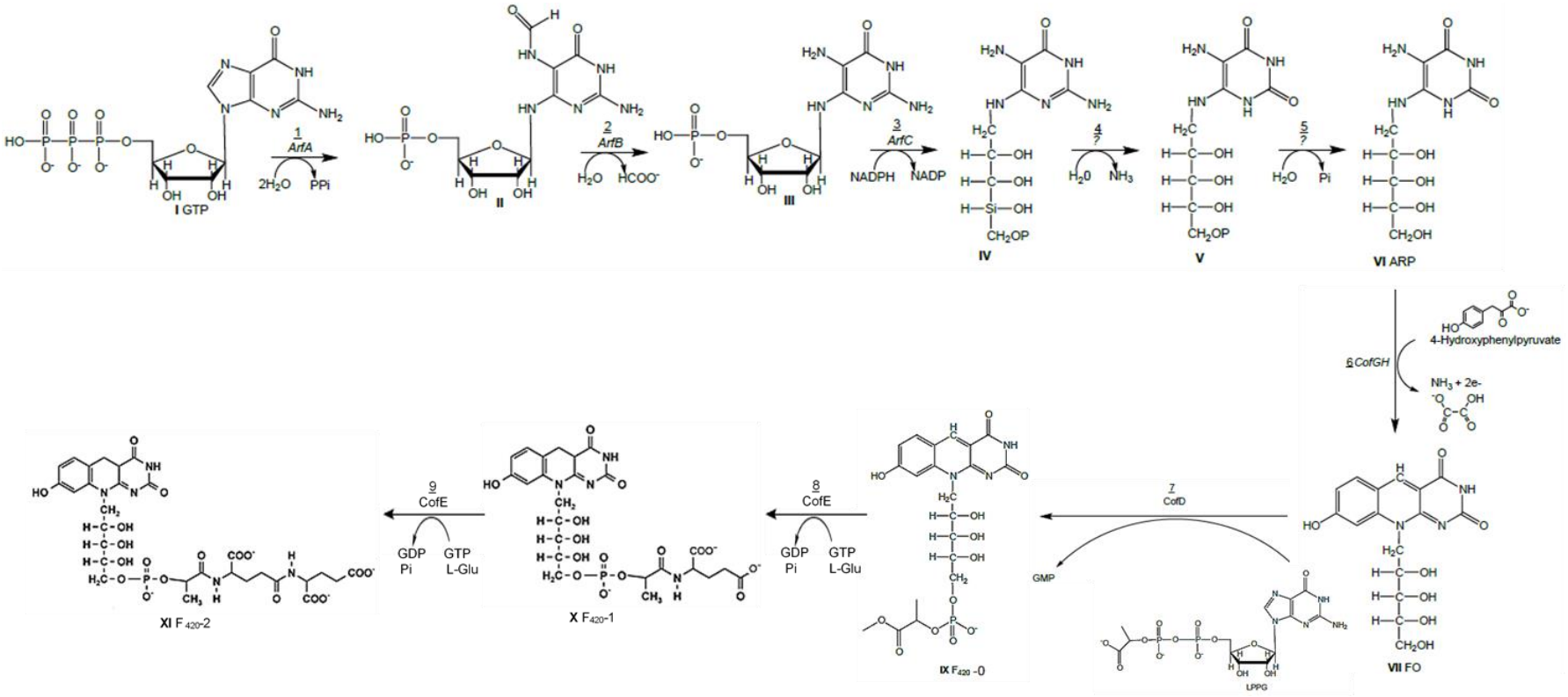

Figure 1.6 Biosynthetic pathway of the F_{420} cofactor. **[I]** GTP; **[II]** 2-amino-5-formylamino-6-ribosylamino-4(3H)-pyrimidinone 5'-monophosphate (FAPy); [**III]** 2,5-diamino-6-ribosylamino-4(3H)-pyrimidinone 5'-phosphate (APy); **[IV]** triaminopyrimidine phosphate; **[V]** 2-amino-5-formylamino-6-ribosylamino-4(3H) pyrimidinone 5'-monophosphate (ARP-P); **[VI]** 5-amino-*6*-ribitylamino-2,4(1H,3H)-pyrimidinedione (ARP); **[VII]** 7,8-didemethyl-8-hydroxy-5-deazariboflavin (FO); **[VIII]** lactyl-2-diphospho-5'-guanosine (LPPG); **[IX]** F_{420}-0; **[X]** F_{420}-1; and **[XI]** F_{420}-2.[12-18]

1.2.4 Phylogenetic distribution of F_{420}-dependent enzymes

The F_{420} cofactor was first isolated and characterized from methanogenic archaea in 1972,[6] but has since been found to be present in several other archaeal, bacterial and eukaryotic microorganisms (Table 1.1). F_{420} in archaea is thought to be found in all strictly anaerobic methanogens,[5,6] where it serves as a major catabolic cofactor in two central methanogenic pathways. Methanogenic archaea that synthesize methane using hydrogenotrophic pathways contain about 100-400 mg/kg of the F_{420} cofactor.[5,19,20] F_{420} is also found in a few non-methanogenic archaea, including the sulfate-reducing *Archaeglobus* genus,[21-24] and the photosynthetic *Halobacteria* and *Halococcus* genera.[25,26]

Within bacteria, the F_{420} cofactor is found in some species of the *Mycobacterium*,[27-29] *Nocardia*,[27,29] *Streptomyces*,[27,30,31] and *Norcadioides*[32] genera. Within *Mycobacterium*, the F_{420} cofactor has significant health implications as it is found in the three major obligate pathogens, *M. tuberculosis, M. leprae, and M. bovis.* The F_{420} within *Mycobacterium* protects the organisms against oxidative and nitrosative stress, and also against naturally available antibiotic and xenobiotic compounds.[33,34] The F_{420} cofactor found in *Streptomyces* mainly functions in antibiotic biosynthesis pathways. Within *Nocardia* and *Norcadioides* the F_{420} cofactor is majorly involved in aerobic catabolism pathways such as degradation of nitrophenols.

The F_{420} cofactor precursor, FO, has been isolated from only two eukaryotic organisms, *D. melanogaster* and *O. tauri*. Within these two organisms, FO acts as a light-harvesting antenna for the DNA photolyase that is responsible for DNA repair and maintenance.[35,36] Table 1.1 summarizes a list of F_{420}-dependent enzymes, the organisms in which they are found, and their biological functions.

Table 1.1 Phylogenetic distribution of F_{420}-dependent enzymes and their biological functions.

Organism	Enzyme	Function
Archaea	F_{420} reducing hydrogenase (Frh)[3]	Hydrogenotrophic methanogenesis
	F_{420}:formate dehydrogenase (Ffd)[7]	Formatotrophic methanogenesis
	$F_{420}H_2$ oxidase (Fpr)[37]	O_2 detoxification
	$F_{420}H_2$:NADP+ oxidoreductase (Fno)[38]	Source of NADPH
	$F_{420}H_2$:heterodisulfide oxidoreductase (Fho)[39]	Source of $F_{420}H_2$ for ATP synthesis
	$F_{420}H_2$:quinone oxidoreductase (Fqo)[40]	Membrane-bound electron transport system
	Methylenetetrahydromethanopterin dehydrogenase (Mtd)[41]	Methanogenesis
	Methylenetetrahydromethanopterin reductase (Mer)[42]	Methanogenesis
	Secondary alcohol dehydrogenase (Adf)[43]	Isopropanol oxidation
	$F_{420}H_2$-dependent sulfite reductase (Fsr)[44]	Sulfite detoxification
Bacteria	F_{420}:H_2 tetracycline synthases (Fts)[30]	Tetracycline biosynthesis
	F_{420} hydride transferase (Fht)[32]	Biodegradation of nitrophenol compounds
	F_{420}-dependent glucose-6-phosphate dehydrogenase (FGD)[45]	Source of $F_{420}H_2$
	Deazaflavin–dependent nitroreductase (Ddn)[46]	Pretomanid pro-drug activation
	F_{420}-reducing hydroxymycolic acid dehydrogenase (fHMAD)[47]	Cell wall biosynthesis
	$F_{420}H_2$-dependent reductases (Fdr)[48]	Xenobiotic metabolism
Eukaryota	DNA photolyase[35]	DNA repair and maintenance

1.3 F_{420}-dependent glucose-6-phosphate dehydrogenase (FGD)

1.3.1 FGD catalyzed reaction

The enzyme FGD was first isolated from *M. smegmatis*,[45] but has since been found to be present in other environmental actinobacteria and some obligate mycobacteria pathogens.[29] FGD uses the oxidized F_{420} cofactor to convert glucose-6-phosphate (G6P) to 6-phosphogluconolactone, thus producing the reduced cofactor, $F_{420}H_2$ (Figure 1.7). This reaction catalyzed by FGD is the first committed step of the pentose-phosphate pathway. The pentose phosphate pathway is responsible for producing ribose sugars necessary for nucleic acid synthesis, and it also produces reducing equivalents in the form of $F_{420}H_2$ that can be used in subsequent enzymatic reactions. $F_{420}H_2$ is used in the activation of an experimental TB drug (PA-824 or Pretomanid),[46,49] and it has also been shown to enhance survival of *M. tuberculosis* by protecting the bacteria against nitrosative damage.[33] FGD is, therefore, evidently a very essential enzyme that is crucial for the survival of mycobacteria, especially since it is the only known source of the reduced cofactor $F_{420}H_2$ within mycobacteria.[34]

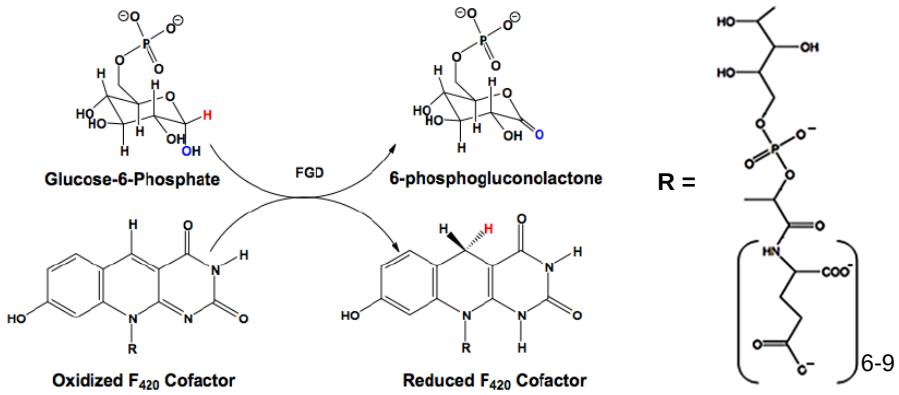

Figure 1.7 FGD-catalyzed reaction. FGD utilizes the oxidized form of the cofactor F_{420} to convert glucose-6-phosphate (G6P) to 6-phosphogluconolactone, thus yielding the reduced cofactor, $F_{420}H_2$.[45]

1.3.2 FGD crystal structure

In 2008, the Baker group solved the *M. tuberculosis* FGD crystal structure at 1.95 Å resolution in complex with the F_{420} cofactor and citrate (Figure 1.8A and B).[50] Citrate binds in the G6P binding pocket and is therefore a competitive inhibitor of the enzyme.[50] FGD was determined to be a 78 kDa homodimer possessing an α/β triosephosphateisomerase (TIM) barrel motif (Figure 1.8A), with each monomer weighing approximately 39 kDa. The binding of the F_{420} cofactor within the FGD active site is characterized by a unique non-prolyl *cis*-peptide bond which forms a bulge directed towards the F_{420} binding site, causing the 5'-deazaisoalloxazine chromophore buried in the active site to adapt a butterfly conformation.[50] Some active site amino acid residues that were thought to be essential for catalysis were also identified from the crystal structure (Figure 1.8B).

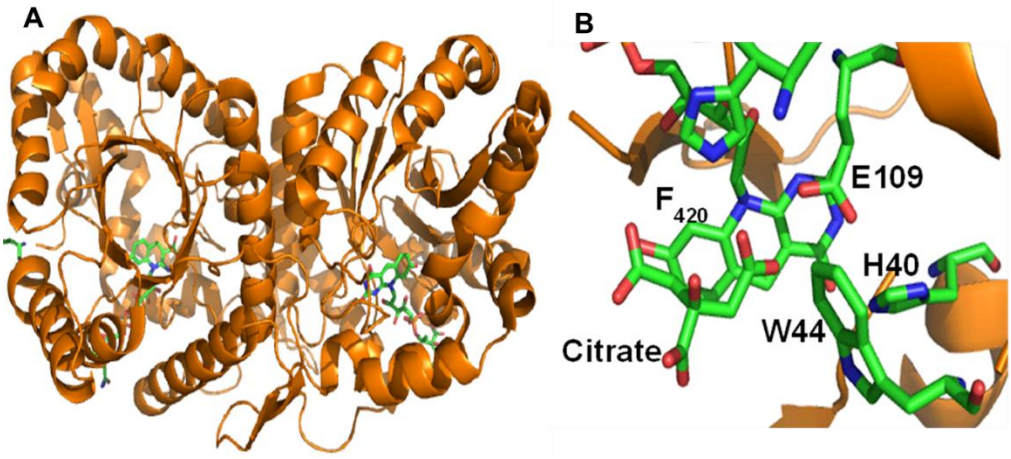

Figure 1.8 Crystal structure of FGD solved at 1.95 Å resolution (PDB # 3C8N). **A**: ribbon structure showing the TIM barrel motif and the F_{420} cofactor bound in the active site. **B**: FGD active site showing the bound cofactor, citrate and some conserved amino acid residues.[50]

1.3.3 FGD proposed mechanism

Based on the crystal structure, the Baker group also proposed a plausible mechanism for the FGD reaction (Figure 1.9). They suggested that Histidine 40 (His40) acts as the active site base which initiates the FGD reaction by abstracting a proton from the C1 hydroxyl group of G6P (Figure 1.9). The next step is the hydride transfer from C1 of G6P to C5 of the F_{420} cofactor, yielding 6-phosphogluconolactone (Figure 1.9). The final step is protonation at N1 of the pyrimidine ring by Glutamate 109 (Glu109), yielding the reduced cofactor $F_{420}H_2$ (Figure 1.9). The Tryptophan 44 (Trp44) and Glutamate 13 (Glu13) residues are thought to be responsible for stabilizing intermediates that are formed during the FGD reaction.[50] We have since investigated this proposed mechanism and our findings are discussed in Chapter 2.

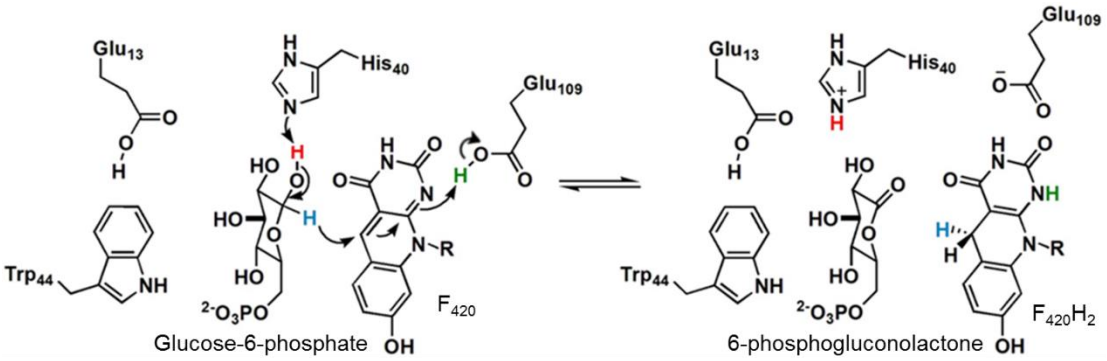

Figure 1.9 The proposed mechanism for the FGD catalyzed reaction. His40 abstracts a proton from C1 hydroxyl of G6P, followed by a hydride transfer from C1 of G6P to C5 of the cofactor. Finally, the N1 of the F_{420} cofactor gets protonated by Glu109.[50]

1.4 Implications of FGD on Tuberculosis disease (TB)

Tuberculosis (TB) is a deadly disease caused by the *M. tuberculosis* bacteria. The bacteria primarily attacks the lungs, but the infection can spread to other parts of the body such as the brain, spine and kidneys. The bacteria can remain dormant for long periods of time (Latent TB) before it eventually causes TB disease. People with Latent TB have a 10% chance of getting TB disease, but those with compromised immune systems due to conditions such as HIV, diabetes or malnutrition are more likely to get TB disease than their healthier counterparts.[51] TB infections are prevalent all over the world, with Asia and Africa recording ~ 87% of total cases reported in 2015.[51] HIV and TB co-infection is a fatal combination since both diseases accelerate the progression of each other. In fact, TB is the leading cause of death for HIV-infected people, making up ~ 35% of all HIV deaths reported in 2015.[51]

While TB is treatable and curable, the current WHO approved treatment regimen is 6 months long and consists of a cocktail of four antimicrobial drugs; Isoniazid (Figure 1.10A), Pyrazinamide (Figure 1.10B), Ethambutol (Figure 1.10C) and Rifampin (Figure 1.10D). Isoniazid and Ethambutol were introduced in 1952 and 1961 respectively, and they both work by inhibiting synthesis of the *M. tuberculosis* cell wall.[52] Pyrazinamide was approved in 1952 and it kills the bacteria by causing pH imbalance, inhibiting fatty acid synthase, and preventing protein translation. Finally, Rifampin acts by inhibiting RNA synthesis, and was approved in 1966.[52] Evidently, no new TB drug has been introduced to the pharmaceutical market in over 50 years, mostly due to the constant evolution of *M. tuberculosis* which has resulted in occurrences of Multi-Drug Resistant (MDR) and Extremely Drug Resistant (XDR) TB.

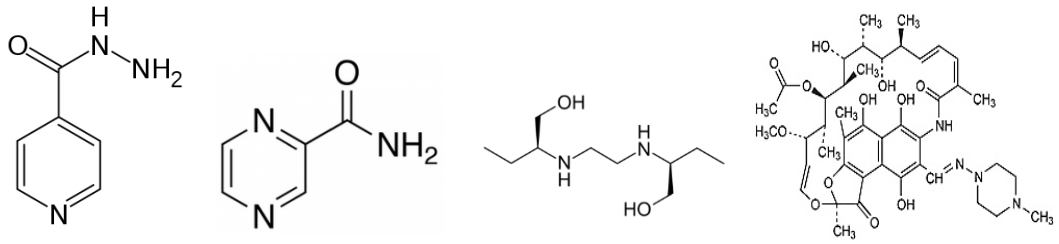

Figure 1.10 Antimicrobial drugs used for TB treatment. **A**: Isoniazid, **B**: Pyrazinamide, **C**: Ethambutol, **D**: Rifampin.[52]

PA-824 (Pretomanid) is a promising tuberculosis drug currently in phase III of clinical trials. PA-824 is a nitroimidazopyran compound that has been shown to be active against both replicating and hypoxic non-replicating *M. tuberculosis*.[53,54] PA-824 is a prodrug that is activated in an $F_{420}H_2$-dependent reaction catalyzed by the enzyme deazaflavin dependent nitroreductase (Ddn) (Figure 1.11).[46,49] Previous investigations of the mechanism of action of PA-824 reveal that it kills *M. tuberculosis* by causing nitrosative stress from NO, which is a byproduct of the PA-824 activation reaction (Figure 1.11).[55,56] FGD is essential for the activation of PA-824 since the $F_{420}H_2$ used by Ddn is produced only from the FGD reaction. Consequently, though not directly, FGD plays a significant role in the rigorous efforts towards the development of novel TB drugs.

1.5 Conclusion

In this chapter, the F_{420} cofactor has been shown to be essential in a variety of organisms and enzymes. It's chemical and physical properties have been clearly discussed to show its uniqueness as a flavin analog cofactor. The FGD enzyme has also been discussed in detail, and its role in the survival of *M. tuberculosis* has been presented. The

subsequent chapters will be focused on the characterization of FGD to further understand its mechanism of action.

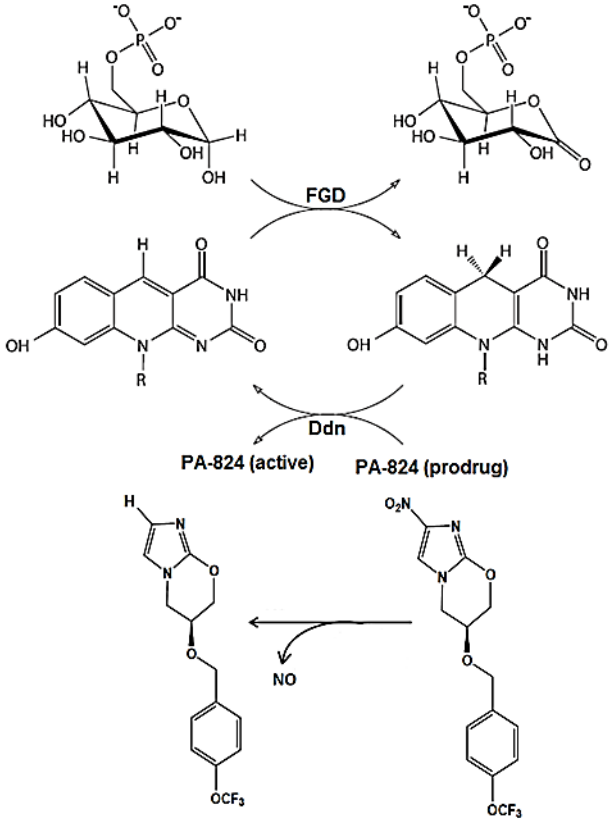

Figure 1.11 The role of FGD in the deazaflavin-dependent nitroreductase (Ddn) activation of PA-824 (Pretomanid). Ddn uses the reduced cofactor to donate a hydride to the C2 position of the PA-824 prodrug, resulting in the release of NO which in turn causes respiratory poisoning to the bacteria.[46,49,55,56]

Chapter 2

INVESTIGATING THE REACTION MECHANISM OF F_{420}-DEPENDENT GLUCOSE-6-PHOSPHATE DEHYDROGENASE FROM *MYCOBACTERIUM TUBERCULOSIS*: KINETIC ANALYSIS OF THE WILD-TYPE AND MUTANT ENZYMES

2.1 Introduction

Tuberculosis (TB) is the world's leading killer due to a bacterial infection. The 2014 statistics reported by the World Health Organization estimates that 9.6 million people were infected and 1.1 million of those infections led to death.[51] These current data show that TB now rivals HIV/AIDS, which caused 1.2 million deaths in 2014.[51] Since latent TB can lead to active TB disease if a host's immune system is weakened, carriers of the HIV virus are at a great risk of developing TB-HIV coinfections, which accounted for 33% of the TB-related deaths in 2014.[51] *Mycobacterium tuberculosis* (*M. tuberculosis*) is the bacterium that causes TB disease and its constant evolution has led to the emergence of multidrug resistant (MDR) and extensively drug resistant (XDR) TB, thus increasing the required period of treatment from 6 months to 2-4 years.[52]

In order to treat MDR- and XDR-TB, a number of promising nitro-imidazole pro-drugs are currently in clinical trials.[54,57] Pretomanid (PA-824)[46,49] is a nitro-imidazole pro-drug that requires activation within *M. tuberculosis*, in a process that is dependent on the cofactor F_{420}. Based on this mechanism, F_{420}-dependent glucose-6-phosphate dehydrogenase (FGD, we have removed the suffix 1 from the original annotation as previously suggested[58]) produces the reduced cofactor, $F_{420}H_2$, which is then used by a deazaflavin-dependent nitroreductase (Ddn) to activate the pro-drug.[6] Cofactor F_{420} is a hydride carrier that not only plays a substantial role in the oxidoreductive reactions of *M. tuberculosis*[59] but also protects the bacteria from nitrosative and oxidative stress.[33,60,61]

The reaction catalyzed by FGD is crucial in *M. tuberculosis* metabolism, being the only known source of the reduced $F_{420}H_2$ within the bacteria.[47,58] FGD is a unique enzyme that uses the cofactor F_{420}, unlike other glucose-6-phosphate dehydrogenases (G6PDs) that utilize either $NADP^+$ or NAD^+.[62-66] FGD is involved in the first committed step of the pentose-phosphate pathway, where it catalyzes the oxidation of glucose-6-phosphate (G6P) to 6-phosphogluconolactone (Figure 1.7). During the FGD reaction, a hydride ion is transferred from C1 of G6P to C5 of the cofactor F_{420}, thus yielding reducing equivalents in the form of $F_{420}H_2$.[50] The *Si*-face stereospecificity of the hydride transfer with respect to C5 of the F_{420} cofactor is a characteristic that has been found to be common for all F_{420}-dependent enzymes.[37,38,67,68]

The crystal structure of wild-type FGD from *M. tuberculosis* has been previously determined to 1.9 Å resolution in the presence of the cofactor F_{420} and the competitive inhibitor, citrate (Figure 1.8).[50] The three-dimensional structure revealed that FGD is a homodimer with an $(\alpha/\beta)_8$ TIM barrel fold. A mechanism has been proposed for the reaction catalyzed by FGD, based on the crystal structure of FGD in complex with F_{420}. In this mechanism, the His40 residue acts as the active site base that abstracts the proton from C1-OH of G6P, thus facilitating the hydride transfer from C1 of G6P to C5 of F_{420}. Glu109 then protonates F_{420} at the N1 position, thus yielding the reduced cofactor $F_{420}H_2$ (Figure 1.9).*[18]* The Trp44 residue is thought to play a role in stabilizing intermediates that are formed in the course of the FGD reaction.[50] Until now, there has been no experimental evidence supporting this proposed mechanism.

Here, we have investigated the roles of these active site residues in FGD catalysis using site-directed mutagenesis to create five FGD variants: H40A, W44F, W44Y, W44A, and E109Q. The wild-type enzyme and these five variants have been characterized by fluorescence binding assays, steady-state kinetics, pH-dependence studies, and pre-

steady state kinetics experiments. Here, we present kinetic evidence that His40, Trp44 and Glu109 indeed play significant roles in FGD catalysis. We also report for the first time, the pH-dependence of catalytic parameters for the FGD reaction. Finally, we present the first observation of biphasic kinetics in FGD, a phenomenon that has only been observed in one other F_{420}-dependent enzyme.[2]

2.2 Materials and Methods

2.2.1 Reagents

The cofactor F_{420} was prepared as previously described, with a tail length of 6-9 γ-glutamate residues, typical of mycobacteria,[15] G6P was purchased from USB Corporation. Sodium chloride, β-mercaptoethanol (βME), imidazole, sodium acetate, Bis-Tris and Tris buffers were purchased from Fisher Scientific.

2.2.2 Site-directed mutagenesis

The open reading frame encoding wild-type FGD has been previously cloned into the *E. coli*-mycobacterial shuttle vector, pYUB1049.[69] This pYUB1049-*fgd* construct was used as a template to generate various FGD mutant constructs. All FGD variants express the protein with an N-terminal His_6-tag to facilitate subsequent protein purification using immobilized metal affinity chromatography (IMAC). The 5'-phosphorylated primers (Integrated DNA Technologies) were extended using iProof™ high-fidelity DNA polymerase (Bio-Rad) and the primers outlined in Table 2.1. Following thermal cycling, the mutated linear plasmids were treated with DpnI, to digest the parental DNA template. The linear vectors were then made circular using T4 DNA ligase (Roche), before transforming into *E. coli* TOP10 electrocompetent cells. The mutations were subsequently verified using

sequencing with T7 forward and terminator primers at the Centre for Genomics, Proteomics and Metabolomics, School of Biological Sciences at The University of Auckland.

Table 2.1 Primers used in the mutagenesis of FGD constructs.

Construct	Primer Sequences (5'- 3')	
H40A	Forward	ACCGTCAGCGACGCTTTTCAGCCTTGG
	Reverse	CCAAGGCTGAAAAGCGTCGCTGACGGT
W44F	Forward	ATTTTCAGCCTTTCCGCCACCAGGG
	Reverse	GGTCGCTGACGGTCGCGCTG
W44Y	Forward	ATTTTCAGCCTTACCGCCACCAGGG
	Reverse	GGTCGCTGACGGTCGCGCTG
W44A	Forward	TTTCAGCCTGCGCGCCACCAGGGC
	Reverse	GCCCTGGTGGCGCGCAGGCTGAAA
E109Q	Forward	CAGGCGCTGAACGAAATCGCCAC
	Reverse	ACCGGTGCCCACGCCAAGGAAAA

2.2.3 FGD expression and purification

The wild-type and mutant constructs of FGD were electroporated into *M. smegmatis* ($mc^2$4517) cells for protein expression. All purification steps were carried out at 4 °C, using a previously reported method with slight modifications.[69] Briefly, the *M. smegmatis* cells expressing various FGD constructs were resuspended in lysis buffer containing 50 mM Tris-HCl (pH 7.0), 150 mM NaCl, 1 mM βME and 10 mM imidazole. The cells were lysed by sonication and then centrifuged for 45 minutes (16,000 x g). The resulting supernatant was then loaded onto a 2.5 x 3 cm Ni-NTA column (Thermo Scientific), previously equilibrated with 4 column volumes of the lysis buffer. The column was then washed with 4 column volumes of wash buffer containing 50 mM Tris-HCl (pH

7.0), 150 mM NaCl, 1 mM βME and 25 mM imidazole, and then eluted with a 25-500 mM imidazole gradient. The active fractions were collected and concentrated by filtration (Millipore, 30 kDa molecular weight cut-off) to about 2 mL and then loaded onto a 1 x 20 cm size-exclusion column (Sephacryl S-200 HR, GE Healthcare), previously equilibrated with 2 column volumes of 50 mM Tris-HCl (pH 7.0). The column was then eluted with 2 column volumes of the same buffer and the purity of the protein was confirmed using SDS-PAGE. The protein was then concentrated and stored at -80 °C in 50 mM Tris-HCl (pH 7.0) buffer until needed.

2.2.4 Fluorescence binding experiments

Fluorescence spectroscopy was used to determine the G6P and F_{420} dissociation constants (K_d) for the FGD wild-type and mutant constructs. A Spectrosil® Quartz sub-micro cell (160 µl nominal volume) from Starna Cells was used to monitor the binding assays at 22 °C on a Horiba FluoroMax Spectrofluorometer, with the excitation and emission slit widths set at 4 and 8 nm, respectively. All binding assays were performed in 50 mM Tris-HCl, pH 7.0. To obtain the K_d of F_{420}, increasing concentrations of F_{420} in either 1 or 2 µL aliquots were titrated into a solution containing 350 nM FGD, to final F_{420} concentrations of 0.05-8.8 µM. The samples were excited at 290 nm and the emission scan was performed from 310 nm–500 nm. The K_d for G6P was also determined under similar conditions by titrating 1 or 2 µL aliquots of G6P into a solution containing 350 nM FGD, to final G6P concentrations of 2-371 µM. Each experiment was conducted in duplicate. A decrease in tryptophan emission at 340 nm was observed for both F_{420} and G6P titration and was used for calculation of the dissociation constants.[2,70,71] In order to investigate the effect of NaCl concentration on the binding affinity of F_{420} and G6P, the wild-type FGD binding assays were performed in 50 mM Tris-HCl, pH 7.0, containing either 150 mM or 300 mM NaCl.

To obtain the K_d values for F_{420}, plots of F/F_{max} *vs* concentration of unbound F_{420} were fitted to a hyperbolic function (Equation 2.1) using SigmaPlot (Systat Software, Inc., San Jose, CA, USA) version 13.0,

$$F/F_{max} = F_{max}\,[F_{420}]_{free}/(K_d + [F_{420}]_{free}) \qquad \text{Equation 2.1}$$

where F/F_{max} is the fractional saturation compared with a solution of 350 nM FGD alone, F_{max} is the maximum fractional saturation (F_{max} = 1), K_d is the dissociation constant, and $[F_{420}]_{free}$ is the concentration of unbound cofactor. $[F_{420}]_{free}$ was determined by subtracting fraction of bound F_{420} from total F_{420} as follows: $([F_{420}]_{total})-((F/F_{max})*[FGD]_{total})$, where $[F_{420}]_{total}$ is the total F_{420} concentration and $[FGD]_{total}$ is the total enzyme concentration, and $((F/F_{max})*[FGD]_{total})$ is the fraction of bound F_{420}. Both F_{420} and FGD concentrations were corrected for dilution during titration.

To obtain K_d values for G6P, plots of F/F_{max} *vs* G6P concentration were fitted to a hyperbolic function (Equation 2.2) using SigmaPlot (Systat Software, Inc., San Jose, CA, USA) version 13.0,

$$F/F_{max} = F_{max}\,[G6P]/(K_d + [G6P]) \qquad \text{Equation 2.2}$$

where F/F_{max} is the fractional saturation compared with a solution of 350 nM FGD alone, [G6P] is the substrate concentration, F_{max} is the maximum fractional saturation (F_{max} = 1), and K_d is the dissociation constant. Both G6P and FGD concentrations were corrected for dilution during titration.

2.2.5 FGD steady state kinetics

The steady state kinetic measurements were carried out in a Spectrosil® Quartz sub-micro cell (160 µl nominal volume) from Starna Cells using a Cary 100 UV-Visible spectrophotometer. To determine the G6P kinetic parameters, the reactions were performed in 50 mM Tris-HCl, pH 7.0 using a constant F_{420} concentration of 20 µM while varying the G6P concentrations (0.008-2 mM). To determine the F_{420} kinetic parameters,

the reactions were performed in 50 mM Tris-HCl, pH 7.0 using a constant G6P concentration of 2 mM while varying the F_{420} concentrations (1–10 μM). The wild-type FGD reactions were initiated by adding enzyme to a final concentration of 25 nM. The FGD W44F, W44Y and E109Q reactions were initiated by adding enzyme to a final concentration of 10 nM, 1 μM, and 4 μM respectively. The FGD W44A and H40A reactions were both initiated with an enzyme concentration of 10 μM. The reactions were monitored by following the reduction of the F_{420} cofactor at 420 nm. Plots of rate constant *vs* substrate concentration were fitted to a hyperbolic function (Equation 2.3) using SigmaPlot (Systat Software, Inc., San Jose, CA, USA) version 13.0.

$$k = k_{cat}[S]/(K_m+[S]) \qquad \text{Equation 2.3}$$

where, k is the rate constant obtained by dividing the initial rate by the enzyme concentration, k_{cat} is the turnover number, K_m is the Michaelis-Menten constant, and [S] is concentration of either G6P or F_{420}.

2.2.6 FGD pH dependence studies

The pH-dependence experiments were conducted for wild-type FGD and its H40A and E109Q variants using the following buffers: 50 mM sodium acetate (pH 5.0 and 5.5), 50 mM Bis-Tris (pH 6.0 and 6.5), and 50 mM Tris-HCl (pH 7-9). The experiments were conducted under the steady state conditions described in the previous section, by varying the G6P concentration over the range 0.008 to 2 mM while keeping the F_{420} concentration constant at 20 μM. The reduction of the F_{420} cofactor at pH 5.0-6.5 and pH 7.0-9.0 were monitored at 400 nm and 420 nm, respectively.[1] Plots of rate constant *vs* substrate concentration were fitted to Equation 3 in order to obtain k_{cat} and K_m at each pH for each of the three enzymes. pK values were determined by fitting pH-rate profiles of log k_{cat} or log k_{cat}/K_m to equations for curves with one proton transition (Equation 2.4) or two proton

transitions (Equations 2.5, 2.6 and 2.7), where Y is k_{cat} or k_{cat}/K_m, Y_H and Y_L are the maximum and minimum pH-independent values of Y respectively, K_1 and K_2 are acid dissociation constants for the ascending and descending limbs respecetively, and $[H^+]$ is the proton concentration at each pH. All fits were done using SigmaPlot (Systat Software, Inc., San Jose, CA, USA) version 13.0.

$$\log Y = \log \{Y_H / (1+[H^+]/ K_1)\} \quad \text{Equation 2.4}$$

$$\log Y = \log \{Y_H / ((1+[H^+] / K_1) + K_2 /[H^+])\} \quad \text{Equation 2.5}$$

$$\log Y = \log \{Y_H / ((1+[H^+] / K_1) + K_1 /[H^+])\} \quad \text{Equation 2.6}$$

$$\log Y = \log \{(Y_H + Y_L([H^+] / K_1)) / ((1+[H^+] / K_1) + K_2 /[H^+])\} \quad \text{Equation 2.7}$$

The K_m of the F_{420} cofactor was checked at pH extremes (pH 5.0 and 9.0) in order to verify that the pH dependence observed was strictly due to effects on the G6P substrate. The reactions were performed in the appropriate buffers using a constant G6P concentration of 2 mM while varying the F_{420} concentrations (1 – 10 μM). For the FGD E109Q variant, these experiments were performed over the full pH range (5.0-9.0) in order to determine if this variant displayed pH-dependent allostery with respect to the F_{420} cofactor. The sigmoidal curves obtained for the FGD E109Q variant at pH 7.0-9.0 were fitted to Equation 2.8, where k is the rate constant obtained by dividing the initial rate by the enzyme concentration, k_{cat} is the turnover number, $K_{0.5}$ is the substrate concentration at half of k_{cat}, [S] is concentration of F_{420}, and n is the Hill coefficient.

$$k = k_{cat}[S]^n/(K_{0.5}^n + [S]^n) \quad \text{Equation 2.8}$$

2.2.7 FGD pre-steady state kinetics

The rapid kinetic experiments for wild-type FGD and its variants were performed in a Hitech Scientific DX2 stopped-flow spectrophotometer at 22 °C in 50 mM Tris-HCl, pH 7.0. The multiple turnover experiments were performed by pre-incubating a solution of 12 μM FGD with 40 μM F_{420}, followed by rapid mixing with an equal volume solution of 2 mM G6P. The final reaction concentrations were 6 μM FGD, 20 μM F_{420}, and 1 mM G6P. Time trace measurements were made in diode array mode between 350-800 nm following F_{420} reduction at 420 nm. Plots of absorbance at 420 nm *vs* time were fitted using SigmaPlot (Systat Software, Inc., San Jose, CA, USA) version 13.0. Plots that revealed a single reaction phase were fitted to a single 3-parameter exponential decay function (Equation 2.9), where A is the highest absorbance, A_1 is the change in absorbance, k_{obs} is the apparent rate constant, t is the reaction time, and c is the absorbance at infinite time. Plots that revealed two reaction phases were fitted to a double 5-parameter exponential decay function (Equation 2.10), where A is the highest absorbance, A_1 and A_2 are the changes in absorbance for the fast and slow phase respectively, k_{obs1} and k_{obs2} are the apparent rate constants for the fast and slow phase respectively, t is the reaction time, and c is the absorbance at infinite time.

$$A = A_1 \cdot e^{-k_{obs} \cdot t} + c \qquad \text{Equation 2.9}$$

$$A = A_1 \cdot e^{-k_{obs1} \cdot t} + A_2 \cdot e^{-k_{obs2} \cdot t} + c \qquad \text{Equation 2.10}$$

The single turnover experiments were performed under similar conditions, by pre-incubating 100 μM FGD with 10 μM F_{420} and mixing rapidly with an equal volume solution of 1 mM G6P solution. The final concentrations for the single turnover kinetics were 50 μM FGD, 5 μM F_{420}, and 500 μM G6P. The single turnover plots of absorbance at 420 nm *vs* time were all fitted to Equation 2.8 using SigmaPlot (Systat Software, Inc., San Jose, CA, USA) version 13.0.

2.3 Results

2.3.1 FGD expression and purification

A subunit molecular mass of ~39 kDa was estimated from the SDS-PAGE gel of the various purified FGD enzymes (Figure 2.1).

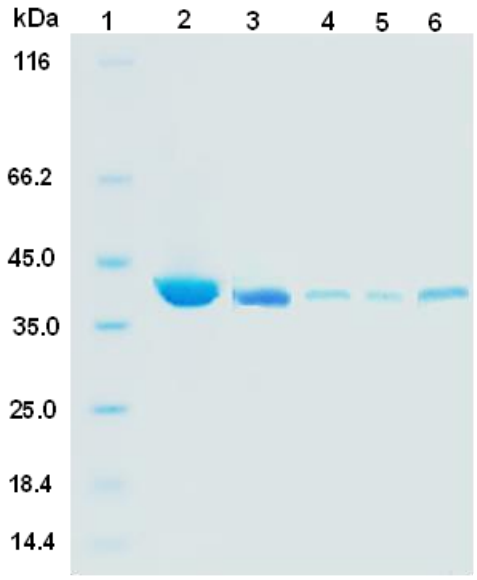

Figure 2.1 SDS-PAGE of purified FGD samples from the SEC column. **Lane 1**: protein molecular weight marker; **Lane 2**: wild-type FGD (7 µg); **Lane 3**: FGD W44F (5 µg); **Lane 4**: FGD W44F (2 µg); **Lane 5**: FGD E109Q (2 µg); **Lane 6**: FGD H40A (4 µg).[72]

2.3.2 Binding of F_{420} and G6P to FGD

A decrease in tryptophan fluorescence intensity at 340 nm was observed upon addition of increasing concentrations of the cofactor F_{420} into FGD solutions (Figure 2.2, panel A). The plot of fractional saturation *vs* unbound cofactor yielded K_d values for F_{420} binding of 6.6 ± 0.1 nM for wild-type FGD (Figure 2.2, panel B). Compared to wild-type FGD, all the variants had higher F_{420} K_d values (Table 2.2). FGD W44Y had the largest F_{420} K_d value, which was 180-fold higher than for wild-type FGD. FGD W44F had the least effect

on F_{420} K_d value, with only a 3-fold higher F_{420} K_d. FGD W44A, E109Q, and H40A had 18-, 75-, and 22-fold higher F_{420} K_d values, respectively. See Appendix A (Figure A.1) for the FGD variants F_{420} binding curves.

A similar decrease in tryptophan fluorescence intensity at 340 nm was revealed when increasing concentrations of G6P were titrated into FGD solutions (Figure 2.2, panel C). The fractional saturation was plotted against G6P concentration and the curve was fitted to Equation 2. The K_d value obtained for G6P binding was 17 ± 4 μM for wild-type FGD (Figure 2.2, panel D). Very similar G6P K_d values were obtained for the various mutant FGD enzymes (Table 2.2) which are all equal within error. See Appendix A (Figure A.2) for the FGD variants G6P binding curves.

The effects of NaCl concentration on F_{420} and G6P dissociation constants were analyzed by repeating the wild-type FGD binding experiments in assay buffer containing either 150 mM or 300 mM NaCl. The F_{420} K_d values at NaCl concentrations of 150 mM and 300 mM were 92 ± 17 nM, and 250 ± 37 nM, respectively. The G6P K_d values at NaCl concentrations of 150 mM and 300 mM were 13 ± 2 μM, and 14 ± 1 μM, respectively.

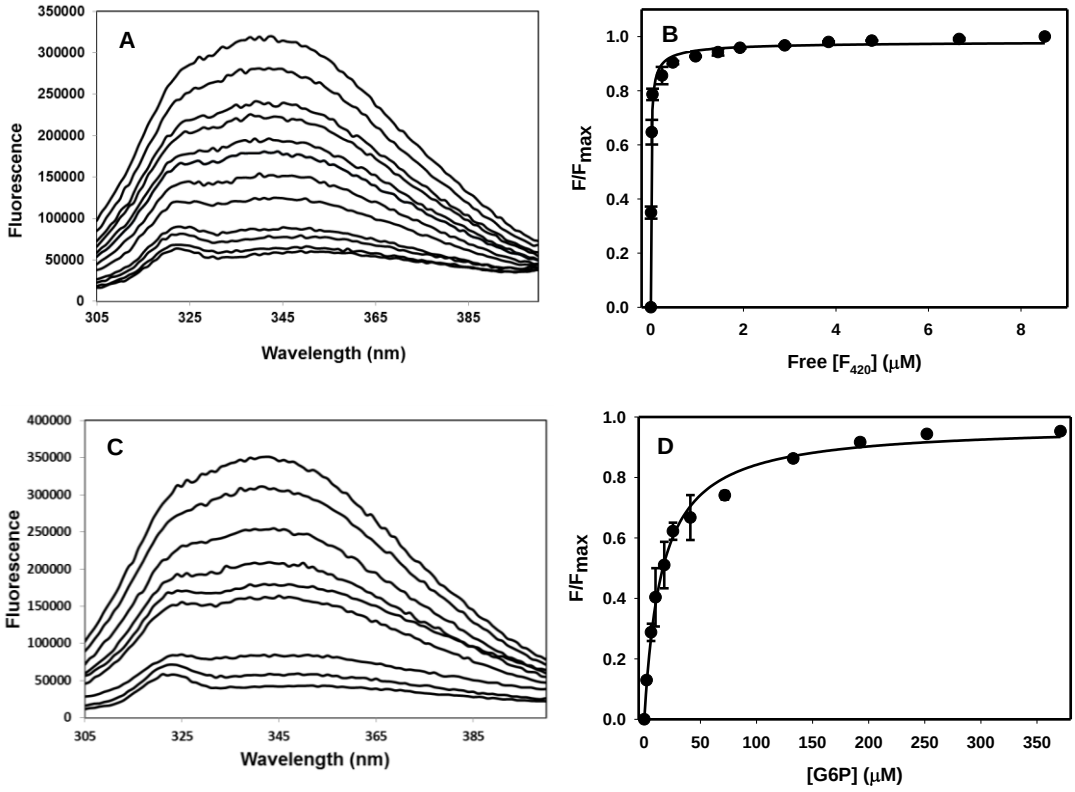

Figure 2.2 Binding of F_{420} and G6P to FGD as measured by tryptophan fluorescence. The assays for F_{420} and G6P binding to FGD were carried out in 50 mM Tris-HCl (pH 7.0) buffer at 22 °C. A 350 nM FGD solution was titrated with increasing concentrations of F_{420} or G6P and the samples were excited at 290 nm while the emission was monitored at 340 nm. **A**: emission spectra of wild-type FGD containing 0, 0.05, 0.28, 0.53, 0.78, 1.8, 2.2, 3.2, 4.2, 5.1, 7.0, and 8.8 μM of F_{420} (upper to lower spectra respectively). **B**: plot of F/F_{max} *vs* free F_{420} concentration for wild-type FGD. The solid circles represent an average of two measurements of F/F_{max} at various concentrations of unbound F_{420} and the solid line represents fit to Equation 2.1. **C**: emission spectra of wild-type FGD containing 0, 2.0, 6.0, 17.8, 41.0, 72.0, 133, 193, and 371 μM of G6P (upper to lower spectra respectively). **D:** plot of F/F_{max} *vs* G6P concentration for wild-type FGD. The solid circles represent an average of two measurements of F/F_{max} at various concentrations of G6P and the solid line represents fit to Equation 2.2. The error bars in the plots represent standard deviations obtained from duplicate measurements of each ligand concentration.[72]

Table 2.2 Binding constants for FGD wild-type and variants. The assays for F_{420} and G6P binding to FGD were carried out in 50 mM Tris-HCl (pH 7.0) buffer at 22 °C. A 350 nM FGD solution was titrated with increasing concentrations of F_{420} or G6P and the samples were excited at 290 nm while the emission was monitored at 340 nm. The F_{420} and G6P K_d values were obtained from fits to Equation 2.1 and Equation 2.2, respectively.[72]

FGD	$^{G6P}K_d$ (μM)	$^{F_{420}}K_d$ (nM)
Wild-type	17 ± 4	6.6 ± 0.1
W44F	19 ± 2	22 ± 9
W44Y	19 ± 2	1170 ± 174
W44A	14 ± 2	122 ± 27
E109Q	17 ± 2	498 ± 52
H40A	10 ± 1	149 ± 20

2.3.3 FGD steady state kinetics

The plots of rate constant *vs* G6P concentration for wild-type FGD and the variants displayed classic Michaelis-Menten saturation kinetics (Figure 2.3A). See Appendix B (Figure B.1) for the FGD variants steady state kinetic plots with respect to G6P.The plots were fitted to a hyperbolic function (Equation 2.3) in order to determine the apparent G6P kinetic parameters, which are presented in Table 2.3. Compared to wild-type FGD, all the variants had lower k_{cat} values with the exception of FGD W44F, which had a 2-fold higher k_{cat}. FGD H40A and W44A had 1000-fold lower k_{cat} values, while FGD W44Y and E109Q k_{cat} values were 34- and 60-fold lower than wild-type FGD, respectively. The G6P K_m values were similar for wild-type FGD and FGD H40A. Compared to wild-type enzyme, FGD W44F, W44Y, W44A and E109Q variants had 16-, 8-, 13-, and 4-fold higher G6P K_m values, respectively.

The plots of rate constant *vs* F_{420} concentration for wild-type FGD and the FGD variants also displayed classic Michaelis-Menten saturation kinetics (Figure 2.3B). See Appendix B (Figure B.2) for the FGD variants steady state kinetic plots with respect to F_{420}. The apparent F_{420} kinetic parameters are shown in Table 2.3. For all six FGD enzymes, the k_{cat} values in response to varying F_{420} were very similar to the values obtained when G6P was varied. When compared with wild-type FGD, the W44F, W44Y and E109Q variants all had 2-fold higher F_{420} K_m values. The F_{420} K_m for H40A variant was 4-fold higher, while F_{420} K_m was 3-fold lower in W44A than wild-type FGD.

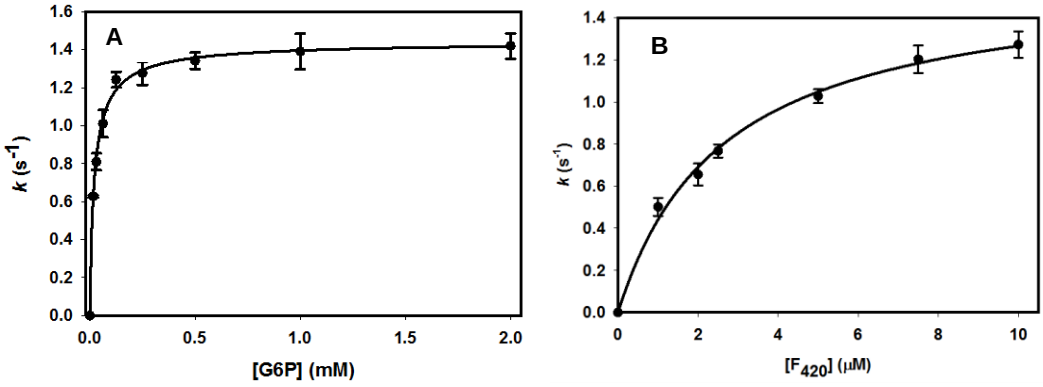

Figure 2.3 Steady state kinetics plots for wild-type FGD. The experiments were carried out in 50 mM Tris-HCl (pH 7.0) at 22 °C. The reactions were monitored by following the reduction of the F_{420} cofactor at 420 nm. The rate constants were obtained by dividing initial rates by enzyme concentration. **A**: Plot of rate constant *vs* G6P concentration. The solid circles represent an average of two measurements of rate constants at various concentrations of G6P and the solid line represents fit to Equation 2.3. **B**: Plot of rate constant *vs* F_{420} concentration. The solid circles represent an average of two measurements of rate constants at various concentrations of F_{420} and the solid line represents fit to Equation 2.3. The error bars in the plots represent standard deviations obtained from duplicate measurements of each variable substrate concentration.[72]

Table 2.3 Apparent steady-state kinetics parameters for FGD wild-type and variants. The apparent kinetic parameters presented here are reasonable approximations of the true values. The experiments were carried out in 50 mM Tris-HCl (pH 7.0) at 22 °C. The reactions were monitored by following the reduction of the F_{420} cofactor at 420 nm. The apparent kinetic parameters k_{cat} and K_m, along with their uncertainties, were obtained by fitting the plots to Equation 2.3.[72]

a The uncertainties for the catalytic efficiency values were calculated using the formula $\{((K_{m\ (err)}/\ K_m)^2 + (k_{cat\ (err)}/\ k_{cat})^2)^{1/2} * (k_{cat}\ /\ K_m)\}$, where $K_{m\ (err)}$ and $k_{cat\ (err)}$ represent the uncertainties in the individual K_m and k_{cat} values.

b Denotes $K_{0.5}$ obtained from fit to Equation 2.8.

c Denotes $k_{cat}\ /K_{0.5}$.

FGD	$^{G6P}k_{cat,\ app}$ (s^{-1})	$^{F_{420}}k_{cat,\ app}$ (s^{-1})	$^{G6P}K_{m,\ app}$ (μM)	$^{F_{420}}K_{m,\ app}$ (μM)	$^{G6P}k_{cat}/K_m$ [a] ($M^{-1}s^{-1}$)	$^{F_{420}}k_{cat}/K_m$ [a] ($M^{-1}s^{-1}$)
Wild-type	1.4 ± 0.1	1.4 ± 0.3	22 ± 2	2.6 ± 0.3	(6.0 ± 0.5) x 10^4	(6.0 ± 1) x 10^5
W44F	3.5 ± 0.1	3.2 ± 0.3	335 ± 35	5.4 ± 1.0	(1.0 ± 0.1) x 10^4	(6.0 ± 1) x 10^5
W44Y	0.041 ± 0.001	0.060 ± 0.01	171 ± 17	4.2 ± 0.8	(2.0 ± 0.2) x 10^2	(2.0 ± 0.4) x 10^4
W44A	0.0012 ± 0.0003	0.0010 ± 0.0003	278 ± 36	0.9 ± 0.2	4.0 ± 1	(1.0 ± 0.5) x 10^3
E109Q	0.023 ± 0.002	0.020 ± 0.003	41 ± 12	5.6 ± 1.0[b]	(1.0 ± 0.5) x 10^2	(4.0 ± 0.8) x 10^3 [c]
H40A	0.0016 ± 0.0001	0.0020 ± 0.0001	27 ± 5	8.0 ± 2.0	(6.0 ± 1) x 10^1	(4.0 ± 0.6) x 10^2

2.3.4 FGD pH dependence

Experiments to study pH-dependence for wild-type FGD and its E109Q and H40A variants were conducted over the pH range 5.0-9.0, by varying the G6P concentration and holding the F_{420} concentration constant. The log k_{cat}-pH profile for wild-type FGD was bell-shaped with optimal activity at pH 7.0 and slopes of +1 and -1 on the

acidic and basic limbs respectively (Figure 2.4A), suggesting that two ionizations are involved in the turnover of the enzyme-substrate complex. The fit of the wild-type FGD log k_{cat} *vs* pH profile to Equation 2.5 yielded wild-type FGD pK_1 and pK_2 values of 6.5 ± 0.3 and 8.0 ± 0.3, respectively. The FGD E109Q log k_{cat}-pH profile displayed a sigmoidal curve with a plateau between pH 6-7 and increased activity between pH 8-9 (Figure 2.4C). Compared to wild-type FGD, the fit to Equation 2.7 for FGD E109Q yielded a similar pK_2, while the pK_1 value shifted slightly towards acidic pH (Table 2.4). The FGD H40A log k_{cat}-pH profile displayed complete removal of the ionization on the basic limb, resulting in a plateau between pH 7-9 (Figure 2.4E), and a fit to Equation 2.4 yielded a pK_1 value similar to the wild-type FGD pK_1 value in the corresponding profile (Table 2.4). The fit of the bell-shaped log k_{cat}/K_m-pH profiles for wild-type FGD (Figure 2.4B) and FGD H40A (Figure 2.4F) to Equation 2.5 yielded pK_1 and pK_2 values that were too close to distinguish and, therefore, the plots were fitted to Equation 2.6 and yielded similar average pK_1 value of 7.0. The log k_{cat}/K_m-pH profile for FGD E109Q was bell shaped (Figure 2.4D), and a fit to Equation 2.5 gave a pK_1 value similar to wild-type FGD and a pK_2 value that was more basic than the wild-type pK_2 (Table 2.4).

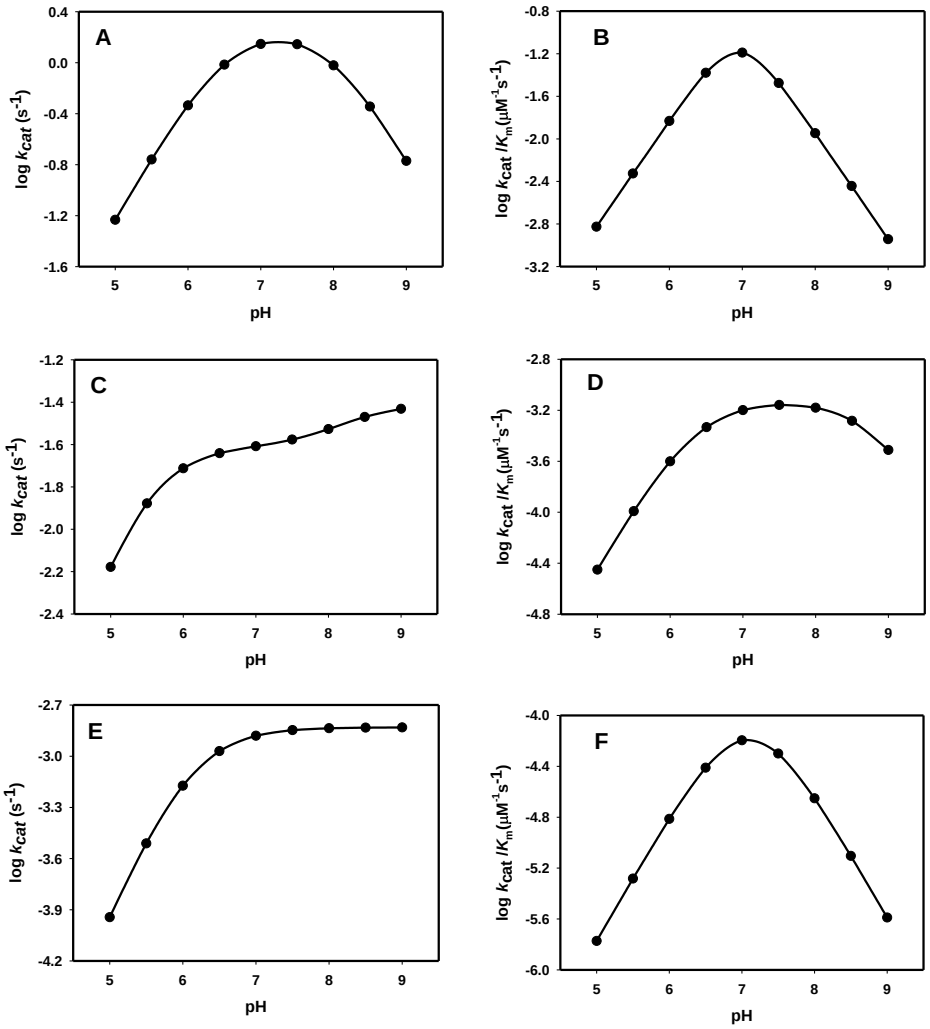

Figure 2.4 pH-rate profiles of log k_{cat} and log k_{cat}/K_m for wild-type FGD (A and B respectively), FGD E109Q (C and D respectively), and FGD H40A (E and F respectively). The pH-dependence studies for the three enzymes were conducted using constant F_{420} concentration (20 μM) and varying G6P concentration (0.008-2 mM) within a pH range of 5.0-9.0. Equations 2.4-2.7 were used to fit the appropriate curves as follows: Equation 2.4 (E), Equation 2.5 (A and D), Equation 2.6 (B and F), and Equation 2.7 (C).[72]

Table 2.4 p*K* values from pH-rate profiles of log k_{cat} and log k_{cat}/K_m for wild-type FGD and its E109Q and H40A variants. The pH-dependence studies for the three enzymes were conducted at 22 °C using a constant F_{420} concentration (20 μM) and varying G6P concentration (0.008-2 mM) within a pH range of 5.0-9.0. The p*K* values were obtained from appropriate fits of the pH-rate profiles to Equations 4-7. The errors reported here were also generated from the appropriate fits to Equations 4-7.[72]

ND: not determined.

FGD	Log k_{cat}-pH		Log k_{cat}/K_m-pH	
	pK_1	pK_2	pK_1	pK_2
Wild-type	6.5 ± 0.3	8.0 ± 0.3	7.0 ± 0.03	7.0 ± 0.03
E109Q	5.4 ± 0.3	8.3 ± 0.7	6.3 ± 0.2	8.8 ± 0.2
H40A	6.1 ± 0.2	ND	7.0 ± 0.01	7.0 ± 0.01

In order to confirm that the pH dependence was completely due to effects of G6P substrate, the K_m of the F_{420} cofactor was determined at pH extremes for the three enzymes. The F_{420} K_m values at pH 5.0 and 9.0 were similar to the F_{420} K_m values at pH 7.0 for both wild-type FGD and FGD H40A (Appendix B, Figure B.3). The FGD E109Q variant displayed classic Michaelis-Menten hyperbolic curves at pH 5.0-6.0, and sigmoidal curves at pH 7.0-9.0 (Figure 2.5). The $K_{0.5}$ values were similar at pH 7.0-9.0 and the K_m values were ~5- and 2-fold lower at pH 5.0 and 6.0 respectively, compared to the $K_{0.5}$. The Hill coefficients were 1.8 ± 0.3, 3.6 ± 0.6 and 3.0 ± 0.4 at pH 7.0, 8.0 and 9.0, respectively. The value of the Hill coefficient evidently increased with increasing pH, thus implying pH-dependent positive kinetic cooperativity in the FGD E109Q variant, with respect to the F_{420} cofactor.

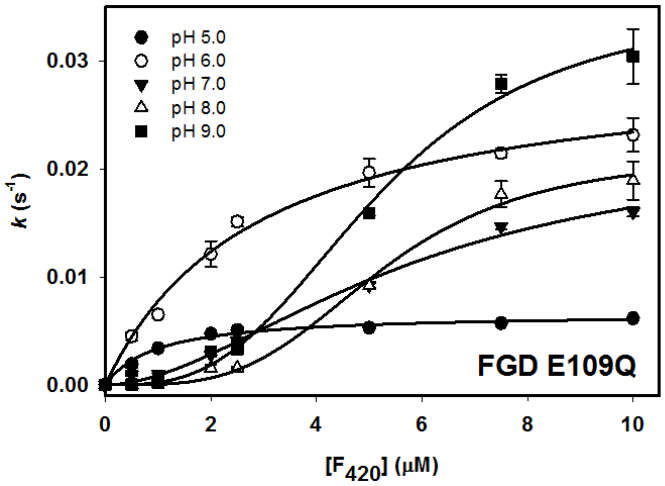

Figure 2.5 FGD E109Q plots of rate constant *vs* F_{420} concentration. The experiments were carried out in appropriate buffers (pH 5.0-9.0) at 22 °C using a fixed G6P concentration and varying F_{420} concentrations. The reactions were monitored by following the reduction of the F_{420} cofactor at 400 nm (pH 5.0-6.0) or 420 nm (pH 7.0-9.0). Each data point represents an average of two measurements of rate constants at various concentrations of F_{420}. The error bars in the plots represent standard deviations obtained from duplicate measurements of each F_{420} concentration.[72]

2.3.5 FGD pre-steady state kinetics

A pre-incubated solution containing FGD and F_{420} was rapidly mixed with equal volumes of a solution containing G6P in the stopped-flow spectrophotometer. The reduction of the F_{420} cofactor was monitored by absorbance changes at 420 nm. The spectra at different time intervals were collected in diode array mode (350 – 800 nm), with no observable peaks for intermediate formation. For the multiple-turnover experiments, the reaction progress monitored at 420 nm revealed a fast phase and a slow phase for wild-type FGD (Figure 2.6A), W44F, W44Y, and E109Q variants. The plots of absorbance at 420 nm *vs* time for these four enzymes were, therefore, fitted to a double exponential decay function (Equation 10). FGD H40A and W44A plots were fitted to a single exponential

decay function (Equation 2.9) since their reactions revealed a single phase. The multiple turnover k_{obs} values are summarized in Table 2.5. See Appendix C (Figure C.1) for the FGD variants multiple turnover curves.

The plots for the single turnover experiments were all fitted to a single exponential decay function (Figure 2.6B;) and the k_{obs} values are also summarized in Table 2.5. Overall, the k_{obs} values in the single turnover conditions are comparatively similar to the multiple turnover k_{obs} values for the fast phase of wild-type FGD, W44F, W44Y, and E109Q. See Appendix C (Figure C.2) for the FGD variants single turnover curves.

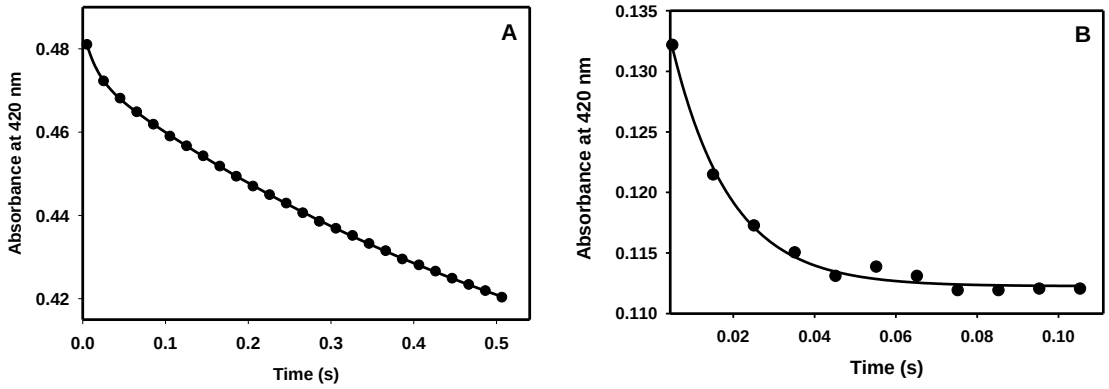

Figure 2.6 Wild-type FGD pre-steady state kinetics plots of absorbance at 420 nm *vs* time. The FGD pre-steady state kinetics experiments were carried out in diode array mode, using 50 mM Tris-HCl (pH 7.0) buffer at 22 °C. **A:** multiple turnover experiment containing 6 µM FGD, 20 µM F_{420} and 1 mM G6P. The plot revealed a fast phase and a slow phase for the reaction. The solid circles represent an average of three absorbance measurements at various times and the solid line represents the fit to Equation 2.10. For the purpose of clarity, only each 10th data point is shown on the plot. **B:** single turnover experiment containing 50 µM FGD, 5 µM F_{420} and 500 µM G6P. The solid circles represent an average of three absorbance measurements at various times and the solid line represents the fit to Equation 2.9.[72]

Table 2.5 Apparent rate constants obtained from pre-steady state kinetics for FGD wild-type and variants. The FGD pre-steady state kinetics experiments were carried out in diode array mode, using 50 mM Tris-HCl (pH 7.0) buffer at 22 °C. Multiple turnover experiment contained 6 µM FGD, 20 µM F_{420} and 1 mM G6P while single turnover experiments contained 50 µM FGD, 5 µM F_{420} and 500 µM G6P. The apparent rate constants were obtained from fits to Equation 2.9 where only a single reaction phase was observed or to Equation 2.10 where two reaction phases were observed. The errors reported here were also generated from the fits to Equation 2.9 and Equation 2.10.[72]

ND: not determined.

FGD	Multiple turnover		Single turnover
	Fast phase k_{obs} (s^{-1})	Slow phase k_{obs} (s^{-1})	k_{obs} (s^{-1})
Wild-type	67 ± 3	1.60 ± 0.02	70 ± 5
W44F	17 ± 1	0.144 ± 0.001	14.5 ± 0.1
W44Y	2.8 ± 0.2	0.065 ± 0.002	5.3 ± 0.2
W44A	ND	0.0172 ± 0.0002	0.11 ± 0.02
E109Q	1.75 ± 0.02	0.104 ± 0.001	1.4 ± 0.1
H40A	ND	0.007 ± 0.001	0.02 ± 0.01

2.4 Discussion

The experiments presented here were aimed at probing the previously proposed mechanism of the FGD reaction.[50] We used site-directed mutagenesis to target three active site residues that are thought to be involved in the FGD reaction. The residue His40 was converted to alanine, thus eliminating the proposed active site base.[50] Trp44, which is thought to stabilize reaction intermediates,[50] was converted to three different residues; phenylalanine to maintain aromaticity, tyrosine for its phenolic side chain, and alanine to eliminate aromaticity. It has also been hypothesized that Glu109 protonates the F_{420}

cofactor at position N1,[50] so this residue was converted to a glutamine, replacing the carboxyl group with a carboxyamide group.

Fluorescence-based binding assays were performed to obtain dissociation constants that would enable appropriate substrate and cofactor concentrations to be chosen for the subsequent kinetic experiments, to ensure saturating conditions and to determine the effects that the FGD variants have on G6P and F_{420} binding, in comparison to wild-type FGD. The K_d values for G6P were approximately equal for the wild-type FGD and all five FGD variants, suggesting that His40, Trp44 and Glu109 do not have critical roles in substrate binding, despite their proximity to the proposed G6P binding site (Table 2.2). The F_{420} K_d values for the four FGD variants, on the other hand, were all significantly higher than that of wild-type FGD (Table 2.2), indicating weaker F_{420} binding. The FGD E109Q variant had 75-fold lower binding affinity for F_{420}, while the F_{420} binding affinity of the H40A variant was 23-fold lower than for wild-type FGD (Table 2.2). Glu109 and His40 help to anchor the F_{420} cofactor into the active site by creating a pocket where its pyrimidine ring binds. Compared to wild-type FGD, the W44Y, W44A and W44F variants had 177-, 18- and 3-fold lower binding affinities for F_{420} (Table 2.2). Trp44 forms a hydrophobic back-stop in the binding pocket and the much lower F_{420} affinity of the W44Y variant, compared with W44F, implies that the phenolic hydroxyl group must destabilize F_{420} binding.

The F_{420} K_d value for wild-type FGD was 6.6 ± 0.1 nM, much lower than the previously reported *M. tuberculosis* wild-type FGD F_{420} K_d value of 4.5 μM, which was obtained in 300 mM NaCl conditions.[50] The significant difference in the F_{420} K_d values obtained under these two different NaCl conditions prompted us to carry out wild-type FGD binding assays at three different NaCl concentrations (0 mM, 150 mM, and 300 mM). The F_{420} K_d value at 300 mM NaCl was 250 ± 37 nM, which is still significantly lower than the 4.5 μM previously published.[18] Overall, the results showed a 14- and 38-fold increase in

F_{420} K_d for the 150 mM and 300 mM NaCl conditions, respectively. Crystal structures of FGD and several other F_{420}-dependent enzymes show that the 5-deazaisoalloxazine chromophore of the F_{420} cofactor is generally buried within the active site while the poly-γ-glutamate tail extends out into the solvent, and helps in anchoring the cofactor into the active site.[43,46,50,73] The observed decrease in F_{420} binding affinity with increasing NaCl concentration could be due to the interaction of sodium ions with the negatively charged poly-γ-glutamate tail of the cofactor F_{420} that is exposed to the solvent. The G6P K_d values at 0 mM, 150 mM and 300 mM were very similar, indicating that NaCl concentration does not affect the binding of G6P to FGD.

The K_m value for G6P obtained for wild-type FGD in our steady-state kinetics studies, conducted in the absence of added NaCl, was 21.6 ± 1.5 μM. This was lower than the previously-determined G6P K_m value of 100 μM, in 50 mM Tris (pH 7.0) containing 300 mM NaCl.[50] We therefore repeated the steady-state kinetics experiments for wild-type FGD with the addition of 300 mM NaCl in the reaction buffer. The G6P K_m value obtained was 100 ± 17 μM (data not shown), fully consistent with the published G6P K_m. [50]

The G6P K_m value obtained for the FGD H40A variant was very similar to the wild-type value (Table 2.3). However, this H40A mutant showed a significant loss of catalytic activity, with a drastic ~900-fold decrease in k_{cat} and ~1000-fold decrease in catalytic efficiency compared to the wild-type FGD (Table 2.3). His40 is close enough to the modeled G6P binding site (Figure 2.7) for proton abstraction from the C1-OH of G6P.*[18]* Other NAD^+ or $NADP^+$ dependent glucose-6-phosphate dehydrogenases have been shown to have conserved histidine residues in their active sites that function either in substrate binding or in acid-base catalysis.[62-66] In the case of FGD, our data show that His40 is involved in catalysis as well as having an indirect role in F_{420} binding. We cannot confirm that His40 is the sole active site base, however, since the E109Q mutant also

shows a large, albeit less dramatic, reduction in k_{cat}. The G6P K_m value for E109Q was 4-fold higher while its k_{cat} value was 140-fold lower than the values for wild-type FGD, resulting in ~500-fold lower catalytic efficiency (Table 2.3). The significant loss of activity for this variant is associated with loss of the ionizable carboxylic side chain, which is proposed to donate a proton to N1 of the F_{420} cofactor. These findings suggest that Glu109 residue also has a role in acid-base catalysis as proposed by Bashiri *et al*.[50]

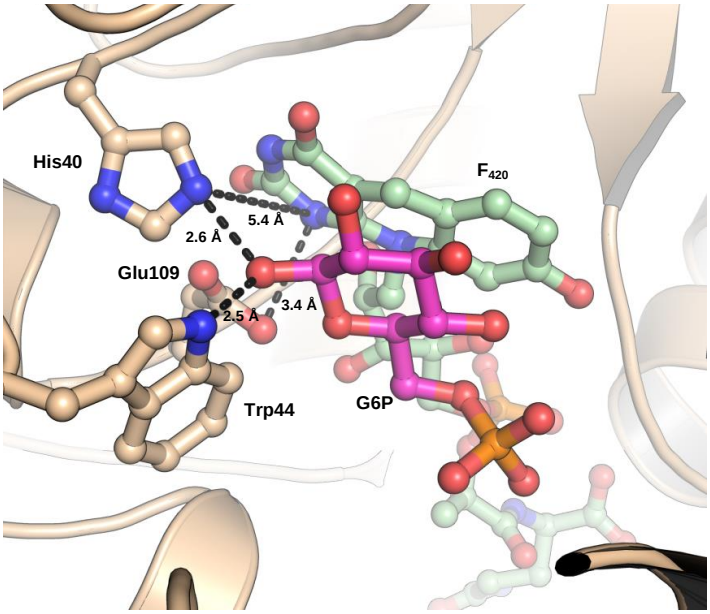

Figure 2.7 Proposed interactions between G6P (magenta), F_{420} (green) and selected active site residues. G6P was docked into the active site to suggest these interactions[18], which are shown in broken lines. The G6P is oriented between F_{420} and Trp44. It has been proposed that His40 abstracts the proton from C1-OH of G6P, while Trp44 stabilizes the reaction intermediate by hydrogen bonding to the negatively charged O during the proton abstraction. The broken lines from His40 and Glu109 to N1 of F_{420} have been used to illustrate the proton donor-acceptor distance and do not imply interactions between these residues and the cofactor.[50]

For the FGD W44Y variant, the G6P K_m was 8-fold higher while the k_{cat} was 34-fold lower, making the variant ~270-fold less efficient than wild-type FGD (Table 2.3). The G6P K_m for FGD W44F was 16-fold higher while the k_{cat} was 2-fold higher, making the variant ~6-fold less efficient than wild-type FGD (Table 2.3). The Trp44 residue has been proposed to be involved in stabilizing FGD reaction intermediates, possibly by hydrogen bonding to a hydroxyl group of the G6P substrate (Figure 2.7).[18] It is easy to see why the W44Y mutation would disrupt productive G6P binding (Figure 2.7) but the lack of a significant effect for the W44F variant would seem to rule out the suggested hydrogen bonding interaction. A significant loss of catalytic activity in the FGD W44A mutant was reflected in a drastic ~1000-fold decrease in k_{cat} and ~2500-fold decrease in catalytic efficiency compared to the wild-type FGD (Table 2.3), revealing that aromaticity at residue 44 is essential for FGD catalysis. Inspection of the FGD structure[18] shows that the aromatic ring plane of residue 44 inserts neatly between His40 and Leu252, adjacent to the cofactor. Loss of this aromatic ring, or replacement with a non-aromatic side chain would disrupt the active site structure significantly and the effects on catalysis due to Trp44 mutations are likely to be due to this rather than loss of the proposed hydroxyl interaction.

The k_{cat} values obtained for all six enzyme variants as the F_{420} concentration was varied were very similar to the k_{cat} values obtained when varying G6P (Table 2.3). The K_m values for the F_{420} cofactor were all slightly higher for the mutants compared to wild-type FGD, with the exception of the W44A variant (Table 2.3). The low F_{420} K_m value for W44A is probably because of the larger F_{420} binding pocket created when aromaticity at residue 44 is eliminated. Overall, as previously observed with varying G6P, all the variants were catalytically less efficient than wild-type FGD.

The pH-rate profiles of some glucose-6-phosphate dehydrogenases have been shown to be influenced by ionizations of the conserved active site residues that act

as general acid-base catalysts.[74,75] The mutation of a potential acid-base catalytic residue should result in complete elimination of the ionization associated with that particular residue, and should be reflected in the pH-rate profile of the mutant enzyme when compared with the native enzyme. We, therefore, selected the FGD E109Q and H40A variants for pH-rate studies because of the potential roles of Glu109 and His40 as general acid-base catalysts for the FGD reaction. The p*K* values obtained from log k_{cat}-pH profiles represent ionizations in the enzyme-substrate complex, when enzyme is fully saturated with substrate.

The wild-type FGD log k_{cat}-pH profile decreased at high and low pH, in a manner characteristic of a general acid-base catalyzed reaction (Figure 2.4A). The two p*K* values obtained from the log k_{cat}-pH profile are consistent with the presence of an enzyme-substrate complex in which one ionizable residue must be deprotonated with a p*K* of 6.5 and another ionizable residue must be protonated with a p*K* of 8.0 in order for catalytic turnover to occur (Table 2.4). The FGD E109Q log k_{cat}-pH profile was sigmoidal with a plateau between pH 6-7 and a linear increase in k_{cat} between pH 8-9 (Figure 2.4C). The pK_1 of the log k_{cat}-pH profile was more acidic while the pK_2 is similar compared to that of wild-type FGD (Table 2.4). FGD H40A k_{cat} varied with pH according to a single acidic p*K* due to a complete elimination of the high-pH ionization seen in the corresponding wild-type FGD pH profile (Figure 2.4E).

The results of the log k_{cat}-pH profiles suggest that both His40 and Glu109 are protonated during catalysis and therefore, could both serve as active site acids. However, the distance between the pyrrole-like nitrogen of His40 and N1 of F_{420} is 5.4 Å, making the proton transfer between His40 and F_{420} unlikely (Figure 2.7). The more favorable donor-acceptor distance of 3.4 Å between N1 of F_{420} and 5-OH of Glu109 allows for the assignment of Glu109 as the active site acid that protonates the F_{420} cofactor at N1 during

the reaction (Figure 2.7). The pK values obtained from log k_{cat}/K_m-pH profiles represent ionizations in the free enzyme and substrate. The FGD E109Q k_{cat}/K_m-pH profile revealed two distinguishable ionization events with a pH-independence between pH 7-8 (Figure 2.4D; Table 2.4). The average pK value obtained from the bell-shaped log k_{cat}/K_m-pH profile for the wild-type and H40A constructs implies that there are two ionization events with pK_1 and pK_2 averaging to pK 7.0 (Figures 2.4B and 2.4F; Table 2.4). The phosphate moiety of G6P substrate ionizes at pK 6.1,[76] and assignment of a pK_1 6.1 to G6P ionization implies that another ionization event occurs at pK_2 7.9. It is possible to assign the basic pK_2 values of the log k_{cat}/K_m-pH profiles to residues in the free enzyme that are involved in binding the phosphate moiety of G6P,[74] such as Lys198 and Lys259.[50]

The K_m of the F_{420} cofactor at pH extremes was determined for wild-type FGD, FGD H40A and FGD E109Q so as to verify that the pH-dependence of the kinetic parameters was entirely as a result of effects on the G6P substrate. The F_{420} K_m values at pH 5.0 and 9.0 were similar for the wild-type FGD and FGD H40A, thus showing that the bell-shaped curves (Figure 2.4B and 2.4F) were not as a result of higher F_{420} K_m at the pH extremes. The FGD E109Q variant had similar $K_{0.5}$ values at pH 7.0-9.0 while the K_m at pH 5.0 was ~5-fold lower compared to the $K_{0.5}$. Therefore, it is also evident that the FGD E109Q bell-shaped curve (Figure 2.4D) was not as a result of lower F_{420} affinity at pH extremes.

Unlike the wild-type enzyme and the FGD H40A mutant, the FGD E109Q variant displayed sigmoidal kinetics with respect to the F_{420} cofactor at pH 7.0-9.0, thus suggesting the possibility of an allosteric mechanism for this mutant (Figure 2.5). The values of the Hill coefficient varied from 1.8-3.6, suggesting strong positive cooperativity with respect to the F_{420} cofactor. However, in order for an allosteric mechanism to truly exist, both the ligand binding curve and the kinetic curve must exhibit sigmoidal behavior.[77-

[79] The FGD E109Q F_{420} binding curves were all hyperbolic at pH 7.0-9.0. This lack of thermodynamic cooperativity in the FGD E109Q F_{420} binding curves strongly suggests that the pH-dependent sigmoidal F_{420} kinetic curves are as a result of kinetic cooperativity.[77,80]

Random addition of substrates and enzyme hysteresis are two mechanisms that can be used to explain kinetic cooperativity.[77,81,82] For a two-substrate oligomeric enzyme that follows a random substrate addition mechanism, the positive kinetic cooperativity curves due to one substrate will depend on the concentration of the other substrate, and saturating concentrations of the other substrate will result in substrate inhibition.[80,83] FGD E109Q G6P kinetic curves did not display substrate inhibition at saturating G6P concentrations (data not shown) and we can therefore eliminate random substrate addition mechanism as an explanation for the observed kinetic cooperativity. It is plausible that the pH-dependent kinetic cooperativity for FGD E109Q is due to enzyme hysteresis as a result of F_{420}-induced isomerization from a less active to a more active form of the enzyme.[81,84] The pH-profile studies presented here have established that the Glu109 residue protonates the F_{420} cofactor at position N1. Therefore, it is likely that in the absence of the Glu109 residue, the FGD E109Q variant will undergo conformational changes with increasing concentrations of F_{420} before it is able to attain it's most active form.

The pre-steady state kinetics experiments conducted in diode array mode produced scans between 350-800 nm, revealing no observable intermediate peaks within that wavelength range. The catalytically inefficient FGD variants, W44A and H40A, displayed only a slow phase under multiple turnover conditions. However, the FGD multiple turnover plots revealed two phases for FGD wild-type, W44F, W44Y, and E109Q (Figure 2.6). Similar biphasic kinetics have previously been observed in another F_{420}-dependent enzyme known as $F_{420}H_2$:$NADP^+$ oxidoreductase.[2] The fast phase k_{obs} values for the mentioned four FGD constructs were very similar to their k_{obs} values under single turnover

conditions (Table 2.5), while the k_{obs} values for the slow phase were very similar to the steady state k_{cat} values (Tables 2.4 and 2.5). Since the fast phase observed reflects the hydride transfer step of the FGD reaction, it is reasonable to conclude that the rate-limiting step for the FGD reaction is not the hydride transfer.

In summary, the drastic loss of catalytic efficiency and k_{cat} for the FGD H40A mutant suggests that His40 plays a crucial role in the FGD reaction. However, based upon the pH profiles, it is likely not the general base as was previously proposed. Based upon the rate-pH profiles, we have also shown that Glu109 is the general acid involved in the last step of the FGD reaction, where it donates a proton to N1 of the F_{420} cofactor. We have also deduced that aromaticity at residue 44 is essential for catalysis, and that Trp44 residue is not likely involved in acid-base catalysis of the FGD reaction.

Chapter 3

MECHANISTIC INSIGHTS INTO F_{420}-DEPENDENT GLUCOSE-6-PHOSPHATE DEHYDROGENASE USING ISOTOPE EFFECTS AND SUBSTRATE INHIBITION STUDIES

3.1 Introduction

F_{420}-dependent glucose-6-phosphate dehydrogenase (FGD) is an essential pentose-phosphate pathway enzyme that catalyzes the conversion of glucose-6-phosphate (G6P) to 6-phosphogluconolactone within mycobacteria.[45] The enzyme utilizes G6P to transfer a hydride to the C5 position on the *si*-face of the oxidized cofactor, producing reduced F_{420} within the cell. Recent studies by Jirapanjawat *et. al.* have shown that the reduced F_{420} cofactor is essential for protecting mycobacteria from diverse environmental antimicrobial agents.[34] More specifically, FGD appears to be the only enzyme within mycobacteria that produces the reduced F_{420} cofactor[34] and is therefore essential for the survival of the bacteria within the environment and also aids in the resistance of *Mycobacterium tuberculosis* (*M. tuberculosis*).[34]

The crystal structure confirms that FGD is a 78 kDa homodimer with one F_{420} molecule per subunit.[50] The proposed FGD reaction mechanism based on this crystal structure suggested that His40 acts as an active site base, while Glu109 donates a proton to the F_{420} cofactor, and Trp44 aids in stabilizing reaction intermediates.[50] However, there was no experimental evidence to support the FGD proposed mechanism. In our previous investigation of the FGD mechanism, we converted His40 to alanine (H40A), in order to discern if it is the active site base. We also converted Glu109 to glutamine (E109Q) to investigate whether it was the active site acid, and converted Trp44 to alanine (W44A), phenylalanine (W44F), and tyrosine (W44Y) to study its functionality.[72] Binding studies on the FGD variants suggested that these residues do not function in G6P binding, but that

they do play a role in F_{420} cofactor binding. However, they did play a role in F_{420} cofactor binding. Additionally, our steady state kinetic analysis of these variants suggests that the aromaticity of Trp44 is essential for FGD activity and that His40 and Glu109 play important roles in catalysis.[72] Further analysis of the H40A and E109Q variants using pH profiles suggested that His40 does not serve as the active site base, while Glu109 is the active site acid.[72] While this work provided insights into the key residues involved in FGD catalysis, much of the mechanistic details of the reaction is yet to be investigated.

For example, studies using isotopic labeling are informative given the multistep nature of enzymatic reactions, and are therefore effective methods for determining enzymatic mechanisms. Isotopic substitution *via* a deuterium or another heavy atom could change the rate of a specific step in a mechanism. Such studies can also help to determine whether an enzymatic reaction is stepwise or concerted.[85,86] Additionally, solvent deuterium isotope studies can be useful in determining how many protons are in flight during turnover.

Studies of this kind have been performed with $NADP^+$-dependent glucose-6-phosphate dehydrogenase (G6PD) in which d-1-glucose-6-phosphate and ^{13}C labeled G6P at the C-1 position were used to determine the magnitude of the isotope effect within the enzyme.[87] Steady state experiments were conducted with these substrates and with the natural unlabeled G6P substrate. The data showed an increase in the apparent V/K values with the deuterated substrate, which was characteristic of a mechanism in which all isotope effects are attributed to the same step of a reaction.[87] The isotopically labeled substrate experiments showed an isotope effect of $^{D}k = 5.27 \pm 0.29$, while in D_2O the number reduced to 3.66 ± 0.29. The data suggest that there is a coupled motion effect when more than one hydrogen is in motion in the transition state.[87] Such studies have not previously been conducted with FGD nor any other F_{420} dependent enzyme. Therefore,

the goal of this study is to use isotopic substitution to observe the isotope effect on the hydride transfer step using steady state and pre-steady state kinetic methods. We have also performed solvent isotope effects experiments using D_2O in order to determine the number and possible origin of protons in flight during turnover. Finally, since previous steady state kinetics could not deduce the order of substrate addition,[72] an additional goal of this work is to use dead-end inhibition studies and steady state kinetics to determine the order of addition for G6P and the F_{420} cofactor.

3.2 Materials and methods

3.2.1 Reagents

G6P was purchased from USB Corporation, unless otherwise specified. The F_{420} cofactor with a tail length of 6-9 γ-glutamate residues was prepared as previously described.[15] Activated carbon, ATP disodium salt (98%), sodium citrate, magnesium chloride and Tris buffer were purchased from Fisher Scientific. D_2O, deuterium chloride, D-Glucose and D-glucose-1-d_1 (98 atom % D) were purchased from Sigma Aldrich. Hexokinase was purchased from Worthington Biochemical Corporation. The glucose-6-phosphate assay kit was purchased from ScienCell Research Laboratories.

3.2.2 FGD expression and purification

The wild-type FGD enzyme used for all experiments presented in this chapter was expressed and purified as described in Chapter 2, Section 2.2.3.

3.2.3 Dead-end inhibition studies using citrate

The wild-type FGD steady state kinetics experiments were performed using a Cary 100 UV-Visible spectrophotometer in a Starna Cells Spectrosil® Quartz sub-micro cell (160 µl nominal volume). Citrate was chosen as the inhibitor for the dead-end inhibition

studies.[50] The experiments were conducted at 22 °C in 50 mM Tris-HCl, pH 7.0 buffer containing 0, 2, 4, 8, or 10 mM sodium citrate. The wild-type FGD steady state kinetics experiments performed in 0 mM citrate have previously been published elsewhere.[72] The inhibition pattern with respect to G6P concentration was determined at the various citrate concentrations using a constant F_{420} concentration of 20 μM while varying the G6P concentrations (8 – 250 μM). The inhibition pattern with respect to F_{420} concentration was determined at the various citrate concentrations using a constant G6P concentration of 2 mM while varying the F_{420} concentrations (1 – 10 μM). Each reaction was initiated by adding wild-type FGD to a final concentration of 25 nM and the reduction of the F_{420} cofactor was followed at 420 nm.

For a visual inspection of the inhibition patterns, plots of 1/k *vs* 1/[S] were fitted to a double reciprocal function (Equation 3.1) using SigmaPlot (Systat Software, Inc., San Jose, CA, USA) version 13.0.

$$1/k = (K_m/(k_{cat}[S])) + 1/k_{cat} \qquad \text{Equation 3.1}$$

where, k is the rate constant obtained by dividing the initial rate by the enzyme concentration, k_{cat} is the turnover number, K_m is the Michaelis-Menten constant, and [S] is concentration of either G6P or F_{420}. Multidimensional fits of *k vs* [S] were also performed for the G6P and F_{420} inhibition curves using SigmaPlot version 13.0 Enzyme Kinetics Module (Systat Software, Inc., San Jose, CA, USA). The G6P inhibition data fit best to the competetive inhibition model (Equation 3.2) while the F_{420} inhibition data fit best to the uncompetetive inhibition model (Equation 3.3).

$$k = k_{cat}/(1 + (K_m/[S]) * (1 + I/K_i)) \qquad \text{Equation 3.2}$$

$$k = k_{cat}/(1 + I/K_i + K_m/[S]) \qquad \text{Equation 3.3}$$

3.2.4 Solvent deuterium isotope effects studies

3.2.4.1 Steady state kinetics experiments

The effects of solvent on the steady state kinetics parameters of wild-type FGD were investigated by performing the experiments at 22 °C, in 50 mM Tris (pH 7.0) dissolved in H_2O or 50 mM Tris (pD 7.0) dissolved in 100 % D_2O. The experiments performed in H_2O have previously been published elsewhere.[72] The D_2O buffer was prepared by deuterium chloride titration of the 50 mM Tris solution to pH 6.6, using the correction pD = pH + 0.4.[88,89] The kinetic parameters with respect to G6P were determined using a constant F_{420} concentration of 20 μM and varying G6P concentrations from 0.008 - 2 mM, while the kinetic parameters with respect to the F_{420} cofactor were determined using a constant G6P concentration of 2 mM and varying F_{420} concentrations from 1 – 10 μM. Each reaction was initiated by adding wild-type FGD to a final concentration of 25 nM and 420 nm wavelength was used to monitor the reduction of the F_{420} cofactor. Plots of rate constant *vs* substrate concentration were fitted to a hyperbolic function (Equation 3.4) using SigmaPlot (Systat Software, Inc., San Jose, CA, USA) version 13.0.

$$k = k_{cat}[S]/(K_m+[S]) \qquad \text{Equation 3.4}$$

where, k is the rate constant obtained by dividing the initial rate by the enzyme concentration, k_{cat} is the turnover number, K_m is the Michaelis-Menten constant, and [S] is concentration of either G6P or F_{420}. For each varied substrate, the solvent kinetic isotope effect (SKIE) was obtained by dividing the k_{cat} with respect to H_2O by the k_{cat} with respect to D_2O.

3.2.4.2 Proton inventory studies

Proton inventory studies were conducted using pre-steady state kinetic experiments under single turnover conditions. The rapid kinetic experiments were

performed on a Hitech Scientific DX2 stopped-flow spectrophotometer at 22 °C in 50 mM Tris (pH 7.0) buffer dissolved in varying D_2O concentrations (0-100%). The 0% D_2O experiments were performed in 50 mM Tris (pH 7.0) buffer dissolved in H_2O, and have previously been published elsewhere.[72] The 20, 40, 60, and 80% D_2O buffers were obtained by mixing appropriate volumes of 50 mM Tris in H_2O (0% D_2O, pH 7.0) with 50 mM Tris in D_2O (100% D_2O, pD 7.0). To ensure that the pD for each prepared D_2O solution remained at pD 7.0, the pD was measured using a pH electrode with the correction pD = pH + 0.4.[88,89] For each buffer composition, a solution of 100 µM FGD was pre-incubated with 10 µM F_{420} and then mixed rapidly with an equal volume solution of 1 mM G6P solution. The final concentrations for the single turnover kinetics were 50 µM FGD, 5 µM F_{420}, and 500 µM G6P. The single turnover plots of absorbance at 420 nm *vs* time were fitted to Equation 3.5 using SigmaPlot (Systat Software, Inc., San Jose, CA, USA) version 13.0,

$$A = A_1 \cdot e^{-k_{obs} \cdot t} + c \qquad \text{Equation 3.5}$$

where A is the absorbance at time t, A_1 is the initial absorbance at time t = 0, k_{obs} is the apparent rate constant, t is the reaction time, and c is the absorbance at infinite time. A linear plot of the proton inventory was analyzed using the simplified version of the Gross-Butler equation (Equation 3.4)[90,91]

$$k_n/k_0 = (\Phi^T - 1)n + 1 \qquad \text{Equation 3.6}$$

where k_n is the apparent rate constant at a given D_2O concentration, k_0 is the apparent rate constant in H_2O, n is the mole fraction of D_2O and Φ^T is the fractionation factor of a proton in transition state.[91,92] Assuming the hydrogen bond in which this proton participates to be linear, the hydrogen bond length (HBL) between the two proton wells was then calculated using Equations 3.7 and 3.8, where Δx_{min} is the distance between two proton wells, 2 Å is the value of two covalent bond lengths, and Φ^T is the fractionation factor.[93-96]

$$HBL = \Delta x_{min} + 2\ \text{Å} \qquad \text{Equation 3.7}$$

$$\Delta x_{min} = 0.2220 + 1.1924(\Phi^T) - 1.3347(\Phi^T)^2 + 0.6080(\Phi^T)^3 \qquad \text{Equation 3.8}$$

3.2.5 Kinetic deuterium isotope effects studies

3.2.5.1 G6P and G6P-d_1 synthesis

The deuterated substrate G6P-d_1 was enzymatically synthesized following a previously published protocol.[87] The reaction contained 30 mM D-glucose-1-d_1, 50 mM ATP, 500 U hexokinase and 50 mM $MgCl_2$ in a total volume of 50 mL. The reaction proceeded overnight at 4 °C and the pH was maintained at pH 8.0 using 2 N KOH. The reaction was then terminated by removing the hexokinase via an Amicon PM Ultrafiltration unit (30 kDa MWCO). The filtrate containing the deuterated substrate was then further purified using 3 cycles of activated charcoal treatment to remove excess ATP and ADP, followed by a Na^+ Chelex-100 column treatment to remove the Mg^{2+} ions. The purified G6P-d_1 was then precipitated using rotary evaporation and ethanol addition. For fair comparison between the deuterated and protiated substrates, the G6P used for the kinetic isotope effect studies was also synthesized using the procedure above, except for the 30 mM D-glucose-1-d_1 being substituted for 30 mM D-glucose. The molar masses of the synthesized G6P and G6P-d_1 substrates were then confirmed using LC-MS IT-TOF. Both synthesized G6P and G6P-d_1 substrates were dissolved in filtered deionized water and the concentrations of the stocks determined using the ScienCell Research Laboratories G6P assay kit. The concentration used for the mass determination was 1 mM for each of the substrates. Data were acquired using the Shimadzu LC-MS-IT-TOF mass spectrometer (MS) and recorded in negative electrospray (ESI) mode at an ESI interface voltage of -3.7 kV. The LC direct injection elution program was run for 1 minute and the MS

chromatograms were recorded from 100 m/z. The data was analyzed using LCMS Solution Software (Shimadzu Corp., Kyoto, Japan) version 3.70.390.

3.2.5.2 G6P and G6P-d_1 steady state kinetics experiments

The steady state kinetic experiments were performed and analyzed as described in Section 3.2.4.1. All the reactions were performed at 22 °C in 50 mM Tris-HCl, pH 7.0 buffer. The kinetic parameters were only determined with respect to the synthesized substrates, using a constant F_{420} concentration of 20 µM and varying the G6P or G6P-d_1 concentrations from 0.008 – 0.4 mM. The final FGD concentration used in each reaction was 25 nM. The hyperbolic steady state kinetic plots of rate constant *vs* substrate concentration were fitted to Equation 3.4 using SigmaPlot (Systat Software, Inc., San Jose, CA, USA) version 13.0. The kinetic isotope effect (k_H/k_D) was obtained by dividing the k_{cat} with respect to G6P (k_H) by the k_{cat} with respect to G6P-d_1 (k_D).

3.2.5.3 G6P and G6P-d_1 pre-steady state kinetics experiments

The pre-steady state kinetic experiments were performed under single turnover conditions as detailed in Section 3.2.4.2. All the reactions were performed at 22 °C in 50 mM Tris-HCl, pH 7.0 buffer. 100 µM wild-type FGD was pre-incubated with 10 µM F_{420} in the reaction buffer and then mixed rapidly with an equal volume solution of 1 mM G6P or G6P-d_1 solution. The final concentrations in the single turnover reactions were 50 µM wild-type FGD, 5 µM F_{420}, and 500 µM G6P or G6P-d_1. The single turnover plots of absorbance at 420 nm *vs* time displayed exponential decay and were fitted to Equation 3.5 using SigmaPlot (Systat Software, Inc., San Jose, CA, USA) version 13.0. The kinetic isotope effect was obtained by dividing the k_{obs} with respect to G6P by the k_{obs} with respect to G6P-d_1.

3.3 Results

3.3.1 Dead-end inhibition studies using citrate

The Lineweaver-Burk plot of 1/*k vs* 1/[G6P] at a fixed concentration of F_{420} and various fixed concentrations of citrate reveals competitive inhibition with respect to G6P (Figure 3.1A). The multidimensional fit of the G6P data to the competitive inhibition model (Figure 3.1B) yielded a G6P K_m of 26 ± 2 µM and citrate K_i of 0.84 ± 0.05 µM.

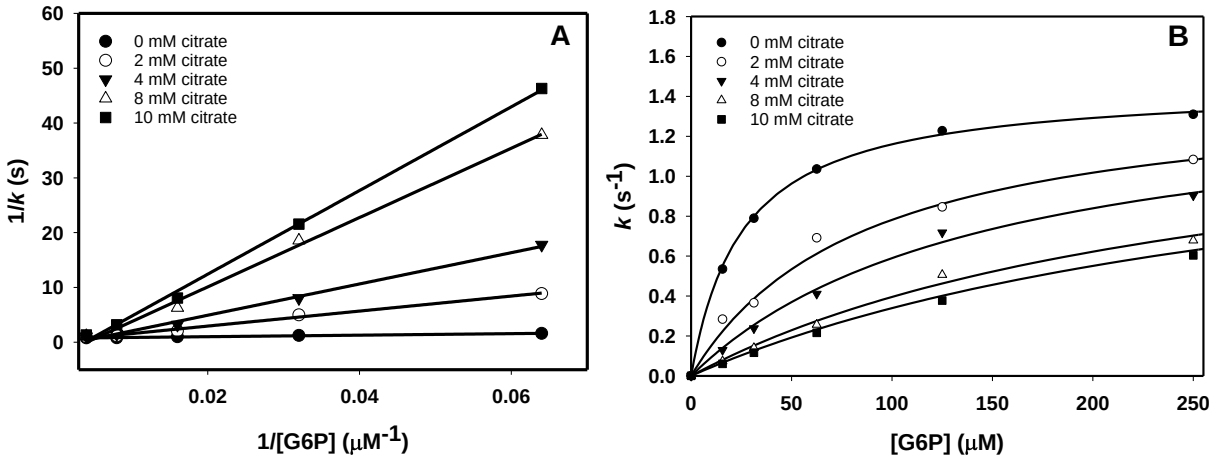

Figure 3.1 Inhibition pattern of wild-type FGD by citrate with G6P as the variable substrate. The steady state kinetics experiments were carried out in 50 mM Tris-HCl (pH 7.0) at 22 °C. The wild-type FGD and F_{420} concentrations were held constant at 25 nM and 20 µM respectively. The G6P and citrate concentrations were varied from 8 – 250 µM and 2 – 10 mM respectively. The rate constants were obtained by dividing initial rates by enzyme concentration. **A:** The double reciprocal plots of 1/*k vs* 1/[G6P]. The symbols represent an average of two measurements of rate constants at various concentrations of G6P and citrate. The solid lines represent the fits to Equation 3.1 at various citrate concentrations. **B:** Multidimensional fit of *k vs* [G6P] fitted to the competitive inhibition model. The symbols represent an average of two measurements of rate constants at various concentrations of G6P and citrate. The solid lines represent the fits to Equation 3.2 at various citrate concentrations.[97]

When the concentration of F_{420} was varied at various fixed citrate concentrations and a constant G6P concentration, the Lineweaver-Burk plot of 1/k *vs* 1/[F_{420}] revealed an

uncompetitive inhibition pattern of citrate with respect to F_{420} (Figure 3.2A). The multidimensional fit of the F_{420} data to the uncompetitive inhibition model (Figure 3.2B) yielded an F_{420} K_m of 0.89 ± 0.08 µM and citrate K_i of 7.3 ± 0.4 µM.

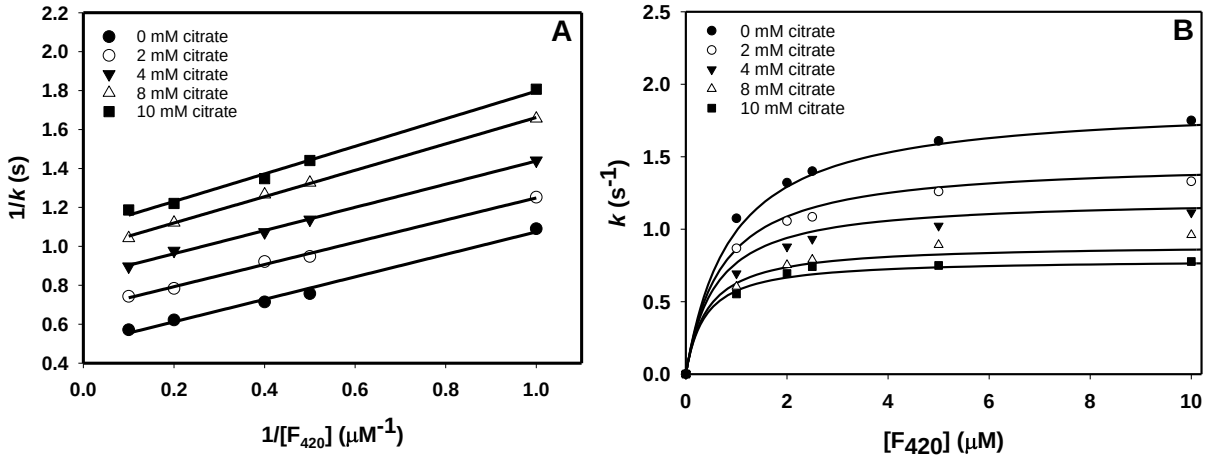

Figure 3.2 Inhibition pattern of wild-type FGD by citrate with F_{420} as the variable substrate. The steady state kinetics experiments were carried out in 50 mM Tris-HCl (pH 7.0) at 22 °C. The wild-type FGD and G6P concentrations were held constant at 25 nM and 2 mM respectively. The F_{420} and citrate concentrations were varied from 1 – 10 µM and 2 – 10 mM respectively. The rate constants were obtained by dividing initial rates by enzyme concentration. **A:** The double reciprocal plots of $1/k$ *vs* $1/[F_{420}]$. The symbols represent an average of two measurements of rate constants at various concentrations of F_{420} and citrate. The solid lines represent the fits to Equation 3.1 at various citrate concentrations. **B:** Multidimensional fit of k *vs* $[F_{420}]$ fitted to the uncompetitive inhibition model. The symbols represent an average of two measurements of rate constants at various concentrations of F_{420} and citrate. The solid lines represent the fits to Equation 3.3 at various citrate concentrations.[97]

3.3.2 Solvent deuterium isotope effects studies

3.3.2.1 Steady state kinetics

The magnitude of SKIE in the wild-type FGD reaction was determined by performing steady state kinetic experiments by varying the G6P or F_{420} concentration in reaction buffer containing either D_2O or H_2O. The hyperbolic steady state kinetics plots of

rate constant *vs* substrate concentration were fitted to Equation 2 to obtain the kinetic parameters. When G6P was the varied substrate (Figure 3.3A), the SKIE on the k_{cat} was 3.1 (Table 3.1). The SKIE on the k_{cat} when F_{420} was the varied substrate (Figure 3.3B) was 2.6, making it comparable to the G6P SKIE within error (Table 3.1). The SKIE on the k_{cat}/K_m was 4.6 and 2.6 with respect to G6P and F_{420} respectively (Table 3.1). The wild-type FGD steady state kinetics figures and parameters for experiments performed in H_2O are presented in Chapter 2, Section 2.3.3 (Figure 2.3 and Table 2.3).[72]

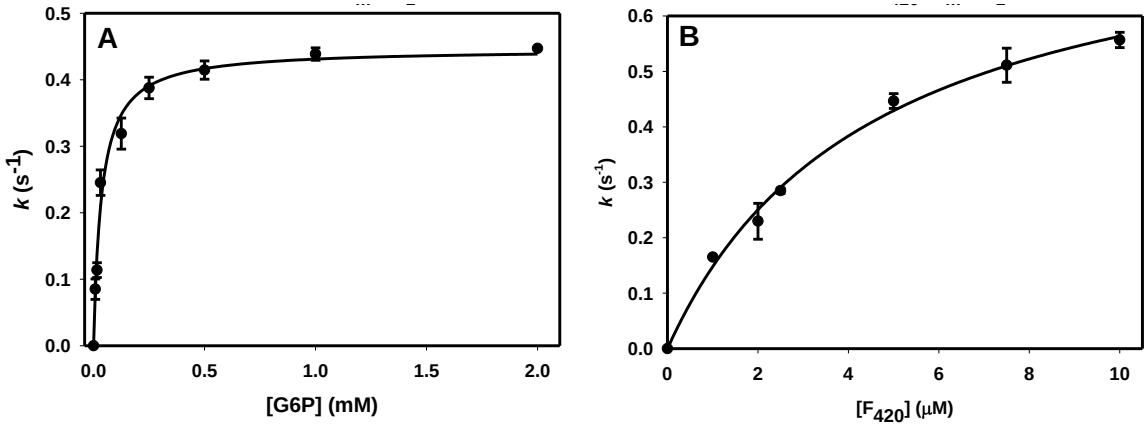

Figure 3.3 Wild-type FGD steady state kinetics plots for solvent isotope experiments. The reactions were carried out at 22 °C in 50 mM Tris-HCl dissolved in either D_2O (pD 7.0). The reduction of the F_{420} cofactor was tracked at 420 nm to obtain the initial rates of the reactions. The rate constants were obtained by dividing the initial rates by the FGD concentration. **A**: Plots of rate constant *vs* G6P concentration for D_2O. The solid circles represent an average of two values of rate constants at various concentrations of G6P and the solid line represents fit to Equation 3.4. **B**: Plot of rate constant *vs* F_{420} concentration for D_2O. The solid circles represent an average of two values of rate constants at various concentrations of F_{420} and the solid line represents fit to Equation 3.4. The error bars represent standard deviations from duplicate reactions of each varied substrate concentration.[97]

Table 3.1 Wild-type FGD solvent isotope effects on apparent steady state kinetics parameters. The reactions were carried out at 22 °C in 50 mM Tris-HCl dissolved in either D_2O (pD 7.0) or H_2O (pH 7.0). The reactions were monitored by following the reduction of the F_{420} cofactor at 420 nm. The steady state kinetic parameters k_{cat} and K_m were obtained by fitting the kinetic data to Equation 3.4. The uncertainty in each kinetic parameter is the standard error from least-squares fits of the kinetic data to the appropriate equation.[97]

[a]The apparent kinetic parameters presented here are reasonable approximations of the true values.

[b]The uncertainties for the catalytic efficiency values were calculated using the formula $\{((K_{m\,(err)}/K_m)^2 + (k_{cat\,(err)}/k_{cat})^2)^{1/2} * (k_{cat}/K_m)\}$, where $K_{m\,(err)}$ and $k_{cat\,(err)}$ represent the uncertainties in the individual K_m and k_{cat} values.

[c]Not determined.

	$^{G6P}k_{cat\,(app)}$[a] (s^{-1})	$^{F420}k_{cat\,(app)}$[a] (s^{-1})	$^{G6P}K_{m\,(app)}$[a] (μM)	$^{F420}K_{m\,(app)}$[a] (μM)	$^{G6P}k_{cat}/K_m$[b] ($M^{-1}s^{-1}$)	$^{F420}k_{cat}/K_m$[b] ($M^{-1}s^{-1}$)
H_2O	1.4 ± 0.1	1.4 ± 0.3	22 ± 2	2.6 ± 0.3	(6.0 ± 0.5) x 10^4	(6.0 ± 1.0) x 10^5
D_2O	0.45 ± 0.01	0.54 ± 0.02	36 ± 5	2.4 ± 0.2	(1.3 ± 0.5) x 10^4	(2.3 ± 0.2) x 10^5
^{D_2O}KIE	3.1 ± 0.2	2.6± 0.6	ND[c]	ND[c]	4.6 ± 2.0	2.6 ± 0.5

3.3.2.2 Proton inventory studies

Rapid mixing experiments under single turnover conditions were performed to obtain proton inventory data. The wild-type FGD k_{obs} value in H_2O (0% D_2O) are presented in Chapter 2, Section 2.3.5, Table 2.5.[72] The single exponential decay curves of absorbance at 420 nm *vs* time were fitted to Equation 3.5 to obtain the k_{obs} value at each concentration of D_2O (Table 3.2). Each of the k_{obs} values were divided by the k_{obs} value at 0% D_2O and plotted *vs* the mole fraction of D_2O and then fitted to Equation 3.6 to obtain the proton inventory parameters (Figure 3.4). The fractionation factor, Φ^T calculated from the proton inventory curve was 0.37, while the hydrogen bond length calculated from Equations 3.7 and 3.8 was 2.5 Å.

Table 3.2 Wild-type FGD stopped flow single turnover apparent rate constants at various concentrations of D_2O. The experiments were carried out in 50 mM Tris-HCl (pH 7.0) at 22 °C. The reactions were monitored by following the reduction of the F_{420} cofactor at 420 nm. The k_{obs} values were obtained by fitting the single turnover plots to Equation 3.5. The uncertainty in each kinetic parameter is the standard error from least-squares fits of the kinetic data to Equation 3.5.[97]

% D_2O	*n*	k_{obs} (s^{-1})	k_n/k_0
0	0	70 ± 5	1
20	0.2	62 ± 5	0.880
40	0.4	55 ± 4	0.779
60	0.6	42 ± 5	0.593
80	0.8	35 ± 3	0.506
100	1	27 ± 5	0.380

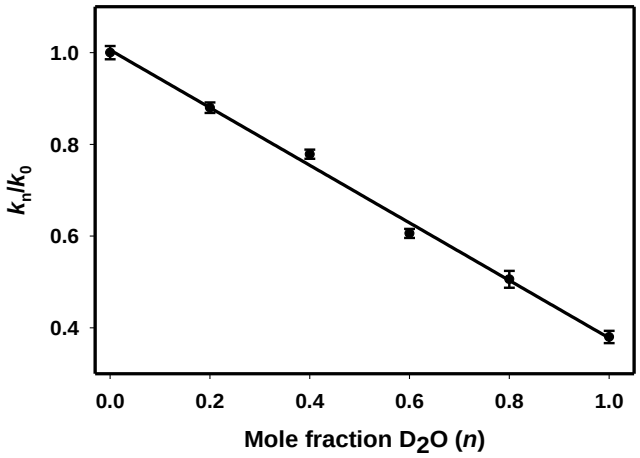

Figure 3.4 Proton inventory curve for wild-type FGD. The single turnover stopped-flow experiments were performed in diode array mode at 22 °C in 50 mM Tris-HCl, pH 7.0, dissolved in varying concentrations of D_2O. 50 µM wild-type FGD was pre-incubated with 5 µM F_{420} and then rapidly mixed with 500 µM G6P. The exponential decay curves for the reduction of the F_{420} cofactor at 420 nm were fitted to Equation 3.5 to yield the apparent rate constants (k_n) at varying D_2O concentrations. The k_n values were then divided by the apparent rate constant in pure H_2O (k_0). The k_n / k_0 ratios were then plotted *vs* the mole fractions of D_2O (*n*) and then fitted to Equation 3.6. The error bars in the plots represent standard deviations obtained from duplicate measurements of each variable substrate concentration.[97]

3.3.3 Kinetic deuterium isotope effects studies

3.3.3.1 G6P and G6P-d_1 molar masses

For the sake of proper comparison, both the protiated G6P and deuterated G6P-d_1 substrates were synthesized enzymatically following the same protocol. The molar masses of the synthesized G6P-d_1 and G6P were confirmed using the Shimadzu LC-MS-IT-TOF mass spectrometer and recorded in both positive and negative electrospray (ESI) mode. The negative ESI mode chromatograms revealed the predicted molar masses of 259.0225 g/mol and 260.0300 g/mol for the G6P (Figure 3.5A) and G6P-d_1 (Figure 3.5B), respectively.

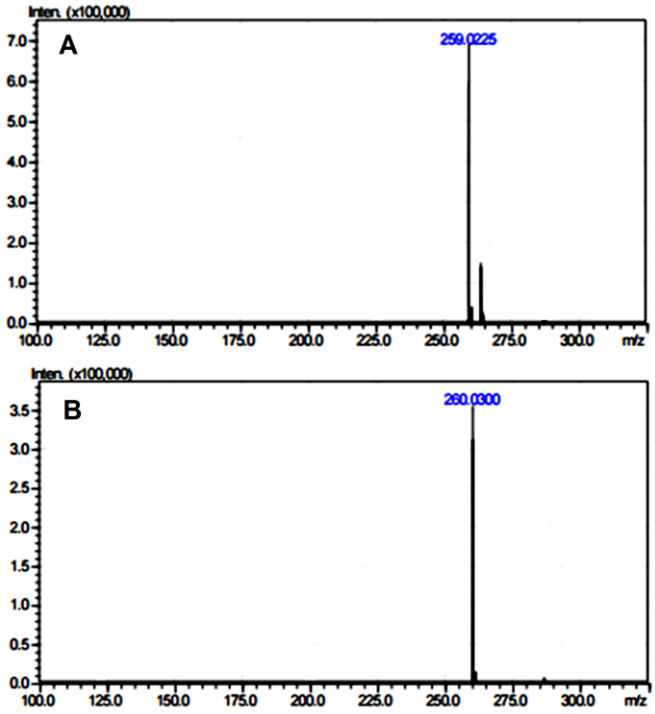

Figure 3.5 LC-MS-IT-TOF chromatograms of enzymatically synthesized substrates. Both chromatograms were recorded in the negative ESI mode. **A**: chromatogram for synthesized protiated G6P. **B**: chromatogram for synthesized deuterated G6P-d_1.[97]

3.3.3.2 G6P and G6P-d_1 steady state kinetics experiments

To determine the kinetic isotope effect on the wild-type FGD reaction, the steady state kinetic experiments were performed with a constant F_{420} concentration, while varying either the G6P or G6P-d_1 substrate concentration. The hyperbolic curves of the rate constant *vs* substrate concentration were fitted to Equation 3.4 to obtain the Michaelis-Menten kinetic parameters (Figure 3.6). The wild-type FGD K_m and k_{cat} values were very similar for the G6P and G6P-d_1 substrates, resulting in an overall kinetic isotope effect of 1.1 with respect to both k_{cat} and k_{cat}/K_m (Table 3.3).

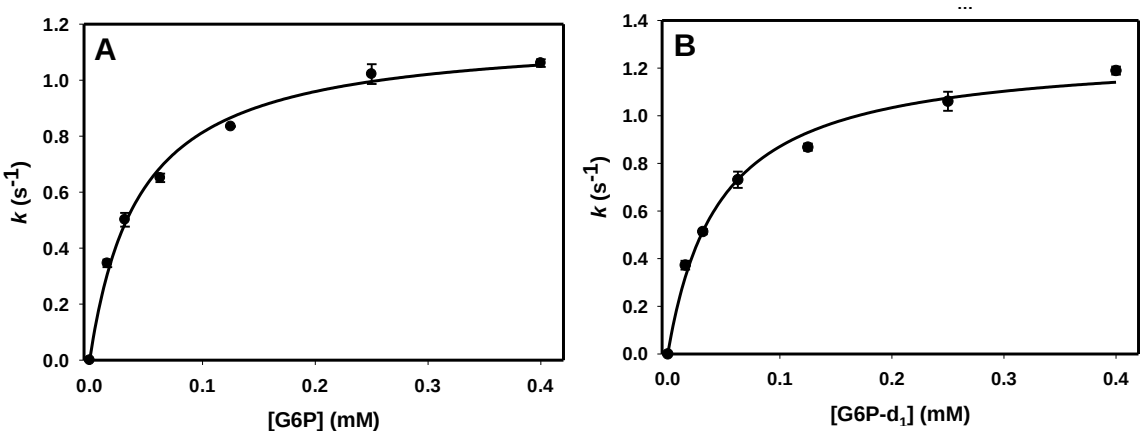

Figure 3.6 Wild-type FGD steady state kinetics plots with respect to enzymatically synthesized G6P and G6P-d_1 substrates. The reactions were carried out at 22 °C in 50 mM Tris-HCl (pH 7.0). The reduction of the F_{420} cofactor was followed at 420 nm to obtain the initial rates of the reactions. The rate constants were obtained by dividing the initial rates by the FGD concentration. **A**: Plot of rate constant *vs* G6P concentration. The solid circles represent an average of two values of rate constants at various concentrations of G6P and the solid line represents the fit to Equation 3.4. **B**: Plot of rate constant *vs* G6P-d_1 concentration. The solid circles represent an average of two values of rate constants at various concentrations of G6P-d_1 and the solid line represents the fit to Equation 3.4. The error bars represent standard deviations from duplicate reactions of each varied substrate concentration.[97]

Table 3.3 Wild-type FGD substrate deuterium isotope effects on steady state and pre-steady state kinetics parameters. The experiments were carried out in 50 mM Tris-HCl (pH 7.0) at 22 °C by varying the concentration of either G6P or G6P-d_1 substrates. The reactions were monitored by following the reduction of the F_{420} cofactor at 420 nm. The steady state and pre-steady state kinetic parameters were obtained by fitting the appropriate kinetic data to Equation 3.4 and Equation 3.5, respectively. The uncertainty in each kinetic parameter is the standard error from least-squares fits of the kinetic data to the appropriate equation.[97]

[a]The apparent kinetic parameters presented here are reasonable approximations of the true values.

[b]The uncertainties for the catalytic efficiency values were calculated using the formula $\{((K_{m\,(err)}/K_m)^2 + (k_{cat\,(err)}/k_{cat})^2)^{1/2} * (k_{cat}/K_m)\}$, where $K_{m\,(err)}$ and $k_{cat\,(err)}$ represent the uncertainties in the individual K_m and k_{cat} values.

	Steady state kinetics					**Pre-steady state kinetics**	
	$k_{cat\,(app)}$[a] (s^{-1})	$K_{m\,(app)}$[a] (μM)	k_{cat}/K_m[b] ($M^{-1}s^{-1}$)	k_H/k_D	$(k_{cat}/K_m)_H/(k_{cat}/K_m)_D$	k_{obs} (s^{-1})	k_H/k_D
G6P	1.40 ± 0.03	44 ± 4	(3.2 ± 0.1) x 10^4	1.1 ± 0.1	1.1 ± 0.1	78 ± 8	1.4 ± 0.1
G6P-d_1	1.30 ± 0.05	46 ± 6	(2.8 ± 0.2) x 10^4			56 ± 1	

3.3.3.3 G6P and G6P-d_1 pre-steady state kinetics experiments

The kinetic isotope effect on the FGD reaction was also investigated by performing rapid mixing experiments under single turnover conditions. The exponential decay curves of absorbance at 420 nm *vs* time were fitted to Equation 3.5 to obtain the k_{obs} values (Figure 3.7). A kinetic isotope effect of 1.4 was obtained by dividing the k_{obs} with respect to G6P by the k_{obs} with respect to G6P-d_1 (Table 3.3).

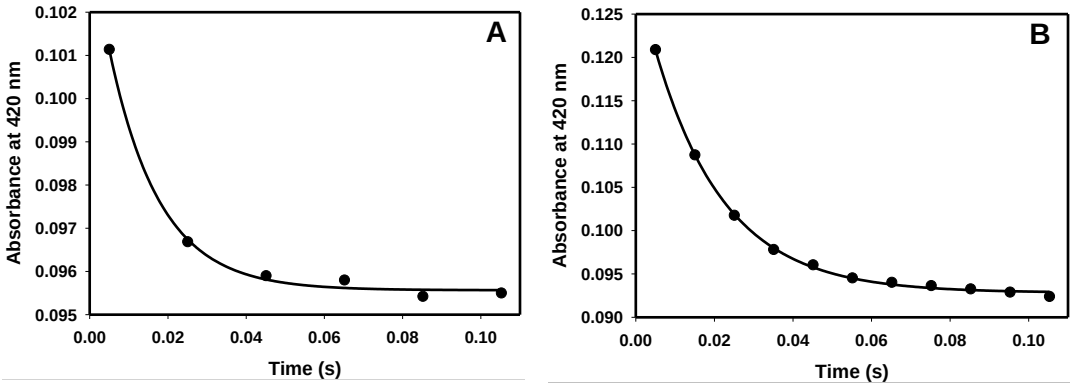

Figure 3.7 Wild-type FGD pre-steady kinetics plots of absorbance at 420 nm *vs* time with respect to enzymatically synthesized G6P and G6P-d_1 substrates. The single turnover experiments were carried out in diode array mode, using 50 mM Tris-HCl (pH 7.0) buffer at 22 °C. **A:** protiated substrate experiment containing 50 µM wild-type FGD, 5 µM F_{420} and 500 µM G6P. The solid circles represent an average of three absorbance values at various times and the solid line represents the fit to Equation 3.5. **B:** deuterated substrate experiment containing 50 µM wild-type FGD, 5 µM F_{420} and 500 µM G6P-d_1. The solid circles represent an average of three absorbance values at various times and the solid line represents the fit to Equation 3.5.[97]

3.4 Discussion

FGD is an enzyme that is essential for the survival of *M. tuberculosis* because it catalyzes the committed step of the pentose-phosphate pathway, which produces pentose phosphate sugars used for nucleotide synthesis within the bacteria. Additionally, FGD has been proven to be the only *M. tuberculosis* enzyme that produces reduced F_{420} cofactor, which is essential for the detoxifaction process within the bacterium.[34] While the *M. tuberculosis* FGD strictly uses the F_{420} cofactor for catalysis,[45] the human G6PD enzyme uses either NAD^+ or $NADP^+$.[62,66] Since *M. tuberculosis* causes TB by incubating within humans, the specificity of FGD for the F_{420} cofactor is a unique characteristic that can be further explored for therapeutic purposes without compromising the human G6PD. In order for FGD to be considered as a potential therapeutic target, it is important to understand the mode of action of this enzyme. However, there is still very little that is known about the

FGD reaction mechanism. The purpose of this present work is to provide further insight into the FGD reaction mechanism by deducing the order of substrate addition using dead-end inhibition studies. We also present deuterium solvent and kinetic isotope effects studies which are useful in determining the number of protons in flight during catalysis and can also be used to determine the rate-limiting step of an enzymatic reaction.

Dead-end inhibition studies with competitive inhibitors can be used to determine whether an enzymatic mechanism is random or ordered, and also to verify the order of substrate addition for enzymes that use two substrates.[98,99] In 1973, glucosamine-6-phosphate, a G6P substrate analog, was identified as a competetive inhibitor of G6PD from yeast and rat liver cells.[100] Since then, dead-end inhibition studies have been conducted to investigate the reaction mechanism of other G6PD enzymes using glucosamine-6-phosphate as the inhibitor.[101-103] However, due to the fact that FGD is unique in its use of the F_{420} cofactor, and because glucosamine-6-phosphate has only previously been shown to inhibit NAD^+ or $NADP^+$ dependent G6PD, we did not use glucosamine-6-phosphate in our studies.

The FGD crystal structure solved previously by the Baker group lead to the discovery that citrate is a competetive inhibitor of FGD with respect to the G6P substrate.[50] Therefore, the inhibition experiments presented here were performed in the presence of citrate, in an attempt to form an FGD:F_{420}:citrate dead-end complex. The inhibition patterns obtained from the dead-end inhibition experiments eliminate a rapid equilibrium random mechanism of substrate addition. In a random mechanism, citrate would be able to bind to both free FGD and the FGD:F_{420} complex, resulting in non-competitive and competitive inhibition with respect to F_{420} and G6P, respectively. However, citrate was found to be a competitive inhibitor with respect to G6P (Figure 3.1) and an uncompetetive inhibitor with respect to F_{420} (Figure 3.2), implying that citrate can only bind to the FGD:F_{420} complex.

This supports a mechanism of ordered addition of substrates, in which the F_{420} cofactor must bind to FGD first before G6P can bind.[98,101,104]

Product inhibition studies can also be utilized to investigate enzyme reaction mechanisms,[98] and such work has specifically been done before using NADPH for other G6PD enzymes.[101-103,105,106] In the case of FGD, we were unable to perform product inhibition studies with the $F_{420}H_2$ product because it is not as readily available as NADPH. We were also unable to perform product inhibition studies with 6-phosphogluconolactone product due its unstable nature in solution which gives it a very short half-life (~1.5 s).[107]

Steady- state kinetic experiments performed in Tris buffer dissolved in either D_2O or H_2O revealed the magnitudes of deuterium SKIE on the wild-type FGD k_{cat} and k_{cat}/K_m, with respect to both G6P and F_{420}. All experiments were performed at pH/pD 7.0 which was chosen based on previously published wild-type FGD pH profiles that revealed a pH independence of k_{cat} at pH 7.0.[72] Regardless of which substrate was varied, the SKIE observed for all four kinetic parameters were normal since all the values obtained were greater than 1 (Table 3.1). These SKIE values all fall within the range of 1.5-4, which is usually observed in general acid-base catalysis derived from a single transition state site such as a catalytic proton bridge.[108] Since a single proton transferred from an oxygen atom usually yields SKIE ≥1.5,[109] our SKIE results suggest that a proton transferred from an oxygen atom probably plays a significant role in the rate-limiting step of the FGD reaction.

Proton inventory experiments were performed using rapid mixing experiments under single turnover conditions, to further investigate the effect of solvent-derived protons and to determine the number of solvent protons in transition in the isotope-sensitive steps of the FGD reaction. The proton inventory curve fitted to Equation 3.6 was linear (Figure 3.4), suggesting that a single solvent-exchangeable proton was likely involved in the transition state and was responsible for the observed overall SKIE.[91,92,110] Fractionation

factors obtained from proton inventory curves are often used to characterize hydrogen bonds, where fractionation factors less than 1 are usually attributed to short and strong hydrogen bonds [111]. The fractionation factor, $\Phi^T = 0.37$ obtained from the proton inventory curve was significantly less than 1 and almost near the minimum Φ^T value of 0.16 [95,111], which is consistent with a proton on a carboxylic acid involved in a short and strong hydrogen bond [112,113]. We can, therefore, propose that this solvent-exchangeable proton is the proton on Glu109 that protonates the cofactor at position N1 [91,110]. The hydrogen bond length for the Glu109-COOH$\cdots$$F_{420}$-N1 interaction as calculated from the measured fractionation factor was 2.5 Å, which is much less than the typical van der Waals contact distance of 2.9 Å between nitrogen and oxygen, indicating short, strong hydrogen bond formation in the FGD mechanism which plausibly serves to increase the enzyme's catalytic efficiency.

Primary deuterium kinetic isotope effects on the FGD reaction were also investigated by using enzymatically synthesized deuterated and protiated G6P in both steady state and pre-steady state kinetic experiments. The G6P hydrogen atom targeted for deuterium substitution was the C1-H, which is the hydride that is transferred to the C5 position of the F_{420} cofactor during catalysis.[50] Small deuterium KIE values of 1.1 were observed with respect to both k_{cat} and k_{cat}/K_m (Table 3.3). Previous kinetic and mechanistic studies performed by our group showed that hydride transfer is likely not the rate-limiting step in the FGD reaction.[72] The results of our deuterium KIE experiments have provided further evidence that supports our previous findings of hydride transfer not being rate-limiting since there were no drastic effects on the reaction rates in both the steady state and pre-steady state kinetic parameters (Table 3.3). We can also conclude that the deuterium KIEs presented here are observed, rather than intrinsic, since the isotope-sensitive hydride transfer step is not rate-limiting.[114,115] It is plausible that the intrinsic

deuterium KIE is masked in the k_{cat} because the slower rate-limiting step occurs before or after the isotope-labeled hydride transfer step. Given the sizeable magnitude of the SKIE, it is likely that a proton transfer is involved in the rate-limiting step of the FGD reaction. This further implies that the rate-limiting step could be the first step of the FGD reaction where a base abstracts a proton form C1-OH of G6P, or the final step of the reaction where a proton is transferred from Glu109 to position N1 of the cofactor.

In 1982, the Cleland group utilized a combination of ^{13}C-labeling with deuterated and protiated G6P substrates in the investigation of the intrinsic KIE on *L. mesenteroides* G6PD which led to the conclusion that ^{13}C and deuterium isotope effects contribution at C1 of G6P occur concomitantly during the reaction.[87] In 1984, further studies on isotope effects by the Cleland group on *L. mesenteroides* G6PD provided evidence of tunneling in hydrogen motion, due to the first deuterium substitution decreasing the KIE of subsequent deuteration.[116] Based solely on the magnitudes of the deuterium KIE (Table 3.3), we cannot confidently deduce whether or not tunneling occurs within FGD since we were not able to measure the intrinsic KIE.

Figure 3.8 represents the proposed mechanism of FGD based upon the crystal structure solved by Bashiri *et. al.* as well as our previously published kinetic studies and our work presented here.[50,72] The oxidized F_{420} cofactor must first bind to the FGD active site, followed by G6P binding (Figure 3.8). We have not at this point been able to deduce the identity of the active site base. Therefore, it is represented as "B" in Figure 3.8. However, the base would then abstract a proton from G6P, facilitating the transfer of a hydride from the substrate to the oxidized F_{420}, thereby reducing it. F_{420} accepts a proton from Glu109 to complete its conversion to $F_{420}H_2$. Quite possibly, the active site base could be solvent.

In summary, this work provides further significant insights into the FGD reaction. We have presented the first evidence of ordered mechanism of substrate addition for FGD, where G6P can only bind to the FGD active site after the F_{420} cofactor has been bound. The solvent isotope effects studies also revealed a proton in flight that is likely from Glu109 and protonates the cofactor at position N1 in the last step of the FGD catalysis. Finally, the primary kinetic isotope effects studies yielded small KIE, implying that hydride transfer is not the rate-limiting step of the FGD reaction, and pointing towards a rate-limiting step that involves a proton transfer.

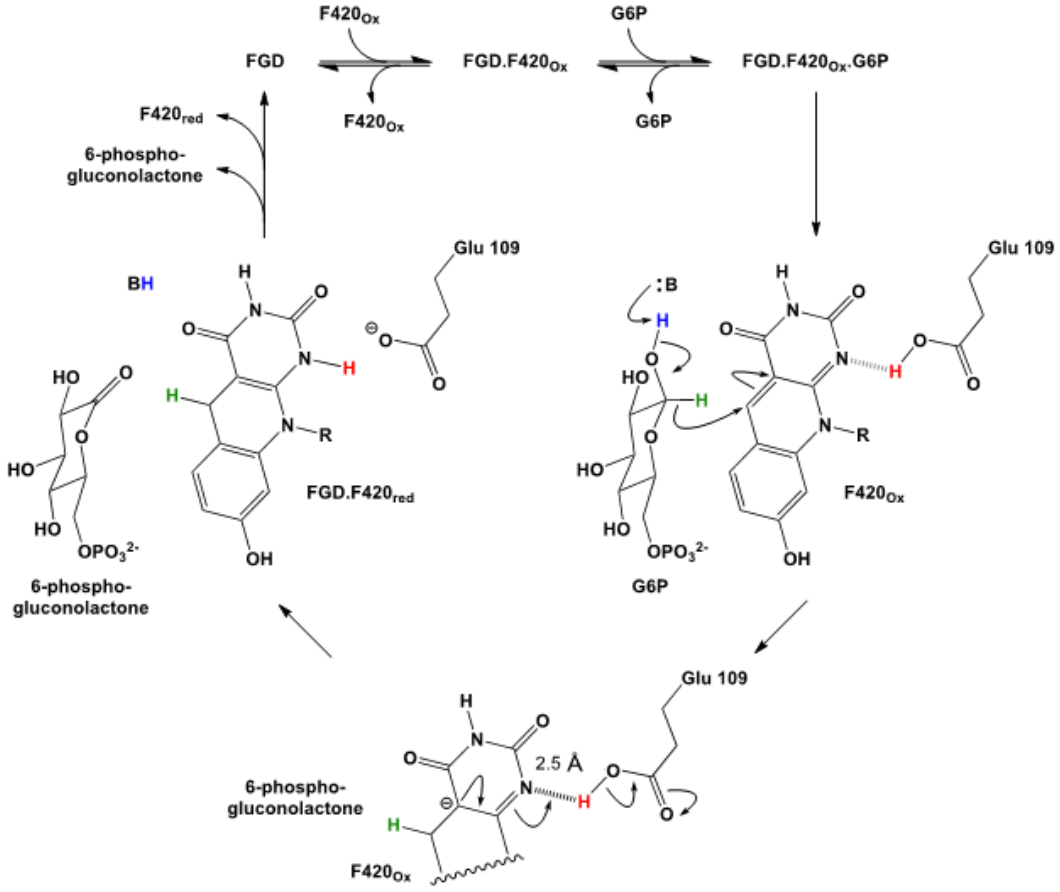

Figure 3.8 Revised FGD mechanism.[97]

Chapter 4

CRYSTAL STRUCTURE AND SUBSTRATE BINDING STUDIES OF THE H40A F_{420}-DEPENDENT GLUCOSE-6-PHOSPHATE DEYDROGENASE VARIANT FROM *MYCOBACTERIUM TUBERCULOSIS*

4.1 Introduction

The crystal structure of wild-type FGD from *M. tuberculosis* has previously been solved to 1.9 Å resolution by the Baker group.[50] However, this crystal structure was solved in the absence of the G6P substrate, since a turnover of the wild-type enzyme would not have captured the events that occur in the active site during catalysis. The crystal structure was instead solved in the presence of the F_{420} cofactor and citrate, which was found to be a competitive inhibitor of the enzyme. In this chapter, we aim to use the catalytically inactive FGD H40A variant to create an enzyme-substrate complex. The FGD H40A kinetic data has already been presented in Chapter 2 of this dissertation.[72] FGD H40A was targeted for crystallization because it's catalytic inactivity prevents it from turning over, and we can then deduce the amino acid residues that interact with the substrate during catalysis. Evidently, the FGD H40A crystals allowed us to trap a ternary structure in complex with G6P and F_{420}, displaying a snapshot of the initiation state of the reaction. Based on this structure, insightful information about the reaction mechanism of FGD is presented, paving the way for the chemical intervention of TB targeting FGD.

4.2 Materials and methods

4.2.1 Reagents

The cofactor F_{420} was prepared as previously described.[15] G6P was purchased from USB Corporation. Sodium chloride, β-mercaptoethanol (βME), imidazole and Tris buffer were purchased from Fisher Scientific.

4.2.2 Site-directed mutagenesis

Site-directed mutagenesis was used to create the FGD H40A mutant as detailed in Chapter 2, Section 2.2.2.

4.2.3 FGD expression and purification

Both wild-type FGD and the FGD H40A variant were expressed and purified following the protocol in Chapter 2, Section 2.2.3.

4.2.4 Binding of F_{420} and G6P to FGD

The fluorescence binding experiments for wild-type FGD and the FGD H40A variant were performed as described in Chapter 2, Section 2.2.4.

4.2.5 FGD steady state kinetics

The steady state kinetics experiments for wild-type FGD and the FGD H40A variant were performed as described in Chapter 2, Section 2.2.5.

4.2.6 FGD H40A crystallization

The FGD H40A crystals were grown and optimized in our laboratory at the University of Texas at Arlington as follows. The purified FGD H40A enzyme was concentrated to 14 mg/mL in 50 mM Tris-HCl, pH 7.0, using a 30 kDa cut-off Amicon filter unit (Millipore). In preparation for co-crystallization, the concentrated enzyme was incubated for 2 hours with 4.5 mM G6P and 41 µM F_{420}. Crystallization experiments were performed using the hanging drop vapor diffusion technique, with a 1:1 ratio of the reservoir solution to the protein solution, to a final drop volume of 4 µL. The best crystals were obtained using a precipitant containing 19% PEG 3350 and 0.1 M ammonium citrate dibasic (pH 5.0) that yielded crystals within 2 days. The crystals were fully grown after 1

week. Single crystals were cryoprotected in 30% glycerol containing 0.1 M ammonium citrate, and mounted on cryo loops and then flash-frozen in liquid nitrogen before shipping to the Synchrotron Radiation Laboratory for X-ray diffraction experiments.

4.2.7 X-ray diffraction, data collection and structure refinement

The X-ray diffraction, data collection and structure refinement presented in this section were performed by our collaborators at the University of Texas at Austin (Joshua Mayfield and Dr. Jessie Zang). Crystallographic diffraction data for FGD H40A/G6P were collected on beam-line 5.0.3 of the Advanced Light Source (ALS). All diffraction data were processed with HKL2000.[117] The structure was determined by molecular replacement (MR) using the existing FGD structure (PDB ID: 3c8n)[50] as a search model using the program Phaser in the PHENIX suite.[118] The MR solution was fitted into the calculated density in COOT[118] with computational refinements performed using phenix.refine in the PHENIX suite.[119] The ligands were manually built into the *F*o-*F*c map in COOT and then iteratively improved to obtain the final model. The quality of the final refined model was evaluated using Procheck and MolProbity.[120] The final statistics for data collection and structure determination are summarized in Table 4.1.

4.3 Results

4.3.1 Binding of F_{420} and G6P to FGD

The K_d values obtained for wild-type FGD and FGD H40A with respect to G6P and F_{420} binding are presented in Chapter 2, Section 2.3.2, Table 2.2. In summary, the G6P K_d values were similar for wild-type FGD and FGD H40A, while the F_{420} K_d value for FGD H40A was ~8 fold higher than for wild-type FGD.

4.3.2 FGD steady state kinetics

Both wild-type FGD and FGD H40A plots of rate constant vs G6P concentration displayed classic Michaelis-Menten saturation kinetics (Figure 2.3). The steady state kinetic parameters obtained for wild-type FGD and FGD H40A are presented in Chapter 2, Section 2.3.3, Table 2.3. In summary, the FGD H40A variant lost ~1000 fold catalytic activity.

4.3.3 FGD H40A structure and G6P binding

Data collection and processing statistics used to solve the FGD H40A structure are displayed in Table 4.1. The electron density maps for G6P and F_{420} bound in the active site are shown in Figure 4.1. The overall architecture of FGD aligns well with previous structures solved by the Baker group (PDB ID: 3c8n and 3b4y).[50]

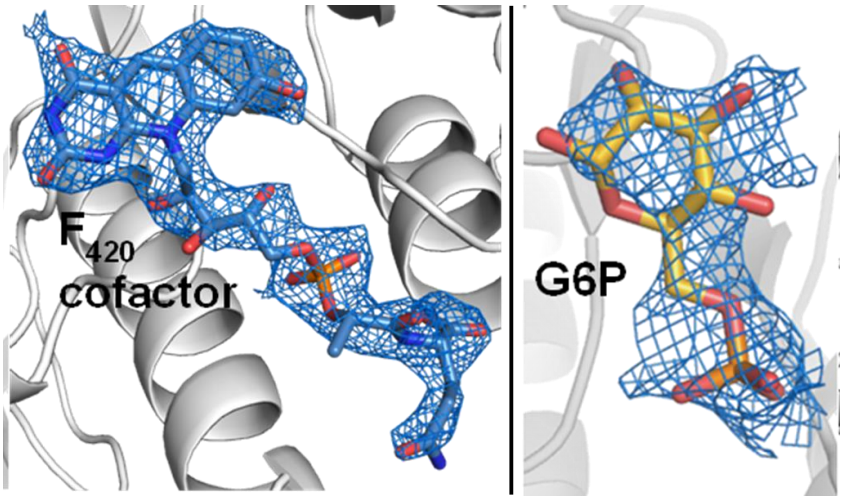

Figure 4.1 FGD H40A 2Fo-Fc electron density maps contoured to 1.0σ

Table 4.1 FGD H40A X-ray crystallography data collection and refinement statistics.

Wavelength (Å)	0.97648
Resolution range (Å)	49.04 - 2.893 (2.997 - 2.893)
Space group	P 21 21 21
Unit cell	a=89.522 Å, b=103.067 Å, c=159.556 Å, α=90°, β=90°, γ=90°
Total reflections	33566
Unique reflections	3220
Redundancy	7 (6)
Completeness	99.7 (97.0)
Mean I/sigma(I)	8.94 (1.99)
Wilson B-factor	41.61
R-sym (%)	23.2 (0.792)
R-work (%)	20.34 (24.40)
*R-free (%)**	26.96 (32.52)
Number of non-hydrogen atoms	10320
Protein residues	1328
RMS (bonds)	0.014
RMS (angles)	2.05
Ramachandran favored (%)	96
Ramachandran outliers (%)**	0.68
Average B-factor	33.1
**R-free is calculated with 5% of data randomly omitted from refinement*	
***Ramachandran statistics generated in MolProbity. Outliers arise from physiologically relevant non-proline cis-peptide bond & terminal residues.*	

The asymmetric unit contains four FGD molecules, each comprising residues 3-334. These residues assume an $(\alpha/\beta)_8$ TIM-barrel fold that encloses a deep active site pocket that binds the F_{420} cofactor and the G6P substrate (Figure 4.2A). The FGD H40A variant's active site aligns well with the existing structures and the mutation appears to minimally disturb the active site arrangement. The cofactor F_{420} is coordinated by a network of hydrogen bonds, as observed previously.[50] This network contains a notable non-proline *cis*-peptide bond between Ser73 and Val74 that orients the carbonyl group of the *cis*-peptide bond such that it contacts the central ring of the F_{420} deaza-isoalloxazine system (Figure 4.2B).[50]

Importantly, our structure provides the first experimental insight into the nature of G6P substrate binding. The hydroxyl groups of carbons 1-4 (C1-C4) in G6P are positioned *via* an extensive network of polar interactions with active site residues (Figure 4.2C). The C1 hydroxyl group hydrogen bonds with the side chain of Glu13, which is positioned by the hydroxyl of Ser38 and the indole nitrogen of Trp44. The C2 hydroxyl group accepts a hydrogen bond from the ε-amino group of Lys9, which in turn is held in place through additional hydrogen bonds with the carbonyl oxygen of Ser73 and the carboxyl group of Glu230.

The C3 hydroxyl group is hydrogen bonded to the side chains of Glu230 and Lys232, while the hydroxyl of C4 is also hydrogen bonded to the ε-amino group of Lys232. Recognition of the G6P phosphate group is mediated by a positively charged cluster of residues, Lys198, Lys259, and Arg283 (Figure 4.2D). Both Lys198 and Arg283 make direct electrostatic interactions with the phosphate moiety, while Lys259 interacts with the side chain of Thr195, which is in turn hydrogen bonded to one of the phosphate oxygens (Figure 4.2D). Atoms suspected to participate in hydride transfer, specifically the C1 of G6P and C5 of the F_{420} cofactor, are positioned ~4.5 Å apart in the FGD H40A structure.

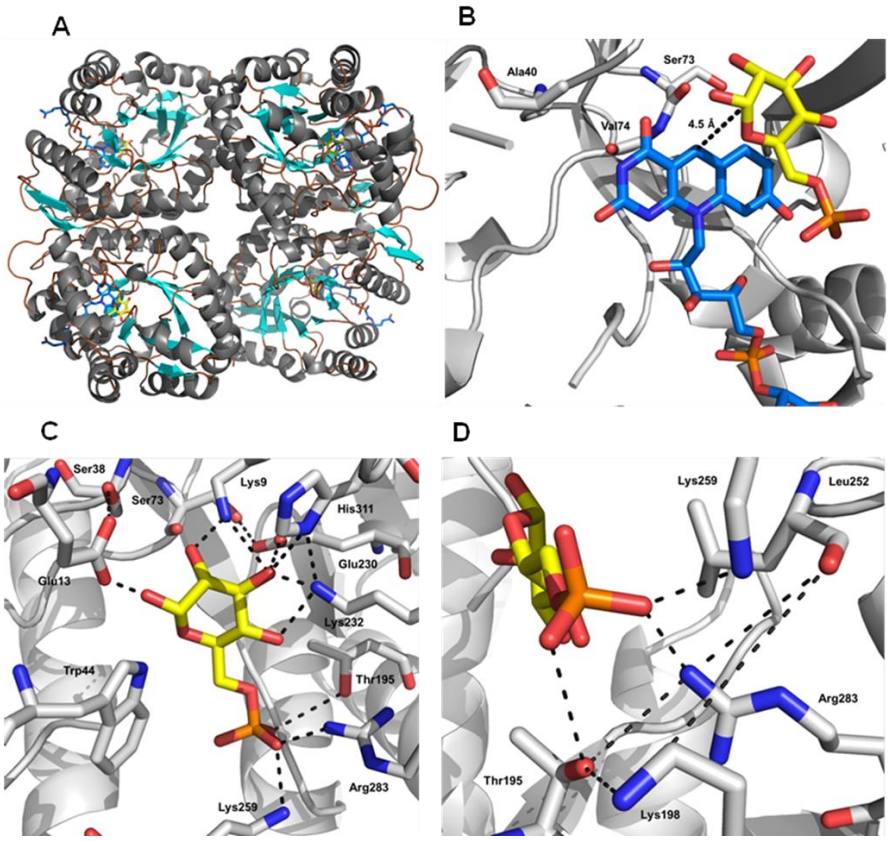

Figure 4.2 Structure of FGD H40A from *M. tuberculosis* in complex with F_{420} and G6P. **A**: Cartoon diagram of the FGD H40A tetramer displaying the $(\alpha/\beta)_8$ TIM-barrel fold, with α-helices (grey), β-strands (cyan), and loops (brown). The bound F_{420} cofactor (blue) and G6P (yellow) are also shown within each monomer. **B**: View of the active site showing the mutated Ala40 residue and the interaction between F_{420} and G6P. Residues Val72 and Ser73, which participate in the crucial non-proline *cis*-peptide bond, are also displayed. **C**: View of the active site showing the interaction of G6P with the protein. Residues Glu13, Lys9, His 311, Glu230, and Lys232 hydrogen bond to the hydroxyl groups of carbons 1-4. Glu13 further hydrogen bonds with Ser38, while Glu230 additionally hydrogen bonds to Ser73. Lys232 and His311 also hydrogen bond with each other. Trp44 does not form any hydrogen bonds with G6P or other residues. **D**: hydrogen bonding network around the phosphate moiety of G6P. Residues Thr195, Arg283, and Lys259 are essential for binding of the G6P phosphate moiety. The hydroxyl of Thr195 and carbonyl of Leu252 further coordinate the interactions by hydrogen bonding to the amino groups of Lys198 and Arg283. All figures were prepared using PyMOL version 1.3 (Schrodinger, LLC, New York, NY).

4.4 Discussion

The structure of FGD H40A bound to G6P reveals two primary determinants of substrate binding. First, the phosphate moiety of G6P interacts electrostatically with FGD at positively charged residues Lys198, Lys259, and Arg283. Secondly, polar contacts between FGD and the hydroxyl groups of C1-C4 on G6P are mediated by multiple residues; namely Lys9, Glu13, Glu230 and Lys232. Interestingly, these residues not only hydrogen bond directly with the G6P hydroxyl groups, thereby positioning G6P, but are also involved in an intricate network of interactions that include His311 and the unique non-proline *cis*-peptide bond between Ser73 and Val74. The carbonyl oxygen of this *cis*-peptide bond is within weak hydrogen bonding distance (~3.5 Å) of the ε-amino group of Lys9, which binds the C2 and C3 hydroxyl groups of G6P. This finding strengthens the importance of this conserved *cis*-peptide bond in FGD function.

In our structure, no obvious conformational change is observed at the active site upon H40A mutation, which is consistent with the nearly identical K_d values for G6P binding between the wild-type and H40A FGD. The decrease in affinity for F_{420} binding upon H40A mutation is not immediately apparent from the mutant structure. One possible explanation is the ability of the imidazole side chain of histidine to participate in polar contacts with the F_{420} cofactor. In a previous FGD structure (PDB ID: 3B4Y)[50] the imidazole ring of His40 is positioned ~3 Å from nitrogen 1 and carbonyl groups of the isoalloxazine ring system. Depending on the rotamer conformation and protonation state of this histidine side chain, hydrogen bonding may occur to stabilize the F_{420} cofactor within the active site.

Our investigation into the mechanism of the FGD reaction revealed that His40 is unlikely to be the active site base, and the particular role it plays in catalysis is not yet known.[72] Hydride transfer from C1 of G6P to C5 of F_{420} is theorized to follow the initial proton abstraction step. In our structure, C1 of G6P and C5 of F_{420} are separated by a

considerable distance (~4.5 Å), making hydride transfer in the observed conformation unlikely. It is probable that hydride transfer from C1 of G6P to the C5 of F_{420} occurs concomitantly with active site rearrangement to position these atoms within an appropriate distance for chemistry.

Appendix A

F_{420} and G6P binding curves for FGD H40A, E109Q, W44A, W44Y and W44F variants

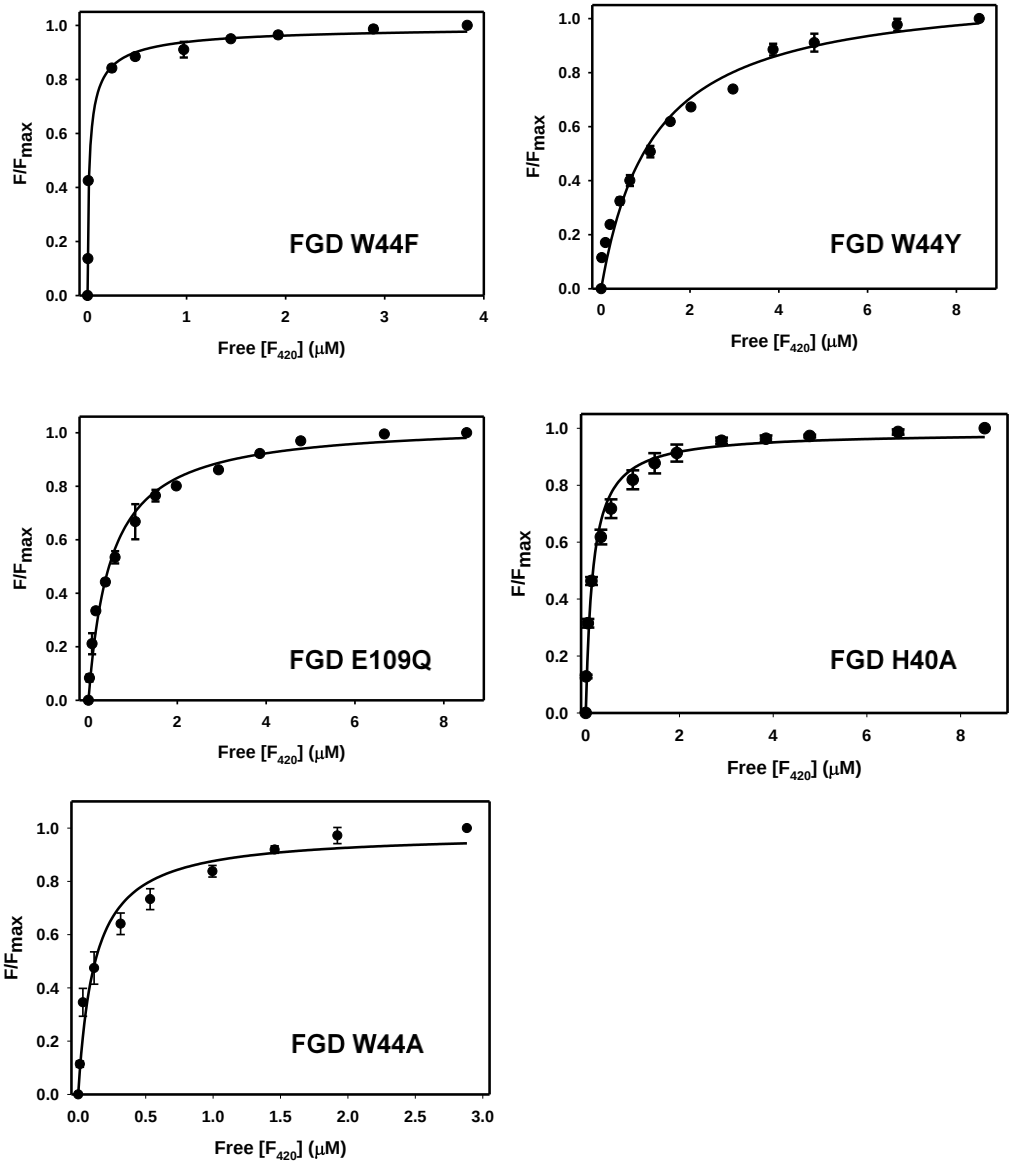

Figure A.1 Plots of F/F_{max} *vs* free F_{420} concentration for FGD variants. The assays for F_{420} binding to FGD were carried out at 22 °C in 50 mM Tris-HCl (pH 7.0). A 350 nM FGD solution was titrated with increasing concentrations of F_{420} and the samples were excited at 290 nm while the emission was monitored at 340 nm. The solid circles represent an average of two measurements of F/F_{max} at various concentrations of free F_{420} and the solid lines represent fit to Equation 2.1. The error bars in the plots represent standard deviations obtained from duplicate measurements of each F_{420} concentration.[72]

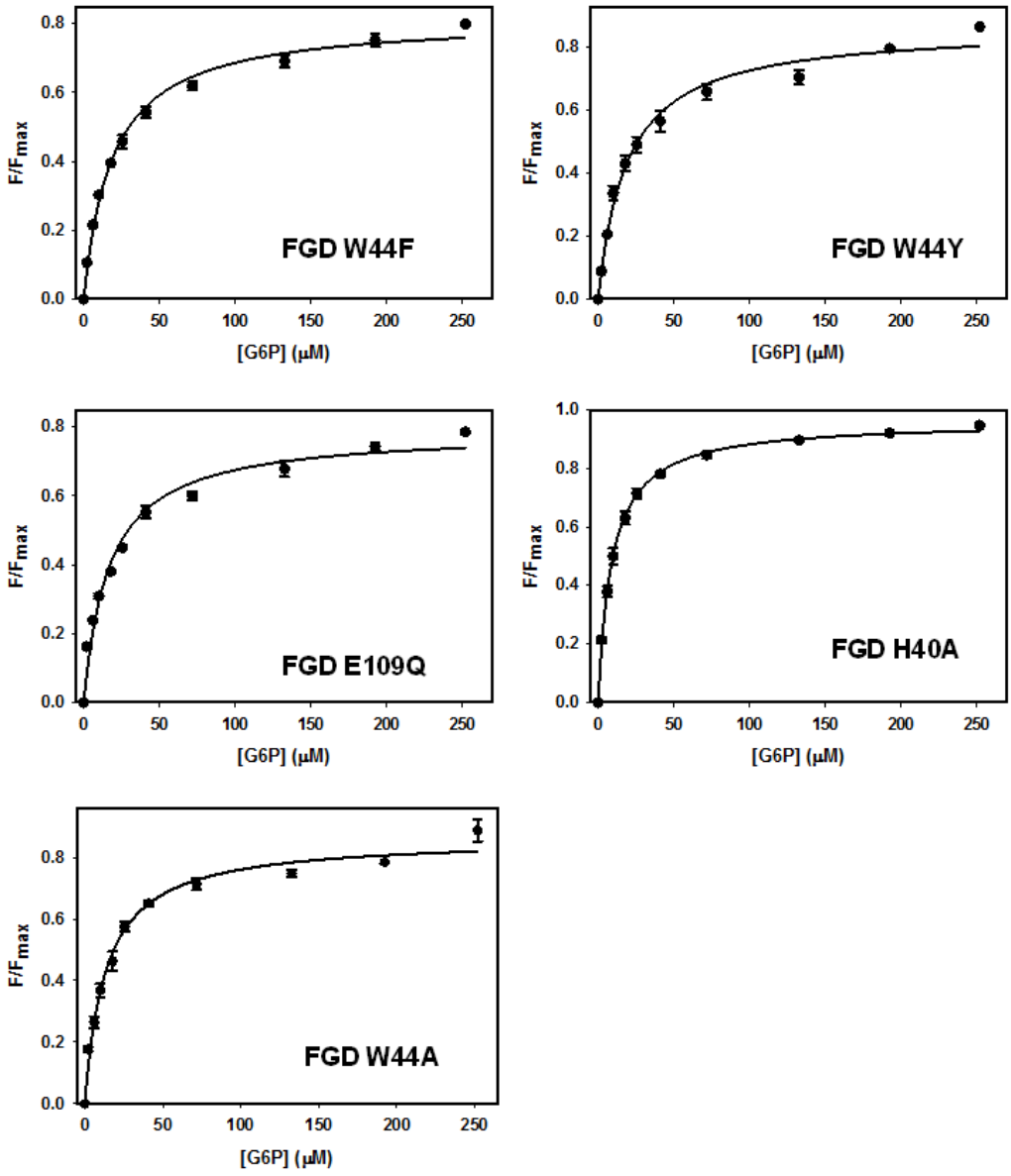

Figure A.2 Plots of F/F_{max} *vs* G6P concentration for FGD variants. The assays for G6P binding to FGD were carried out at 22 °C in 50 mM Tris-HCl (pH 7.0). A 350 nM FGD solution was titrated with increasing concentrations of G6P and the samples were excited at 290 nm while the emission was monitored at 340 nm. The solid circles represent an average of two measurements of F/F_{max} at various concentrations of G6P and the solid lines represent fit to Equation 2.2. The error bars in the plots represent standard deviations obtained from duplicate measurements of each G6P concentration.[72]

Appendix B

Steady state kinetics and pH dependence curves for FGD H40A, E109Q, W44A, W44Y and W44F variants

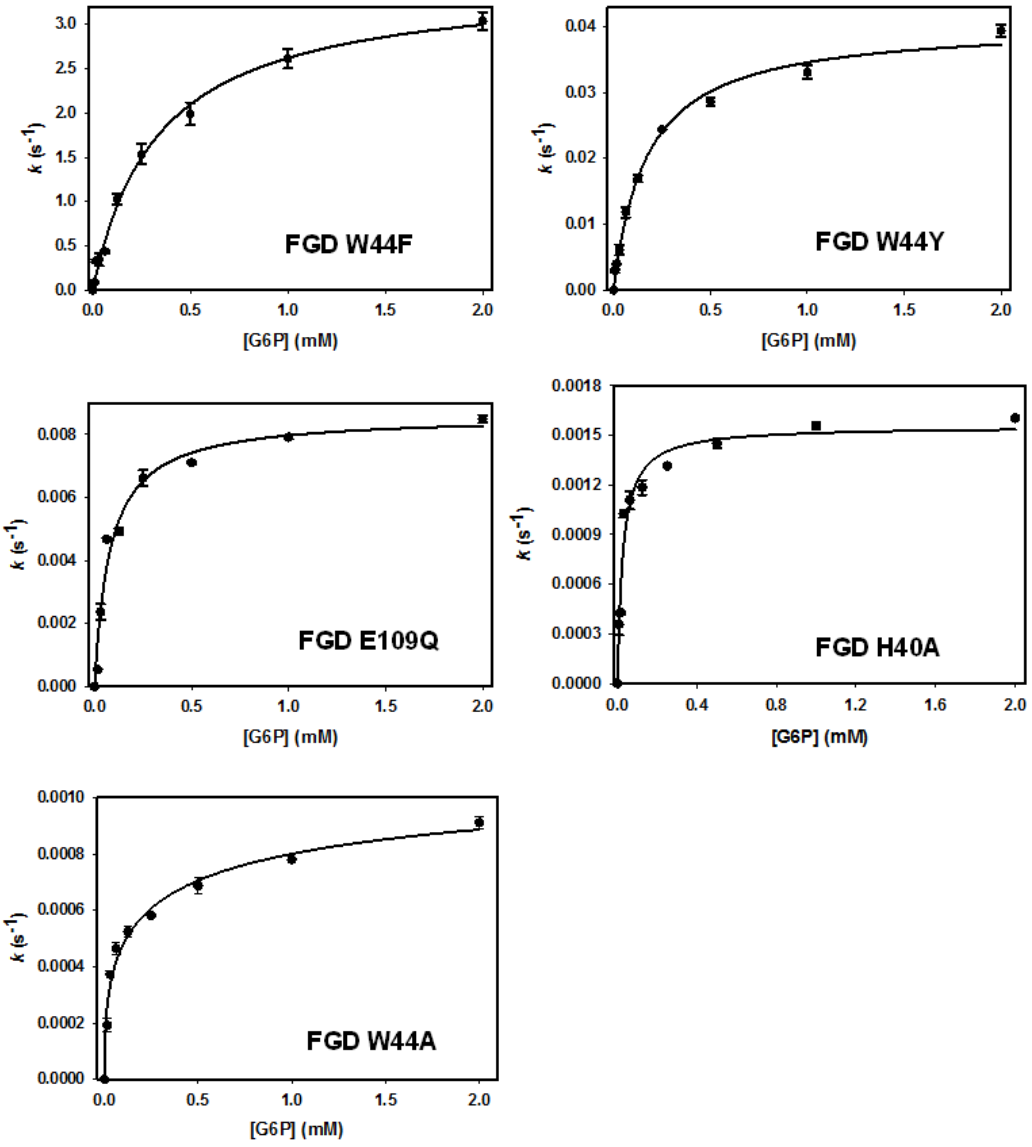

Figure B.1 Plots of rate constant *vs* G6P concentration for FGD variants. The FGD steady-state kinetics experiments were carried out in 50 mM Tris-HCl (pH 7.0) at 22 °C. The reactions were monitored by following the reduction of the F_{420} cofactor at 420 nm. The rate constants were obtained by dividing initial rates by enzyme concentration. The solid circles represent an average of two measurements of rate constants at various concentrations of G6P and the solid lines represent fit to Equation 2.3. The error bars in the plots represent standard deviations obtained from duplicate measurements of each G6P concentration.[72]

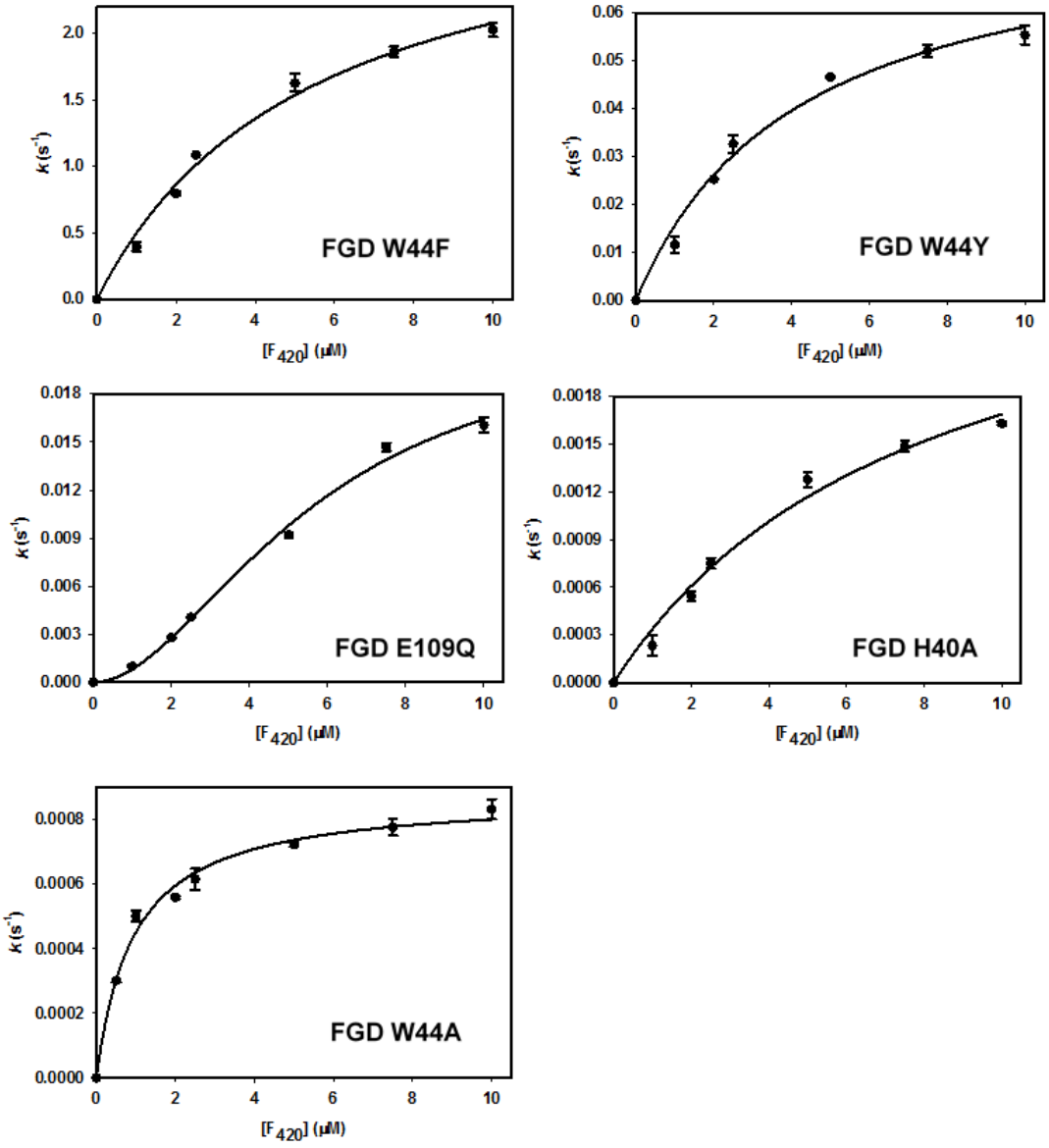

Figure B.2 Plots of rate constant *vs* F_{420} concentration for FGD variants. The FGD steady-state kinetics experiments were carried out in 50 mM Tris-HCl (pH 7.0) at 22 °C. The reactions were monitored by following the reduction of the F_{420} cofactor at 420 nm. The rate constants were obtained by dividing initial rates by enzyme concentration. The solid circles represent an average of two measurements of rate constants at various concentrations of F_{420} and the solid lines represent fit to Equation 2.3, except for the FGD E109Q that was fitted to Equation 2.8. The error bars in the plots represent standard deviations obtained from duplicate measurements of each F_{420} concentration.[72]

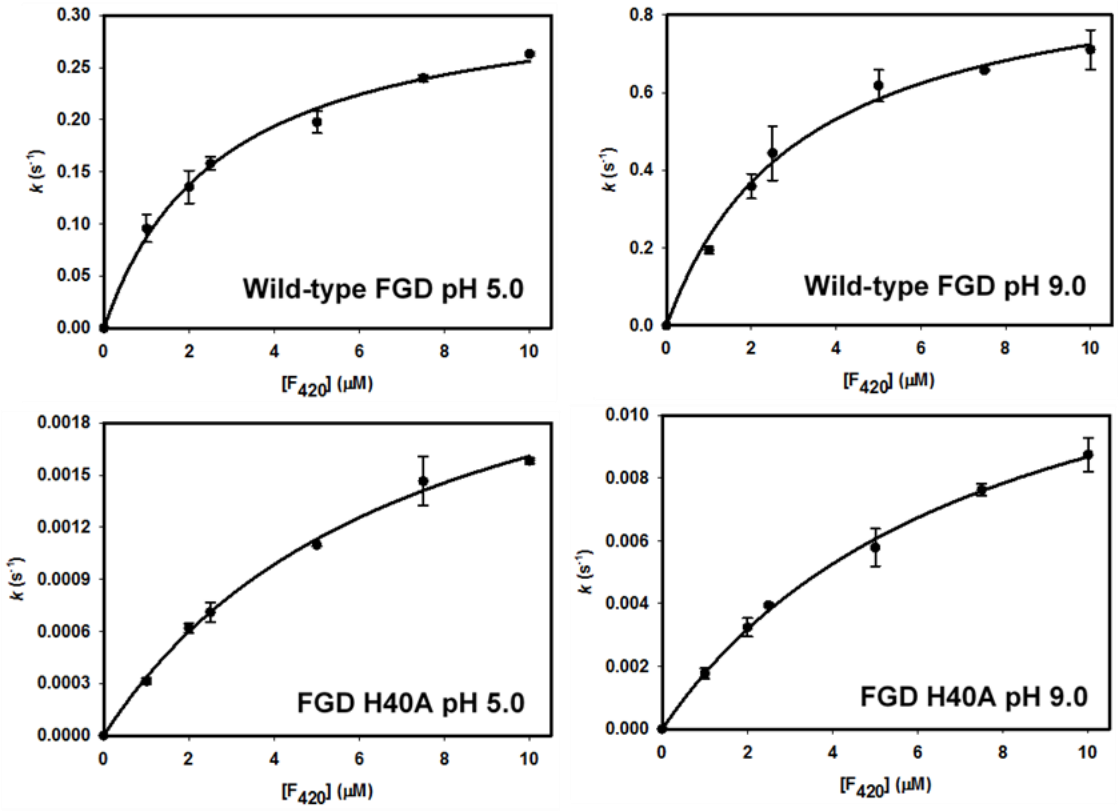

FGD	k_{cat} (s^{-1})		F_{420} K_m (μM)	
	pH 5.0	pH 9.0	pH 5.0	pH 9.0
Wild-type	0.33 ± 0.01	0.95 ± 0.05	2.7 ± 0.3	3.1 ± 0.5
H40A	0.003 ± 0.0002	0.02 ± 0.005	7.3 ± 0.8	7.6 ± 0.7

Figure B.3 Plots of rate constant *vs*. F_{420} concentration at pH extremes for wild-type FGD and FGD H40A. The experiments were carried out in appropriate buffers (pH 5.0 or 9.0) at 22 °C using a fixed G6P concentration and varying F_{420} concentrations. The reactions were monitored by following the reduction of the F_{420} cofactor at 400 nm (pH 5.0) or 420 nm (pH 9.0). Each data point represents an average of two measurements of rate constants at various concentrations of F_{420}. The kinetic parameters reported in the table were obtained by fitting the plots to Equation 2.3. The error bars in the plots represent standard deviations obtained from duplicate measurements of each F_{420} concentration. The uncertainties reported in the table were standard errors generated from the least squares fits to Equation 2.3.[72]

Appendix C

Multiple and single turnover pre-steady state kinetic curves for FGD H40A, E109Q, W44A, W44Y and W44F variants

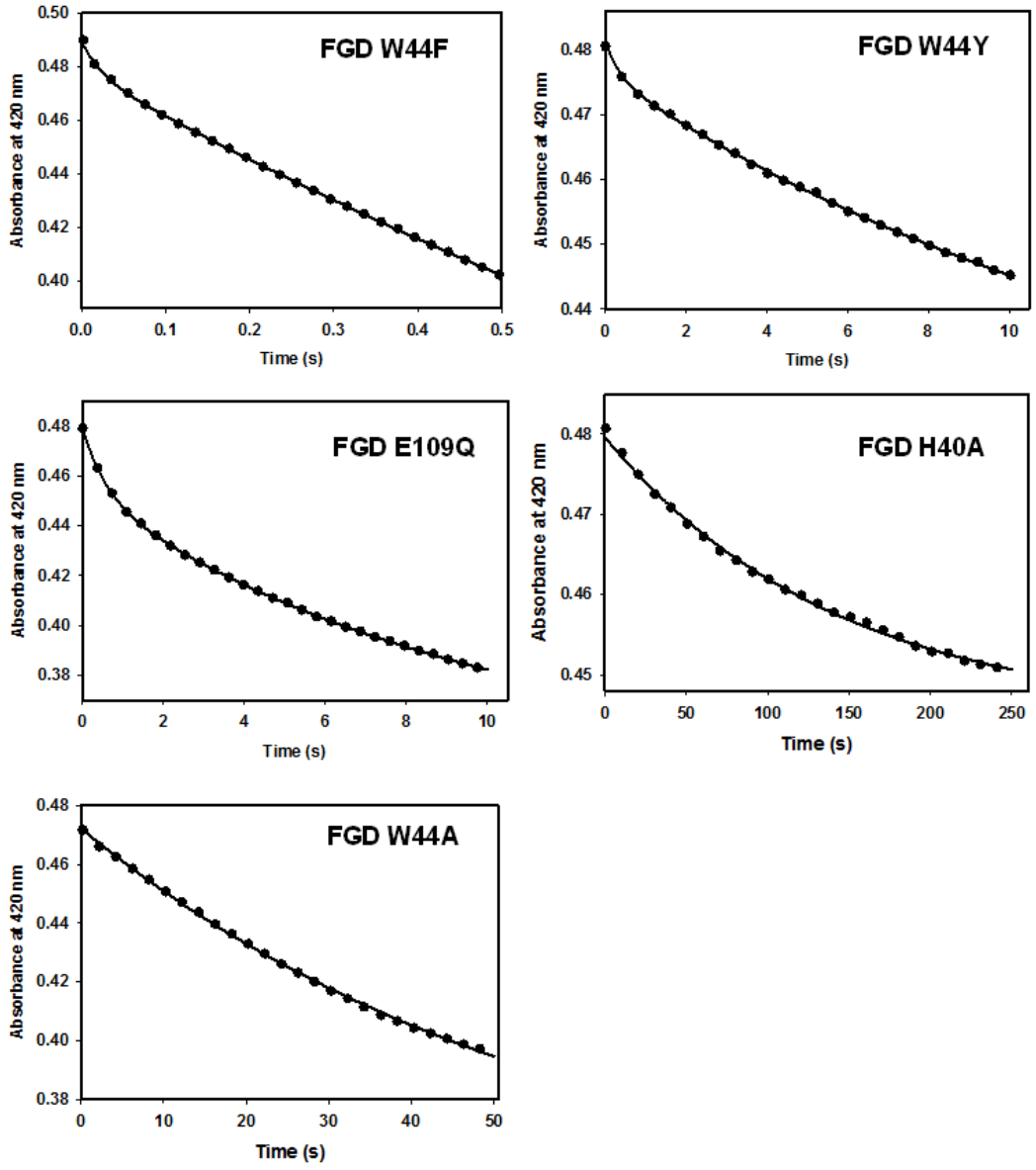

Figure C.1 Multiple turnover plots of absorbance at 420 nm *vs* time for FGD variants. The FGD pre-steady state kinetics experiments were carried out in diode array mode, using 50 mM Tris-HCl (pH 7.0) buffer at 22 °C. The multiple turnover experiments contained 6 µM FGD, 20 µM F_{420} and 1 mM G6P. The solid circles represent an average of two absorbance measurements at various times and the solid lines represent the fit to Equation 2.9 or 2.10. For clarity, only each 10th data point is shown on these plots.[72]

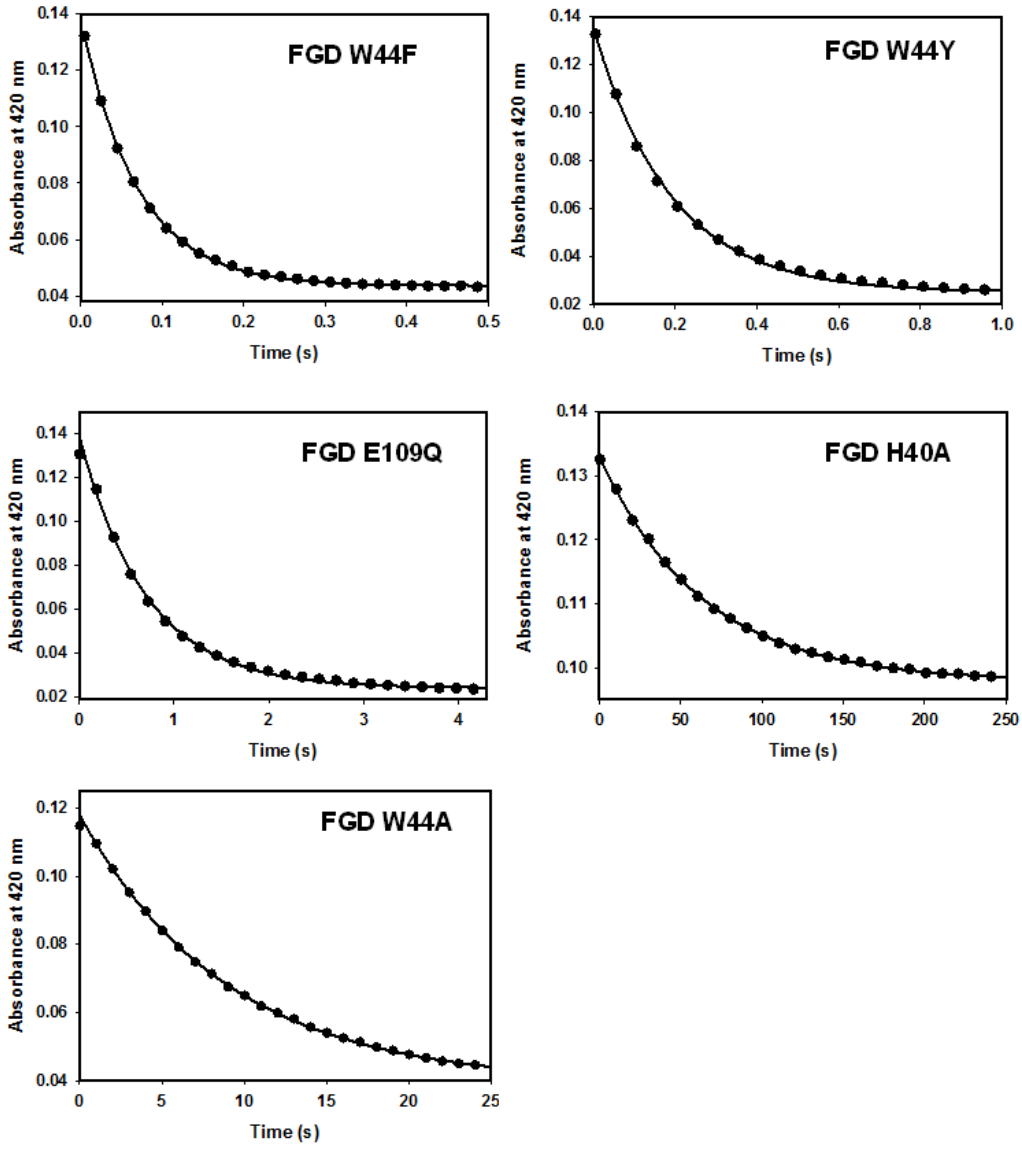

Figure C.2 Single turnover plots of absorbance at 420 nm *vs* time for FGD variants. The FGD pre-steady state kinetics experiments were carried out in diode array mode, using 50 mM Tris-HCl (pH 7.0) buffer at 22 °C. The single turnover experiments contained 50 µM FGD, 5 µM F_{420} and 500 µM G6P. The solid circles represent an average of two absorbance measurements at various times and the solid lines represent the fit to Equation 2.9.[72]

(1) Eirich, L. D.; Vogels, G. D.; Wolfe, R. S. Proposed Structure for Coenzyme F_{420} from *Methanobacterium*. *Biochem.* **1978**, *17*, 4583-4593.

(2) Joseph, E.; Le, C. Q.; Nguyen, T.; Oyugi, M.; Hossain, M. S.; Foss, F. W.; Johnson-Winters, K. Evidence of negative cooperativity and half-site reactivity within an F_{420}-dependent enzyme: Kinetic analysis of $F_{420}H_2$:$NADP^+$ oxidoreductase. *Biochem.* **2016**, *55*, 1082-1090.

(3) Yamazaki, S.; Tsai, L.; Stadtman, T. C.; Teshima, T.; Nakaji, A.; Shiba, T. Stereochemical studies of a selenium-containing hydrogenase from *Methanococcus vanniielii*: Determination of the absolute configuration of C-5 chirally labeled dihydro-8-hydroxy-5-deazaflavin cofactor. *PNAS* **1985**, *82*, 1364-1366.

(4) Yamazaki, S.; Tsai, L.; Stadtman, T. C.; Jacobson, F. S.; Walsh, C. Stereochemical studies of 8-hydroxy-5-deazaflavin-dependent $NADP^+$ reductase from *Methanococcus vannielii*. *J. Biol. Chem.* **1980**, *255*, 9025-9027.

(5) Eirich, L. D.; Vogels, G. D.; Wolfe, R. S. Distribution of coenzyme F_{420} and properties of its hydrolytic fragments. *J. Bacteriol.* **1979**, *140*, 20-27.

(6) Cheesman, P.; Toms-Wood, A.; Wolfe, R. S. Isolation and properties of a fluorescent compound, $Factor_{420}$, from *Methanobacterium* strain M.o.H. *J. Bacteriol.* **1972**, *112*, 527-531.

(7) Tzeng, S. F.; Wolfe, R. S.; Bryant, M. P. Factor 420-dependent pyridine nucleotide-linked hydrogenase system of *Methanobacterium ruminantium*. *J. Bacteriol.* **1975**, *121*, 154-191.

(8) Jacobson, F.; Walsh, C. Properties of 7,8-didemethyl-8-hydroxy-5-deazaflavins relevant to redox coenzyme function in methanogen metabolism. *Biochem.* **1984**, *23*, 979-988.

(9) Walsh, C. Naturally occurring 5-deazaflavin coenzymes:Biological redox roles. *Acc. Chem. Res.* **1986**, *19*, 216-221.

(10) DiMarco, A. A.; Bobik, T. A.; Wolfe, R. S. Unusual coenzymes of methanogenesis. *Annu. Rev. Biochem.* **1990**, *59*, 355-394.

(11) Purwantini, E. Coenzyme F_{420}: Factors affecting its purification from methanobacterium thermoautotrophicum and its conversion to F_{390} and effect of temperature on the spectral properties of coenzyme F_{420} and related compounds. University of Iowa, 1991.

(12) Graupner, M.; Xu, H.; White, R. H. Characterization of the 2-phospho-l-lactate transferase enzyme involved in coenzyme F_{420} biosynthesis in *Methanococcus jannaschii*. *Biochem* **2002**, *41*, 3754-3761.

(13) Graupner, M.; Xu, H.; White, R. H. The pyrimidine nucleotide reductase step in riboflavin and F_{420} biosynthesis in archaea proceeds by the eukaryotic route to riboflavin. *J. bacteriol.* **2002**, *184*, 1952-1957.

(14) Graham, D. E.; Xu, H.; White, R. H. Identification of the 7,8-didemethyl-8-hydroxy-5-deazariboflavin synthase required for coenzyme F_{420} biosynthesis. *Arch. Microbiol.* **2003**, *180*, 455-464.

(15) Bashiri, G.; Rehan, A. M.; Greenwood, D. R.; Dickson, J. M.; Baker, E. N. Metabolic engineering of cofactor F_{420} production in *Mycobacterium smegmatis*. *PLoS One* **2010**, *5*, e15803.

(16) Grochowski, L. L.; Xu, H.; White, R. H. Identification and characterization of the 2-phospho-l-lactate guanylyltransferase involved in coenzyme F_{420} biosynthesis. *Biochem.* **2008**, *47*, 3033-3037.

(17) Li, H.; Graupner, M.; Xu, H.; White, R. H. CofE catalyzes the addition of two glutamates to F_{420}-0 in F_{420} coenzyme biosynthesis in *Methanococcus jannaschii*. *Biochem.* **2003**, *42*, 9771-9778.

(18) Nocek, B.; Evdokimova, E.; Proudfoot, M.; Kudritska, M.; Grochowski, L. L.; White, R. H.; Savchenko, A.; Yakunin, A. F.; Edwards, A.; Joachimiak, A. Structure of an amide bond forming F_{420}:γ-glutamyl ligase from *Archaeoglobus fulgidus*-a member of a new family of non-ribosomal peptide synthases. *J. Mol. Biol.* **2007**, *372*.

(19) van Beelen, P.; Dijkstra, A. C.; Vogels, G. D. Quantitation of coenzyme F_{420} in methanogenic sludge by the use of reversed-phase high-performance liquid chromatography and a fluorescence detector. *Eur. J. Appl. Micorbiol. Biotechnol.* **1983**, *18*, 67-69.

(20) Dolfing, J.; Mulder, J. W. Comparison of methane production rate and coenzyme F_{420} content of methanogenic consortia in anaerobic granular sludge. *Appl. Environ. Microbiol.* **1985**, *49*, 1142-1145.

(21) Stetter, K. O.; Lauerer, G.; Thomm, M.; Neuner, A. Isolation of extremely thermophilic sulfate reducers: Evidence for a novel branch of archaebacteria. *Science* **1987**, *236*, 822-824.

(22) Vornolt, J.; Kunow, J.; Stetter, K. O.; Thauer, R. K. Enzymes and coenzymes of the carbon monoxide dehydrogenase pathway for autotrophic CO_2 fixation in *Archaeoglobus lithotrophicus* and the lack of carbon monoxide dehydrogenase in the heterotrophic *A. profundus*. *Arch. Microbiol.* **1995**, *163*, 112-118.

(23) Moller-Zinkhan, D.; Borner, G.; Thauer, R. K. Function of methanofuran, tetrahydromethanopterin, and coenzyme F_{420} in *Archaeoglobus fulgidus*. *Arch. Microbiol.* **1989**, *152*, 362-368.

(24) Gorris, L. G.; Voet, A. C.; van der Drift, C. Structural characteristics of methanogenic cofactors in the nonmethanogenic archaebacterium *Archaeoglobus fulgidus*. *Biofactors* **1991**, *3*, 29-35.

(25) Lin, X. L.; White, R. H. Occurrence of coenzyme F_{420} and its γ-monoglutamyl derivative in nonmethanogenic archaebacteria. *J. Bacteriol.* **1986**, *168*, 444-448.

(26) de Wit, L. E. A.; Eker, A. P. M. 8-Hydroxy-5-deazaflavin-dependent electron transfer in the extreme halophile *Halobacterium cutirubrum*. *FEMS Microbiol. Lett.* **1987**, *48*, 121-125.

(27) Daniels, L.; Bakhiet, N.; Harmon, K. Widespread distribution of a 5-deazaflavin cofactor in *Actinomyces* and related bacteria. *Syst. Appl. Microbiol.* **1985**, *6*, 12-17.

(28) Bair, T. B.; Isabelle, D. W.; Daniels, L. Structures of coenzyme F_{420} in *Mycobacterium* species. *Arch. Microbiol.* **2001**, *176*, 37-43.

(29) Purwantini, E.; Gillis, T. P.; Daniels, L. Presence of F_{420}-dependent glucose-6-phosphate dehydrogenase in *Mycobacterium* and *Nocardia* species, but absence from *Streptomyces* and *Corynebacterium* species and methanogenic Archaea. *FEMS Microb. Lett.* **1997**, *146*, 129-134.

(30) Wang, P.; Bashiri, G.; Gao, X.; Sawaya, M. R.; Tang, Y. Uncovering the enzymes that catalyze the final steps in oxytetracycline biosynthesis. *J. Am. Chem. Soc.* **2013**, *135*, 7138-7141.

(31) Kuo, M. S.; Yurek, D. A.; Coats, J. H.; Li, G. P. Isolation and identification of 7,8-didemethyl-8-hydroxy-5-deazariboflavin, an unusual cosynthetic factor in streptomycetes, from S*treptomyces lincolnensis*. *J. Antibiot.* **1989**, 475-478.

(32) Ebert, S.; Rieger, P. G.; Knackmuss, H. J. Function of coenzyme F_{420} in aerobic catabolism of 2,4,6-trinitrophenol and 2,4-dinitrophenol by *Nocardioides simplex* FJ2-1A. *J. Bacteriol.* **1999**, *181*, 2669-2674.

(33) Purwantini, E.; Mukhopadhyay, B. Conversion of NO_2 to NO by reduced coenzyme F_{420} protects mycobacteria from nitrosative damage. *Proc. Natl. Acad. Sci. U.S.A.* **2009**, *106*, 6333-6338.

(34) Jirapanjawat, T.; Ney, B.; Taylor, M. C.; Warden, A. C.; Afroze, S.; Russell, R. J.; Lee, B. M.; Jackson, C. J.; Oakeshott, J. G.; Pandey, G.; Greening, C. The redox cofactor F_{420} protects mycobacteria from diverse antimicrobial compounds and mediates a reductive detoxification system. *Appl. Environ. Microbiol.* **2016**, *82*, 6810-6818.

(35) Glas, A. F.; Maula, M. J.; Cryleb, M.; Barendsb, T. R. M.; Schneidera, S.; Kayaa, E.; Schlichtingb, I.; Carell, T. The archaeal cofactor FO is a light-harvesting antenna chromophore in eukaryotes. *Proc. Natl. Acad. Sci.* **2009**, *106*, 11540-11545.

(36) Eker, A. P.; Hessels, J. K. C.; Velde, J. V. D. Photoreactivating enzyme from the green alga *Scenedesmus acutus*. Evidence for the presence of two different flavin chromophores. *Biochem.* **1988**, *27*, 1758-1765.

(37) Seedorf, H.; Kahnt, J.; Pierik, A. J.; Thauer, R. K. *Si*-face stereospecificity at C5 of coenzyme F_{420} for $F_{420}H_2$ oxidase from methanogenic Archaea as determined by mass spectrometry. *FEBS J.* **2005**, *272*, 5337-5342.

(38) Warkentin, E.; Mamat, B.; Sordel-Klippert, M.; Wicke, M.; Thauer, R. K.; Iwata, M.; Iwata, S.; Ermler, U.; Shima, S. Structures of $F_{420}H_2$:$NADP^+$ oxidoreductase with and without its substrates bound. *EMBO J.* **2001**, *20*, 6561-6569.

(39) Deppenmeier, U.; Blaut, M.; Mahlmann, A.; Gottschalk, G. Reduced coenzyme F_{420}: heterodisulfide oxidoreductase, a proton-translocating redox system in methanogenic bacteria. *Proc. Antl. Acad. Sci.* **1990**, *87*.

(40) Kunow, J.; Linder, D.; Stetter, K. O.; Thauer, R. K. $F_{420}H_2$: quinone oxidoreductase from *Archaeoglobus fulgidus*. Characterization of a membrane bound multisubunit complex containing FAD and iron-sulfur clusters. *Eur. J. Biochem.* **1994**, *223*, 503-511.

(41) Hartzell, P. L.; Zvilius, G.; Escalante-Semerena, J. C.; Donnelly, M. I. Coenzyme F_{420} dependence of the methylenetetrahydromethanopterin dehydrogenase of *Methanobacterium thermoautotrophicum*. *Biochem. Biophys. Res. Commun.* **1985**, *133*, 884-890.

(42) Ma, K.; Thauer, R. K. Purification and properties of N5, N10-methylenetetrahydromethanopterin reductase from *Methanobacterium thermoautotrophicum* (strain Marburg). *Eur. J. Biochem.* **1990**, *191*, 187-193.

(43) Aufhammer, S. W.; Warkentin, E.; Berk, H.; Shima, S.; Thauer, R. K.; Ermler, U. Coenzyme binding in F_{420}-dependent secondary alcohol dehydrogenase, a member of the bacterial luciferase family. *Struct.* **2004**, *12*, 361-370.

(44) Johnson, E. F.; Mukhopadhyay, B. A new type of sulfite reductase, a novel coenzyme F_{420}-dependent enzyme, from the methanarchaeon *Methanocaldococcus jannaschii*. *J. Biol. Chem.* **2005**, *280*, 38776-38786.

(45) Purwantini, E.; Daniels, L. Purification of a novel coenzyme F_{420}-dependent glucose-6-phosphate dehydrogenase from *Mycobacterium smegmatis*. *J. Bacteriol.* **1996**, *178*, 2861-2866.

(46) Cellitti, S. E.; Shaffer, J.; Jones, D. H.; Mukherjee, T.; Gurumurthy, M.; Bursulaya, B.; Boshoff, H. I.; Choi, I.; Nayyar, A.; Lee, Y. S.; Cherian, J.; Niyomrattanakit,

P.; Dick, T.; Manjunatha, U. H.; Clifton E. Barry, I.; Spraggon, G.; Geierstanger, B. H. Structure of Ddn, the deazaflavin-dependent nitroreductase from *Mycobacterium tuberculosis* involved in bioreductive activation of PA-824 *Struct.* **2012**, *20*, 101-112.

(47) Purwantini, E.; Mukhopadhyay, B. Rv0132c of *Mycobacterium tuberculosis* encodes a coenzyme F_{420}-dependent hydroxymycolic acid dehydrogenase. *PLoS One* **2013**, *8*, e81985.

(48) Taylor, M. C.; Jackson, C. J.; Tattersall, D. B.; French, N.; Peat, T. S.; Newman, J.; Briggs, L. J.; Lapalikar, G. V.; Campbel, P. M.; Scott, C.; Russell, R. J.; Oakeshott, J. G. Identification and characterization of two families of $F_{420}H_2$-dependent reductases from mycobacteria that catalyze aflatoxin degradation. *Mol. Microbiol.* **2010**, *78*, 561-575.

(49) Manjunatha, U. H.; Boshoff, H.; Dowd, C. S.; Zhang, L.; Albert, T. J.; Norton, J. E.; Daniels, L.; Dick, T.; Pang, S. S.; Barry, C. E. Identification of a nitroimidazo-oxazine-specific protein involved in PA-824 resistance in *Mycobacterium tuberculosis*. *Proc. Natl. Acad. Sci. U.S.A.* **2006**, *103*, 431-436.

(50) Bashiri, G.; Squire, C. J.; Moreland, N. J.; Baker, E. N. Crystal structures of F_{420}-dependent glucose-6-phosphate dehydrogenase FGD1 involved in the activation of the anti-tuberculosis drug candidate PA-824 reveal the basis of coenzyme and substrate binding. *J. Biol. Chem.* **2008**, *283*, 17531-17541.

(51) WHO. Global Tuberculosis Report 2015. *WHO Press* **2015**, *20*, 1-204.

(52) Villemagne, B.; Crauste, C.; Flipo, M.; Baulard, A. R.; Deprez, B.; Willand, N. Tuberculosis: the drug development pipeline at a glance. *Eur. J. Med. Chem.* **2012**, *51*, 1-16.

(53) Stover, C. K.; Warrener, P.; VanDevanter, D. R.; Sherman, D. R.; Arain, T. M.; Langhorne, M. H.; Anderson, S. W.; Towell, J. A.; Yuan, Y.; McMurray, D. N.; Kreiswirth, B. N.; Barry, C. E.; Baker, W. R. A small-molecule nitroimidazopyran drug candidate for the treatment of tuberculosis. *Nature* **2000**, *405*, 962-966.

(54) Lenaerts, A. J.; Gruppo, V.; Marietta, K. S.; Johnson, C. M.; Driscoll, D. K.; Tompkins, N. M.; Rose, J. D.; Reynolds, R. C.; Orme, I. M. Preclinical testing of the nitroimidazopyran PA-824 for activity against *Mycobacterium tuberculosis* in a series of in vitro and in vivo models. *Antimicrob. Agents Chemother.* **2005**, *49*, 2294-2301.

(55) Manjunatha, U.; Boshoff, H.; Barry, C. E. I. The mechanism of action of PA-824. *Comm. Integ. Biol.* **2009**, *2*, 215-218.

(56) Singh, R.; Manjunatha, U.; Boshoff, H. I. M.; Ha, Y. H.; Niyomrattanakit, P.; Ledwidge, R.; Dowd, C. S.; Lee, Y.; Kim, P.; Zhang, L.; Kang, S.; Keller, T. H.; Jiricek, J.; Barry, C. E. $^{r.}$ PA-824 kills nonreplicating *Mycobacterium tuberculosis* by intracellular NO release. *Science* **2008**, *322*, 1392-1395.

(57) Matsumoto, M.; Hashizume, H.; Tomishige, T.; Kawasaki, M.; Tsubouchi, H.; Sasaki, H.; Shimokawa, Y.; Komatsu, M. OPC-67683, a nitro-dihydroimidazooxazole derivative with promising action against tuberculosis in vitro and in mice. *PLoS Med.* **2006**, *3*, 2131-2144.

(58) Bashiri, G.; Perkowski, E. F.; Turner, A. P.; Feltcher, M. E.; Braunstein, M.; Baker, E. N. Tat-dependent translocation of an F_{420}-binding protein of *Mycobacterium tuberculosis*. *PLoS One* **2012**, *7*, e45003.

(59) Selengut, J. D.; Haft, D. H. Unexpected abundance of coenzyme F_{420}-dependent enzymes in *Mycobacterium tuberculosis* and other actinobacteria. *J. Bacteriol.* **2010**, *192*, 5788-5798.

(60) Darwin, K. H.; Ehrt, S.; Gutierrez-Ramos, J.-C.; Weich, N.; Nathan, C. F. The Proteasome of *Mycobacterium tuberculosis* Is Required for Resistance to Nitric Oxide. *Science* **2003**, *302*, 1963-1966.

(61) Gurumurthy, M.; Rao, M.; Mukherjee, T.; Rao, S. P.; Boshoff, H. I.; Dick, T.; Barry, C. E., 3rd; Manjunatha, U. H. A novel F_{420}-dependent anti-oxidant mechanism protects *Mycobacterium tuberculosis* against oxidative stress and bactericidal agents. *Mol. Microbiol.* **2013**, *87*, 744-755.

(62) Au, S. W. N.; Gover, S.; Lam, V. M. S.; Adams, M. J. Human glucose-6-phosphate dehydrogenase: the crystal structure reveals a structural $NADP^+$ molecule and provides insights into enzyme deficiency. *Struct.* **2000**, *8*, 293-303.

(63) Cosgrove, M. S.; Naylor, C.; Paludan, S.; Adams, M. J.; Levy, H. R. On the mechanism of the reaction catalyzed by glucose 6-phosphate dehydrogenase. *Biochem.* **1998**, *37*, 2759-2767.

(64) Kim, Y. S.; Kim, Y. I.; Byun, H. S. Inactivation of *Saccharomyces cerevisiae* glucose-6-phosphate dehydrogenase by diethylpyrocarbonate. *Biochem. Int.* **1988**, *17*, 1099-1106.

(65) Domschke, W.; Engel, H. J.; Domagk, G. F. Protein structure and enzyme activity. IV. Demonstration of essential histidine residues in the glucose-6-phosphate dehydrogenase from *Candida utilis*. *Hoppe-Seyler's Z. Physiol. Chem.* **1969**, *350*, 1117-1120.

(66) Kotaka, M.; Gover, S.; Vandeputte-Rutten, L.; Au, S. W. N.; Lams, V. M. S.; Admas, M. J. Structural studies of glucose-6-phosphate and $NADP^+$ binding to human glucose-6-phosphate dehydrogenase. *Acta Crystallogr., Sect D: Biol. Crystallogr.* **2005**, *61*, 495-504.

(67) Kunow, J.; Schworer, B.; Setzke, E.; Thauer, R. K. *Si*-face stereospecificity at C5 of coenzyme F_{420} for F_{420} -dependent N^5,N^{10}-methylenetetrahydromethanopterin dehydrogenase, F_{420} -dependent N^5,N^{10}-methylenetetrahydromethanopterine reductase and $F_{420}H_2$:dimethylnaphthoquinone oxidoreductase. *Eur. J. Biochem.* **1993**, *214*, 641-646.

(68) Klein, A. R.; Berk, H.; Purwantini, E.; Daniels, L.; Thauer, R. K. *Si*-face stereospecificity at C5 of coenzyme F_{420} for F_{420}-dependent glucose-6-phosphate dehydrogenase from *Mycobacterium smegmatis* and F_{420}-dependent alcohol dehydrogenase from *Methanoculleus thermophilicus*. *Eur. J. Biochem.* **1996**, *239*, 93-97.

(69) Bashiri, G.; Squire, C. J.; Baker, E. N.; Moreland, N. J. Expression, purification and crystallization of native and selenomethionine labeled *Mycobacterium tuberculosis* FGD1 (Rv0407) using a *Mycobacterium smegmatis* expression system. *Prot. Expr. Purif.* **2007**, *54*, 38-44.

(70) Moiller, M.; Denicola, A. Study of protein-ligand binding by fluorescence. *Biochem. Mol. Biol. Ed.* **2002**, *30*, 309-312.

(71) Koshland, D. E.; Nemethy, G.; Filmer, D. Comparison of experimental binding data and theoretical models in 613 proteins containing subunits. *Biochem.* **1966**, *5*, 365−385.

(72) Oyugi, M. A.; Bashiri, G.; Baker, E. N.; Johnson-Winters, K. Investigating the reaction mechanism of F_{420}-dependent glucose-6-phosphate dehydrogenase from *Mycobacterium tuberculosis*: Kinetic analysis of the wild-type and mutant enzymes. *Biochem.* **2016**, *55*, 5566–5577.

(73) Aufhammer, S. W.; Warkentin, E.; Ermler, U.; Hagemeier, C. H.; Thauer, R. K.; Shima, S. Crystal structure of methylenetetrahydromethanopterin reductase (Mer) in complex with coenzyme F_{420}: Architecture of the F_{420}/FMN binding site of enzymes

within the nonprolyl *cis*-peptide containing bacterial luciferase family. *Prot. Sci.* **2005**, *14*, 1840-1849.

(74) Cosgrove, M. S.; Gover, S.; Naylor, C. E.; Vandeputte-Rutten, L.; Adams, M. J.; Levy, H. R. An examination of the role of Asp-177 in the His-Asp catalytic dyad of *Leuconostoc mesenteroides* glucose-6-phosphate dehydrogenase: X-ray structure and pH dependence of kinetic parameters of the D177N mutant enzyme. *Biochem.* **2000**, *39*, 15002-15011.

(75) Viola, R. E. Kinetic studies of the reactions catalyzed by glucose-6-phosphate dehydrogenase from *Leuconostoc mesenteroides*: pH variation of kinetic parameters. *Arch. Biochem. & Biophys.* **1984**, *228*, 415-424.

(76) Bhattacharyya, L.; Rohrer, J. S.: *Applications of ion chromatography for pharmaceutical and biological products*; John Wiley & Sons, Inc., 2012; Vol. 1.

(77) Neet, K. E. Cooperativity in enzyme function: Equilibrium and kinetic aspects. *Meth. Enzymol.* **1995**, *249*, 519–567.

(78) Ricard, J.; Cornish-Bowden, A. Co-operative and allosteric enzymes: 20 years on. *Eur. J. Biochem.* **1987**, *166*, 255-272.

(79) Hammes, G. G.; Wu, C. W. Kinetics of allosteric enzymes. *Annu. Rev. Biophys. Bioeng.* **1974**, *3*, 1–33.

(80) Ferdinand, W. The interpretation of non-hyperbolic rate curves for two-substrate enzymes. A possible mechanism for phosphofructokinase. *Biochem. J.* **1966**, *98*, 278-283.

(81) Frieden, C. Kinetic aspects of regulation of metabolic processes. The hysteretic enzyme concept. *J. Biol. Chem.* **1970**, *245*, 5788–5799.

(82) Kadirvelraj, R.; Sennett, N. C.; Custer, G. S.; Phillips, R. S.; Wood, Z. A. Hysteresis and negative cooperativity in human UDP-glucose dehydrogenase. *Biochem. Int.* **2013**, *52*, 1456-1465.

(83) Jensen, R. A.; Trentini, W. C. Alternative allosteric effects exerted by end products upon a two substrate enzyme in *Rhodomicrobium vannielii*. *J. Biol. Chem.* **1970**, *245*, 2018–2022.

(84) Kurganov, B. I.; Dorozhko, A. I.; Kagan, Z. S.; Yakovlev, V. A. The theoretical analysis of kinetic behaviour of "hysteretic" allosteric enzymes. II. The dissociating and associating enzymic systems in which the rate of installation of equilibrium between the oligomeric forms is small in comparison with that of enzymatic reaction. *J. Theor. Biol.* **1976**, *60*, 271-286.

(85) Cleland, W. W. The use of isotope effects to determine enzyme mechanisms. *J. Biol. Chem.* **2003**, *278*, 51975-51984.

(86) O'Leary, M. H. Multiple isotope effects on enzyme-catalyzed reactions. *Ann. Rev. Biochem. Biophys. Acta.* **1989**, *58*, 377-401.

(87) Hermes, J. D.; Roeske, C. A.; O'Leary, M. H.; Cleland, W. W. Use of multiple isotope effects to determine enzyme mechanisms and intrinsic isotope effects. Malic enzyme and glucose 6-phosphate dehydrogenase. *Biochem.* **1982**, *21*, 5106–5114.

(88) Mikkelsen, K.; Nielsen, S. O. Acidity measurement with the glass electrode in H_2O and D_2O mixtures. *J. Phys. Chem.* **1960**, *64*, 632-637.

(89) Glasoe, P. K.; Long, F. A. Use of glass electrodes to measure acidities in deuterium oxide. *J. Phys. Chem.* **1960**, *64*, 188-191.

(90) Karpefors, M.; Ädelroth, P.; Brzezinski, P. The onset of the deuterium isotope effect in cytochrome c oxidase. *Biochem.* **2000**, *39*, 5045–5050.

(91) Kresge, A. J. Solvent isotope effect in H_2O-D_2O mixtures. *Pure Appl. Chem.* **1964**, *8*, 243–258.

(92) Schowen, K. B.; Schowen, R. L. Solvent isotope effects of enzyme systems. *Meth. Enzymol.* **1982**, *87*, 551-606.

(93) Harris, T. K.; Mildvan, A. S. High-precision measurement of hydrogen bond lengths in proteins by nuclear magnetic resonance methods. *Prot. Struct. Fun. Gen* **1999**, *35*, 275-282.

(94) Harris, T. K.; Zhao, Q.; Mildvan, A. S. NMR studies of strong hydrogen bonds in enzymes and in a model compound. *J. Mol. Struct.* **2000**, *552*, 97-109.

(95) Mildvan, A. S.; Massiah, M. A.; Harris, T. K.; Marks, G. T.; Harrison, D. H. T.; Viragh, C.; Reddy, P. M.; Kovach, I. M. Short, strong hydrogen bonds on enzymes: NMR and mechanistic studies. *J. Mol. Struct.* **2002**, *615*, 163-175.

(96) Wei, Y.; McDermott, A. E.: *Modeling NMR chemical shifts: gaining insights into structure and environment*; Oxford University Press: Cary, NC, 1999.

(97) Oyugi, M. A.; Bashiri, G.; Baker, E. N.; Johnson-Winters, K. Mechanistic insights into F_{420}-dependent glucose-6-phosphate dehydrogenase using isotope effects and substrate inhibition studies. *Biochim. Biophys. Acta.* **2017**, *(Manuscript in Revision)*.

(98) Cleland, W. W. The kinetics of enzyme-catalyzed reactions with two or more substrates or products: II. Inhibition: Nomenclature and theory. *Biochim. Biophys. Acta.* **1963**, *67*, 173-187.

(99) Fromm, H. J. The use of alternative substrates in studying enzymic mechanisms involving two substrate. *Biochim. Biophys. Acta.* **1964**, *81*, 413-417.

(100) Bessell, M.; Thomas, T. The effect of substitution at C-2 of D-glucose 6-phosphate on the rate of dehydrogenation by glucose 6-phosphate dehydrogenase (from yeast and from rat liver). *Biochem. J.* **1973**, *131*, 83-89.

(101) Kanji, M. I.; Toews, M. L.; Carper, W. R. A kinetic study of glucose-6-phosphate dehydrogenase *J. Biol. Chem.* **1976**, *251*, 2258-2262.

(102) Shreve, D. S.; Levy, H. R. Kinetic mechanism of glucose-6-phosphate dehydrogenase from the lactating rat mammary gland: Implications for regulation. *J. Biol. Chem.* **1980**, *255*, 2670-2677.

(103) Wang, X. T.; Shannon, W. N.; Veronica, M. S.; Engel, P. C. Recombinant human glucose-6-phosphate dehydrogenase: Evidence for a rapid-equilibrium random-order mechanism. *Eur. J. Biochem.* **2002**, *269*, 3417-3424.

(104) Cleland, W. W.: *Steady state kinetics in the enzymes*; 3rd ed.; Academic Press: New York, 1970; Vol. II. pp. 1-65.

(105) Ulusu, N. U.; Tandogan, B. Purification and kinetics of sheep kidney cortex glucose-6-phosphate dehydrogenase. *Comp. Biochem. Physiol.* **2006**, *143*, 249-255.

(106) Ulusu, N. U.; Tandogan, B.; Tezcan, F. E. Kinetic properties of glucose-6-phosphate dehydrogenase from lamb kidney cortex. *Biochimie* **2005**, *87*, 187-190.

(107) Horecker, B. L.; Smyrniotis, P. Z. Reversibility of glucose-6-phosphate oxidation. *Biochim. Biophys. Acta.* **1953**, *12*, 98-102.

(108) Schowen, K. B.; Limbach, H.-H.; Denisov, G. S.; Schowen, R. L. Hydrogen bonds and proton transfer in general-catalytic transition-state stabilization in enzyme catalysis. *Biochim. Biophys. Acta.* **1999**, *1458*, 43-62.

(109) Quinn, D. M.; Sutton, L. D.: *Theoretical basis and mechanistic utility of solvent isotope effects*; CRC Press: Boca Raton, 1991. pp. 73-126.

(110) Quinn, D. M.: *Theory and practice of solvent isotope effects*; CRC Press: Boca Raton, 2005. pp. 995-1018.

(111) Kreevoy, M. M.; Liang, T. M. Structures and isotopic fractionation factors of complexes. *J. Am. Chem. Soc.* **1980**, *102*, 3315-3322.

(112) Cleland, W. W. Low-barrier hydrogen bonds and enzymatic catalysis. *Arch. Biochem. & Biophys.* **2000**, *382*, 1-5.

(113) Cleland, W. W. The low-barrier hydrogen bond in enzymic catalysis. *Adv. Phys. Org. Chem.* **2010**, *44*, 1-17.

(114) Northrop, D. B. The expression of isotope effects on enzyme-catalyzed reactions. *Ann. Rev. Biochem.* **1981**, *50*, 103-131.

(115) Cook, P. F.; Cleland, W. W. Mechanistic deductions from isotope effects in multireactant enzyme mechanisms. *Biochem.* **1981**, *20*, 1790-1796.

(116) Hermes, J. D.; Cleland, W. W. Evidence from multiple isotope effect determinations for coupled hydrogen motion and tunneling in the reaction catalyzed by glucose-6-phosphate dehydrogenase. *J. Am. Chem. Soc.* **1984**, *106*, 7263-7264.

(117) Otwinowski, Z.; Minor, W. Processing of X-ray diffraction data collected in oscillation mode. *Meth. Enzymol.* **1997**, *276*, 307-326.

(118) Emsley, P.; Cowtan, K. Coot: model-building tools for molecular graphics. *Acta Crystallogr. D. Biol. Crystallogr.* **2004**, *60*, 2126-2132.

(119) Adams, P. D.; Afonine, P. V.; Bunkoczi, G.; Chen, V. B.; Davis, I. W.; Echols, N.; Headd, J. J.; Hung, L. W.; Kapral, G. J.; Grosse-Kunstleve, R. W.; McCoy, A. J.; Moriarty, N. W.; Oeffner, R.; Read, R. J.; Richardson, D. C.; Richardson, J. S.; Terwilliger, T. C.; Zwart, P. H. PHENIX: a comprehensive Python-based system for macromolecular structure solution. *Acta Crystallogr D Biol Crystallogr* **2010**, *66*, 213-221.

(120) Chen, V. B.; Arendall, W. B., 3rd; Headd, J. J.; Keedy, D. A.; Immormino, R. M.; Kapral, G. J.; Murray, L. W.; Richardson, J. S.; Richardson, D. C. MolProbity: all-

atom structure validation for macromolecular crystallography. *Acta Crystallogr. D. Biol. Crystallogr.* **2010**, *66*, 12-21.

Biographical Information

Mercy Amondi Oyugi earned her Bachelor of Science degree in Biochemistry with a Mathematics minor from Western Michigan University in the Fall of 2011. In 2012, she joined The University of Texas at Arlington as a BS-PhD track graduate student with a major in Biochemistry. For her dissertation project, Mercy worked under the supervision of Dr. Kayunta Johnson-Winters, where her research focused on the characterization of F_{420}-dependent enzymes, particularly FGD and Fno. While pursuing her doctoral degree and focusing on her research, Mercy also worked as a Graduate Teaching Assistant for several General Chemistry lab courses at UTA's Department of Chemistry and Biochemistry.

Mercy has also received noteworthy awards during her career as a graduate student including the NOBCChE E.I. Dupont Graduate Fellowship, UTA's Dr. Charles K. Baker Character Fellowship, ASBMB graduate travel award, NOBCChE graduate travel award and the ACS DFW 1st place graduate oral presentation. Mercy has presented her work at various local and national scientific meetings and she has also published her research in peer-reviewed journals. From September 2016 to June 2017, Mercy completed a co-op at GlaxoSmithKline, working with the Biopharmaceutical R&D Advanced Manufacturing Technologies group.

Mercy Amondi Oyugi graduated from The University of Texas at Arlington in August 2017, with a PhD in Biochemistry.